Finite Amplitude Waves in Plane Poiseuille Flow

Thesis by
Jeffrey D. Pugh

In Partial Fulfillment of the Requirements
for the Degree of
Doctor of Philosophy

California Institute of Technology
Pasadena, California

June, 1988

(Submitted August 7th, 1987)

Acknowledgments

A number of people have helped me, directly and indirectly, with this thesis. On the academic side, Professor Saffman suggested this project in the first place, and offered me advice and criticism at those times when nothing would work. I had a number of helpful discussions with Steve Wiggins and Michael Landman, particularly regarding the material in Chapter 3. I also want to thank Juan Zufiria and Jim Kamm for answering the phone hundreds of times for me when I wasn't in the office. Jeff Aguilera's THEME package made the preparation of this dissertation almost a pleasure. Needless to say, most of the good ideas in it are my own, and any errors or omissions can be blamed on the computer.

Most of all it has been my friends who have made my stay at Caltech enjoyable, particularly Joe J. Rushanan and Warren Kibbe, and my fellow bridge players, Jeff Goldsmith, Walter Hamilton and Jim Bys.

My parents and brother have been more supportive than I would have thought possible, given the distance separating us, and their visits provided a welcome excuse to see more of the USA.

In addition to thanking Caltech for financial support, I acknowledge the support of the Office of Naval Research (Grant N00014-85-K-0205) and the Department of Energy, Office of Energy Sciences (DE-AS03-76ER-72012), Applied Mathematical Sciences (KC-07-01-01).

Finally, I want to thank my wife, Jennifer Stern, for her unceasing willingness to discuss problems and listen to my complaints, and for her love and encouragement, without which I would not have finished.

Abstract

Nonlinear behavior in plane Poiseuille flow has attracted theoretical interest over the last decade, both because of its tractability and because it is believed that some of the results may be applicable to phenomena occurring in the boundary layer. We have investigated the existence of three-dimensional finite amplitude waves in plane Poiseuille flow, in the hope of finding candidates for a class of simple flows which might provide insight into the nature of turbulence. These so-called *vortical states* would exist as attractors for the turbulent flow and mimic many of its properties.

One of the requisite properties of these simple flows is existence at the low Reynolds numbers observed in experimental studies of transition to turbulence in plane Poiseuille flow. Although no such three-dimensional solutions were found in our study, a number of new insights have been made into the structure and stability of two- and three-dimensional steady wave solutions in plane Poiseuille flow. These in turn suggest new areas of investigation for finding vortical states.

Table of Contents

List of Figures

List of Tables

CHAPTER 1

INTRODUCTION

1.1 Background

A major thrust of research in fluid mechanics is the attempt to understand turbulence in fluid flow and the nature of the transition process by which the motion of a viscous fluid changes from laminar to turbulent flow. In recent years attention has turned to theoretical attempts to solve the fully nonlinear Navier-Stokes equations in various simple flow geometries. In particular, plane Poiseuille flow (PPF) has emerged as a tractable problem to consider. This is the viscous, incompressible flow between two infinite parallel surfaces, driven by a constant streamwise pressure gradient. The fully-developed laminar flow has a parabolic velocity profile between the two surfaces.

Originally considered as a simple prototype for more complicated shear flows (such as boundary layer flow over a flat plate), PPF is now of interest in its own right. In part this is because it has become possible to construct experiments which produce the high aspect ratios and low turbulence levels necessary for accurate comparison with the theoretical models of infinite parallel surfaces. It is ironic that while PPF seems difficult to produce experimentally, its theoretical analysis is straightforward, while for boundary layer flow the converse is true.

1.2 Review of experiments

For many years experimenters were unable to observe the theoretically predicted periodic disturbances in PPF because of the difficulty in producing laminar flow close to the critical Reynolds number. In a physical experiment one has to have a large aspect ratio (width to height) and a long enough channel for fully-developed laminar flow to form, and yet avoid contamination from the side walls. Some of these requirements are contradictory; for instance with the requisite narrow channel height, the effect of wall imperfections is enhanced. Despite these obstacles, some carefully controlled experiments meeting the requirements have been performed in recent years. We summarize below Herbert's (1983a) review of these, and those experiments which have been done since then.

Karnitz, Potter and Smith (1974) kept the flow laminar to **Re** = 5000 and observed that natural sinusoidal velocity fluctuations preceded turbulent bursts.

Nishioka, Iida and Ichikawa (1975) achieved an effective turbulence level as low as 0.01%. Fully-developed laminar PPF was maintained up to **Re** = 8000-9000. They maintained fully 2D flow up to **Re** = 3500 and mildly 3D above that, attributed to warping of the upper wall. Amplitude distributions, phase velocities and amplification rates of controlled small disturbances agreed well with theory. There was reasonable agreement with predictions of Herbert (1976,1977) for steady waves.

Nishioka, Iida and Kanbayashi (1978) concentrated on the condition for first occurrence of 3D effects. They observed the instability of 2D disturbances to 3D effects and 3D "peak-valley splitting" when spanwise dependence of the disturbance appears, indicating formation of a spanwise, periodic longitudinal vortex system. Onset of three-dimensionality depended on the threshold amplitude of the perturbation, implying a secondary instability of the 2D perturbed flow. They observed formation of a high-shear layer and appearance of high frequency "spikes" in the velocity perturbation.

Nishioka, Asai and Iida (1981) detailed the appearance of the high-shear layer and the formation of spikes in the flow, indicating formation of a viscous sublayer and horse-shoe vortices.

Kozlov and Ramazanov (1980) achieved a turbulence level of 0.1%, maintaining laminar flow up to $\mathbf{Re} = 7000$. They possibly did not achieve fully-developed flow for $\mathbf{Re} > 4000$.

Kozlov and Ramazanov (1983) investigated 3D development of controlled 2D disturbances, finding Λ-vortices similar to those observed in flat-plate boundary layer experiments. The spanwise spacing appeared to be independent of Reynolds number or disturbance frequency.

Carlson, Widnall and Peeters (1982) conducted a flow visualization of artificially triggered transition using mica particles in a water channel. Natural and artificial transition occurred at $\mathbf{Re}$=1000, initiated by the formation of turbulent spots.

Nishioka and Asai (1985) introduced three different types of disturbances into fully-developed PPF and concluded transition occurred above $\mathbf{Re} = 1000$, with a threshold amplitude the same as the amplitude of disturbances in full turbulent flow.

Alavyoon, Henningson and Alfresson (1986) studied the formation and evolution of turbulent spots for $1100 < \mathbf{Re} < 2200$, finding laminar flow was always maintained for $\mathbf{Re} < 1100$.

These last three experiments confirm the relatively crude experiments of Davies and White (1928) and Patel and Head (1969), who disturbed the flow using right-angled corners and found a transition Reynolds number of about $\mathbf{Re} = 1000$.

1.3 Time-dependent numerical simulations

The uniform flow solution (with a constant parabolic velocity profile) is an exact solution of the viscous, incompressible Navier-Stokes equations. It is of interest to consider what type of non-uniform solutions might exist besides this uniform solution. Approaches to the numerical solution of the Navier-Stokes equations for PPF have generally been of two types. In the first, the full time-dependent problem is solved, starting from some generally arbitrary initial condition (such as the uniform flow with a random two- or three-dimensional perturbation). This method has the characteristic of simulating the actual flow development in experiments and of finding only stable solutions if it converges to an equilibrium state. Recent work along these lines (e.g., Kleiser 1982, Kim 1983, Biringen 1984, Biringen and Maestrello, 1984, Krist and Zang, 1987) demonstrates that numerical simulations can successfully mimic experimental behavior and indicates also that true PPF is obtained in the experiments.

More importantly, perhaps, high resolution numerical simulations allow access to internal flow variables that would be prohibitively difficult and time consuming to measure in a physical experiment. Thus it becomes practical to examine the data for characteristic flow structures (such as hairpin vortices and high-shear regions) that have been observed or proposed before. Identification and examination of the time-evolution of such structures may lead to a better understanding of their role in the production of turbulence. However, even with the powerful computers available nowadays, resolution of the fine-scale in turbulence is still impossible. There also is little control over the flow development (particularly if several mechanisms are equally viable) and it is tedious to trace equilibrium solutions and stability characteristics in the multi-dimensional parameter space.

1.4 Vortical states

An alternative approach to the solution of the Navier-Stokes equation is to find steady equilibrium solutions and compute their stability. This method has the advantage of allowing greater control over the solutions discovered and has the further value of adding to the number of known steady solutions of the Navier-Stokes equations. It is relatively straightforward and intuitive to classify steady solutions in the form of a curve or surface in the relevant parameter space. Furthermore, the power of bifurcation theory can be brought to bear on the problem, perhaps suggesting further areas of investigation. As an example of the success of this approach, in Chapter 3, 2D STABILITY, we demonstrate the existence of at least two new families of unsteady but quasi-periodic solutions to the Navier-Stokes equations, discovered as bifurcations from a surface of 2D steady solutions.

Any attempt to understand transition and turbulence relies upon proposing and testing intuitively understandable models that explain the observed behavior. Time-dependent simulations are valuable in that they suggest or at least allow searching for coherent structures that might be part of such a model. In this spirit, Saffman (1983) has proposed the existence of so-called *vortical states* – simple solutions of the Navier-Stokes equations which would act as "attractors" for the turbulent flow in such a way that the existence of turbulence depends on the existence of these vortical states and that these states would display some of the properties of the turbulent flow.

The testing of such an intrinsically vague hypothesis necessitates finding such states with the desired turbulent properties before investigating how the turbulent flow might arise from them. The simplest class of vortical states are steady, finite-amplitude travelling waves in a viscous, incompressible flow and it is the search and study of such waves in PPF which motivates the research reported on in this thesis. We look for steady, travelling wave solutions, either periodic in the streamwise direction and uniform in the spanwise direction (2D waves) or periodic in both directions (3D waves). In both cases we look only for wave propagation in the streamwise direction. The primary objective is to find such solutions which exist at Reynolds numbers of the same order as the transition Reynolds number observed in PPF experiments. We map out solutions of these forms in the appropriate solution space and also consider their linear stability and, where possible, compare these results with experimental observations. We briefly summarize below the previous work done and the new material that is our contribution to this research.

1.5 2D steady waves

The first step in considering the non-uniform behavior of PPF is to examine its linear stability to streamwise wavelike disturbances. Rayleigh's criterion shows that inviscid PPF is stable. Heisenberg (1924) developed an asymptotic method that correctly dealt with the viscous "critical layer" in the flow and he computed a stability diagram. Lin (1944) refined the asymptotic expansions to obtain a critical Reynolds number ($\mathbf{Re}_{\mathrm{cr}}$), the maximum Reynolds number for which the flow is unconditionally stable. He found $\mathbf{Re}_{\mathrm{cr}}$=5300 at $\alpha = 1$, where α is the streamwise wave-number of the disturbance. The Orr-Sommerfeld equations, which describe the linear stability of PPF, were solved numerically by Thomas (1953), who obtained $\mathbf{Re}_{\mathrm{cr}}$=5780 at $\alpha = 1.02$. The difficulty in the numerical solution arises in correctly resolving the sharp boundary layers near the channel walls at $y = \pm h$. Orszag (1971) solved this problem by using an expansion in Chebyshev polynomials. All our calculations use the essentially equivalent *method of spectral tau collocation* for solving the governing ODEs. Using his method, Orszag obtained $\mathbf{Re}_{\mathrm{cr}}$=5772.22 at $\alpha = 1.02056$.

There is considerable discrepancy between this value and the transition Reynolds number observed experimentally ($\mathbf{Re} \approx 1000$). Furthermore, Nishioka *et al.* (1975) observed that using a very low turbulence level facility, uniform PPF could be maintained up to $\mathbf{Re}_{\mathrm{cr}}$ and above. Both these facts suggest that the observed transition at low Reynolds numbers is due to instability to finite amplitude disturbances.

Finite amplitude waves. In an effort to find finite amplitude disturbances, one investigates the effect of higher streamwise harmonics on neutral Orr-Sommerfeld disturbances, i.e., expands the streamwise dependence in N Fourier modes. Meksyn and Stuart (1951) used asymptotic methods to solve the equations formulated by Noether (1921). They obtained $\mathbf{Re}_{\mathrm{cr}}$=2510 at $\alpha = 1.22$. Zahn *et al.* (1974) solved the nonlinear equations numerically for $N = 1$ and $N = 2$ and found a neutral surface in $(\mathbf{Re}, \alpha, A)$ space. Herbert (1976,1977) used the spectral collocation technique to obtain a minimum of $\mathbf{Re}_{\mathrm{cr}}$=2935 at $\alpha = 1.323$ for $N = 4$. He also found good agreement with characteristics of steady waves observed in Nishioka's experiments.

In Chapter 2 we address ourselves to tidying up some aspects of the 2D calculations. We develop the governing equations and introduce the relevant dimensionless parameters. In particular we note there are at least two ways of defining the Reynolds number, each with different relevance when comparing theoretical results with experiments. To confirm the convergence results we compare results with $N = 1, 2, 4$ and 8 modes and also demonstrate the exponential decay of the modal energies for two calculations with $N = 13$ modes. Qualitatively good results are obtained with just $N = 1$ modes, and this fact is used as support for drawing conclusions from the low-resolution 3D calculations presented in Chapter 5.

We should note here another, semi-numerical, method of searching for waves of permanent form which might also be candidates for vortical states. Stewartson and Stuart (1971) developed the so-called Ginzburg-Landau equation to describe the weakly nonlinear evolution of 2D disturbances in PPF near $\mathbf{Re}_{\mathrm{cr}}$. Landman (1987) has studied this equation and found a variety of solutions, including not only the periodic, travelling waves mentioned above, but also other spatially periodic and quasi-periodic solutions and various types of solitary wave solutions. Although strictly these solutions are applicable only in the low amplitude regime, they suggest other classes of solutions for which to search in the fully nonlinear Navier-Stokes equations.

1.6 2D superharmonic stability of 2D secondary flows

In recent work on shear flow instability, the tacit assumption has been made that the two-dimensional stability of finite amplitude waves in plane Poiseuille flow follows a simple and well-understood pattern, namely one with a stability transition at the limit point in Reynolds number. Using numerical stability calculations we show that the application of heuristic arguments in support of this assumption has been in error, and that a much richer picture of bifurcations to quasi-periodic flows can arise from considering the two-dimensional superharmonic stability of such a shear flow.

1.7 3D stability

Since the experiments of Klebanoff *et al.* (1962) in the boundary layer first gave evidence of 3D instability of the 2D small-amplitude oscillations (Tollmien-Schlichting, or TS waves), various attempts have been made to explain the phenomena. Williams *et al.* (1984) summarized the observed behavior as involving ten stages, from the appearance of TS waves, their growth into the nonlinear regime, through the appearance of transverse periodic three-dimensionality, the formation of a high-shear layer and hairpin eddies, to local breakdown, the appearance of turbulent spots and finally full turbulence. This behavior has also been observed in PPF by Nishioka *et al.* (1975,1980,1981) which supports the contention that PPF models boundary layer phenomena.

Herbert (1983a) has summarized the various models used to explain the observed behavior, and for convenience we include here a summary based on his report, plus the work that has been done since his review article. Most of these models involve the linear or weakly nonlinear interaction of TS waves (Orr-Sommerfeld eigenfunctions) with 3D linear modes. Following Herbert's notation, we denote a general waveform as $A(\alpha, \beta, \omega)$ where ω is the frequency of the wave, and α, β are the streamwise and spanwise wave-numbers respectively of the disturbance.

Analytical models. Benney and Lin (1960) deduced the existence of a longitudinal vortex system after peak-valley splitting from the model $A(\alpha, 0, \omega_A) + B(\alpha, \beta, \omega_B)$. Synchronization ($\omega_A = \omega_B$) and thus resonance can apparently occur if the third-order governing equations are accounted for, and there is some experimental evidence for the phase difference $\omega_A - \omega_B$ existing prior to the formation of longitudinal vortices in the flow.

Craik (1971) proposed a resonant triad between TS wave and a subharmonic

3D wave: $A(\alpha, 0, \omega_A) + B(\alpha/2, \beta, \omega_B)$. Resonance occurs for a specific value of the spanwise wavenumber β. This resonance has been observed by Saric *et al.* (1980,1983,1984) in the boundary layer, but is inoperative for reasons of symmetry in PPF (Herbert and Morkovin, 1980).

Herbert and Morkovin (1980) considered the interaction of TS wave with longitudinal vortices, $A(\alpha, 0, \omega) + B(0, \beta, 0)$, at finite A. The TS wave destabilizes vortices with $\beta = O(1)$ with resulting dramatic growth of B for A greater than some small threshold amplitude. Although this agrees qualitatively with experiments, Herbert notes that the small region of validity of the expansions used in weakly-nonlinear models makes quantitative comparison with experiments difficult.

Numerical methods. Such analytical problems can be overcome by direct numerical computation of stability, either using Floquet theory or time-dependent simulations. In this case the temporal stability problem is solved (rather than the more experimentally comparable spatial stability problem) because of the infinite computational box (in principle) required for the latter case. On the other hand, in numerical computations it is no longer necessary to restrict oneself to small disturbances.

Orszag and Kells (1980) conducted a time dependent simulation for $500 \leq \mathbf{Re} \leq 3500$ for PPF. They noted (fortuitously) that PPF seemed explosively unstable to 3D perturbations at subcritical Reynolds numbers. Kleiser (1982) found similar behavior: 2D and 3D modes interact to give numerical/physical breakdown in situations where each mode would decay in isolation.

Orszag and Patera (1981) computed the stability of true equilibrium states (for $\mathbf{Re} > 2900$) and quasi-equilibria (via direct numerical simulation) down to $\mathbf{Re} = 1000$ for initial conditions $A_0(\alpha, 0, \omega) + C_0(0, \beta, 0)$ – longitudinal vortices with small C_0. Strong growth of $C(t)$ was found down to $\mathbf{Re} = 1000$ provided A_0 is sufficiently large and its 2D decay sufficiently small. It is the latter condition that fails for **Re** < 1000. Typical growth rates were 10-100 times those of the viscous primary instability.

Orszag and Patera (1983) proposed that the secondary instability of 2D secondary flows to 3D disturbances is a prototype of transitional instability in many wall-bounded shear flows. They computed the growth rates of many of these flows and found convective rates in qualitative agreement with those observed experimentally. Analysis of the energy transfer showed that the 2D wave mediates the transfer of energy from the mean flow to the 3D perturbation. The instability mechanism is basically inviscid, involving vortex stretching and tilting.

In Herbert (1983b) and other recent papers (1983c,1984), Herbert has emphasized the significance of subharmonic instabilities. Experiments in the boundary layer (Saric *et al.*, 1980,1983) revealed alternative routes to transition other than the peak-valley splitting observed by Klebanoff and characteristic of superharmonic instability. Herbert also reports an experiment by Kozlov (1982) in which subharmonic transition was observed in PPF. Numerical calculations show that subharmonic instability is active at lower threshold amplitudes than superharmonic, but with weaker growth rates. In some 2D amplitude range, both types of instability are viable ones for the breakdown of a 2D secondary flow and which appears naturally will depend on the nature of the background noise. Herbert has also extended the analysis to the Blasius boundary layer by use of the *shape assumption*, whereby the fundamental is assumed to be the principal mode eigenfunction of the Orr-Sommerfeld problem at the Reynolds number and α of interest. The computed velocity distributions from this method are in good agreement with experiment.

As Herbert (1983a) noted, little is known about the most dangerous cases ($\sigma_{\max}$ in terms of α, β and **Re**) and hence about general criteria for the most dangerous

β or for threshold amplitudes of the 2D secondary flow, at which the flow becomes unstable to 3D disturbances. In Chapter 4, 3D STABILITY OF 2D SECONDARY FLOWS we attempt to rectify this lack of knowledge for the superharmonic and subharmonic ($p = 1/2$) linear stability of 2D secondary flows. Because we use a Floquet approach, requiring a 2D equilibrium state, we do not consider cases with $\mathbf{Re} < 2600$. In doing so we extend the results of Orszag and Patera (1983) who reported superharmonic data for $\mathbf{Re} = 4000, \alpha = 1.25$ and Herbert (1983a) who shows calculations for various amplitudes at $\alpha = 1$. Subharmonic stability calculations have been reported for $\alpha = 1.02$ at $\beta = 2$ (Herbert, 1983b,c) and for isolated points on the 2D secondary flow solution surface.

Temporal vs. spatial stability. All the numerical studies considered above of necessity consider temporal stability, since spatial stability would involve (in principle) an infinite computational box. The relevance of applying such temporal stability results to the spatial stability measures in experiments has been often disputed and in this regard it is worth noting the work of Kleiser (1982). He numerically computed the time evolution of 2D flows for parameters as close as possible to the experimental conditions of Nishioka *et al.* (1978). Kleiser found not only the qualitative features of initial linear growth of the 3D disturbance, the formation of a high-shear layer and instantaneous inflexional velocity profiles, but also astonishing quantitative agreement of the instantaneous velocity profile with the experimental measurements up to the early stages of breakdown. Such agreement seems to support the contention that temporal stability computations are applicable to experiments.

1.8 **3D steady waves**

Given the known three-dimensionality of transition and turbulent PPF, and the success in reducing the Reynolds number to about **Re**=2400 by considering 2D finite amplitude disturbances, it is logical to consider whether three-dimensional steady waves (secondary flows) might exist at even lower Reynolds numbers.

Investigations of stability indicate the 2D secondary flows are unstable to both super- and subharmonic (with wavelength doubling) 3D disturbances. Points of neutral stability can be used to provide a bifurcation point onto the surface of 3D solutions. There is no evidence as yet, either experimentally or numerically, that such 3D secondary flows can be obtained (for instance with the growth of the 3D instability from the 2D secondary flow solution).

To our knowledge there have been no published reports of 3D superharmonic wave calculations. In Chapter 5, 3D STEADY WAVES, we compute the solution surfaces for some representative parameter values.

Subharmonic waves have been computed by Goldshtik *et al.* (1983) who used a low-resolution finite-difference method to compute steady solutions and reported they existed down to a Reynolds number of 1000, in agreement with the experimentally observed transition value. We have also performed this calculation and find low Reynolds number solutions when using low resolution. However at higher resolution there is a dramatic change in the qualitative behavior of the solutions.

1.9 Plane Poiseuille-Couette flow

Finally, in Chapter 6 we take a detour into the calculation of finite-amplitude solutions in Poiseuille-Couette flow. Although plane Couette flow is believed to be linearly stable for all Reynolds numbers (see Drazin and Reid, 1981 for a summary of the evidence), experiments by Reichardt (1956) suggest transition occurs at $\mathbf{Re} \approx 750$. It has been proposed that this disagreement would be explained by the existence of finite amplitude solutions in plane Couette flow, existing either as isolas or as bifurcations from infinity. One approach to finding such solutions is to compute finite amplitude solutions in PPF and then continue these into Poiseuille-Couette flow by increasing the wall velocity from zero. One can then investigate reducing the pressure gradient to zero while maintaining a finite wall velocity. The corresponding flow would be a finite amplitude solution in plane Couette flow. Toplosky and Akylas (1987) have recently attempted (and failed) to find finite amplitude states in non-rotating pipe flow using a similar technique. They used finite amplitude states in rotating pipe flow as a starting point for their calculations but could not continue these down to zero rotation rate. In Chapter 6 we report on the results of such an investigation using the 3D superharmonic flows as a starting point for Poiseuille-Couette flow.

CHAPTER 2

2D STEADY WAVES

2.1 Problem formulation

Consider the incompressible Navier-Stokes equations written in stream-function formulation:

$$\frac{\partial \nabla^2 \Psi}{\partial t} + \Psi_y \nabla^2 \Psi_x = \Psi_x \nabla^2 \Psi_y + \nu \nabla^4 \Psi. \tag{2.1}$$

We look for steady, periodic travelling waves moving down the channel shown in Figure 2.1 with wave speed c in the streamwise direction x.

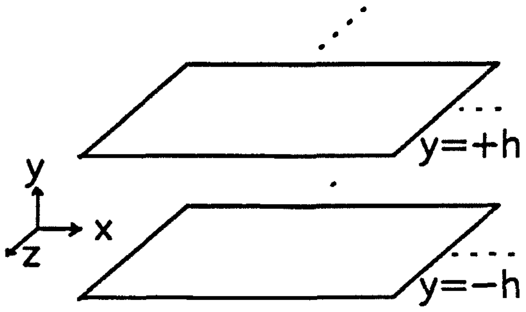

FIGURE 2.1. Definition sketch for PPF.

With the transformation $\Psi(x,y,t) = \Psi(\tilde{x},y)$ (where $\tilde{x} = x - ct$) and $\Psi(\tilde{x},y) = \Psi_{\mathrm{PPF}}(y) + \psi(\tilde{x},y)$ (where $\Psi_{\mathrm{PPF}} = U_0(y - y^3/3h^2)$ is the stream-function of the uniform PPF, and ψ is the perturbation of the disturbed flow away from this basic flow), and also nondimensionalizing by the channel half-width h and the characteristic velocity U_0, we have the perturbation equation

$$-\frac{1}{\mathbf{Re}}\nabla^4\psi + (U_{\mathrm{PPF}} - c)\nabla^2\psi_x - U''_{\mathrm{PPF}}\psi_x + \psi_y\nabla^2\psi_x - \psi_x\nabla^2\psi_y = 0, \tag{2.2}$$

where $\mathbf{Re} = hU_0/\nu$, $U_{\mathrm{PPF}} = \Psi_{\mathrm{PPF},y}$ and for convenience we now write x for $\tilde{x}$. We solve this by spectrally decomposing (2.2) in the x-direction, writing

$$\psi(x,y) = \sum_{n=-\infty}^{+\infty} \hat{\psi}_n(y) e^{i\alpha n x}. \tag{2.3}$$

Note that $\hat{\psi}_0$ is a perturbation to the uniform PPF. For reality of $\psi(x,y)$ we require

$$\hat{\psi}_{-n}(y) = \hat{\psi}_n^*(y) \tag{2.4}$$

which allows us to solve only for the non-negative modes, $n \geq 0$.

The modal equations corresponding to (2.2) for mode n are

$$\begin{aligned} -\frac{1}{\mathbf{Re}} \left(S_x^4 + 2S_x^2 \frac{d^2}{dy^2} + \frac{d^4}{dy^4} \right) \hat{\psi}_n + (U_{\mathrm{PPF}} - c) \left(S_x^2 + \frac{d^2}{dy^2} \right) S_x \hat{\psi}_n - U''_{\mathrm{PPF}} S_x \hat{\psi}_n \\ + \hat{\psi}_y * \left(S_x^2 + \frac{d^2}{dy^2} \right) S_x \hat{\psi} - (S_x \hat{\psi}) * \left(S_x^2 + \frac{d^2}{dy^2} \right) \frac{d\hat{\psi}}{dy} = 0, \end{aligned} \tag{2.5}$$

where $S_x f_n = i\alpha n f_n$ and the convolution $f * g$ for mode n is defined as $f * g = \sum_{q=-\infty}^{+\infty} f_{n-q} g_q$. The corresponding modal boundary conditions deduced from no-slip at the channel walls are

$$\begin{aligned} n > 0 \qquad & \hat{\psi}_{n,y}(\pm 1) = 0 \quad (u_n(\pm 1) = 0) \\ & \hat{\psi}_n(\pm 1) = 0 \quad (v_n(\pm 1) = 0) \end{aligned} \tag{2.6}$$

$$n = 0 \qquad \hat{\psi}_{0,y}(\pm 1) = 0 \quad (u_0(\pm 1) = 0).$$

The boundary condition on v_0 is automatically satisfied (since $v_0 = (i\alpha 0)\hat{\psi}_0 \equiv 0$ everywhere). $\hat{\psi}_0$ is arbitrary to within a constant so we set

$$\hat{\psi}_0(-1) = 0. \tag{2.7}$$

This leaves one boundary condition undetermined. This corresponds to having not yet chosen the nondimensionalizing velocity U_0, and to a resulting indeterminacy in $\hat{\psi}_0$. Thus the last boundary condition may be regarded as fixing the parametrization of the problem. Two reasonable choices would be either to fix the flux (Q), i.e., put

$$\left[\Psi_{\mathrm{PPF}} + \hat{\psi}_0\right]_{-h}^{+h} = Q \tag{2.8a}$$

or to fix the pressure gradient (P), i.e., put

$$\left[\Psi_{\mathrm{PPF},yy} + \hat{\psi}_{0,yy}\right]_{-h}^{+h} = \frac{2Ph}{\nu} \tag{2.8b}$$

where equations (2.8) should be read as relating dimensional quantities for the moment. With (2.8a) as the last boundary condition, we set $U_0 \equiv U_Q$ where U_Q is the centerline velocity of the uniform PPF having the same flux Q as our disturbed flow. Thus $\Psi_{\mathrm{PPF}} = U_Q(y - y^3/3h^2)$ and, after nondimensionalizing by U_Q and h and using (2.7), (2.8a) becomes

$$\text{Flux boundary condition:} \qquad \hat{\psi}_0(+1) = 0. \tag{2.9a}$$

Similarly, using (2.8b) and setting $U_0 \equiv U_P$, where U_P is the centerline velocity of the uniform PPF having the same pressure gradient P as our disturbed flow, (2.8b) becomes

$$\text{Pressure boundary condition:} \qquad \left[\hat{\psi}_{0,yy}\right]_{-1}^{+1} = 0. \tag{2.9b}$$

Boundary conditions (2.9a) and (2.9b) represent the extremes of a continuous range. Solutions satisfying (2.9a) will have zero flux perturbation but finite pressure perturbation; as the flux perturbation $\hat{\psi}_0(+1)$ is increased the pressure perturbation $[\hat{\psi}_{0,yy}]_{-1}^{+1}$ decreases to zero where (2.9b) holds.

Equations (2.4)-(2.7) and (2.9) constitute a nonlinear eigenvalue problem for the unknown phase speed c. There is a phase indeterminacy in the solution $\hat{\psi}_n (n \geq 0)$ because if $\hat{\psi}_n$ is a solution, so is $\hat{\psi}_n e^{in\alpha\delta}$ (for arbitrary δ). This corresponds to a $-\delta$ shift of the origin in the x-direction. Thus for a given eigenvalue c of the equations, there corresponds a one-dimensional space of eigensolutions $\hat{\psi}_n e^{in\alpha\delta}$. To remove this indeterminacy we impose a phase condition of the form

$$I \int_{-1}^{+1} \hat{\psi}_1(y)dy = 0, \tag{2.10}$$

where I denotes the imaginary part of a complex number. This may be regarded as the extra equation required to determine the unknown eigenvalue c in the equations.

Flux and pressure Reynolds numbers. Corresponding to the two different nondimensionalizing velocities are two different Reynolds numbers, $\mathbf{Re_Q}$ and $\mathbf{Re_P}$. Their explicit dependence on the flux Q and pressure gradient P is easily determined as

$$\begin{aligned} Q = [\Psi_{\mathrm{PPF}}]_{-h}^{+h} &= \frac{4U_Q h}{3}, \\ \mathbf{Re_Q} = \frac{hU_Q}{\nu} &= \frac{3Q}{4\nu} \end{aligned} \tag{2.11a}$$

and

$$\begin{aligned} P = \frac{\nu}{2h}[\Psi_{\mathrm{PPF},yy}]_{-h}^{+h} &= \frac{-2\nu U_P}{h^2}, \\ \mathbf{Re_P} = \frac{hU_P}{\nu} &= \frac{-h^3 P}{2\nu^2} \end{aligned} \tag{2.11b}$$

It is important to note that the differing boundary conditions alter only the scaling of the problem, not the the physics. For a given disturbed flow, there are unique perturbation stream-functions $\hat{\psi}_{Q0}$ and $\hat{\psi}_{P0}$ which differ by a multiple of the base PPF and the scaling factor U_Q/U_P. The dimensional representation of the *total* mean flow is

$$\Psi_{\mathrm{PPF}} + \hat{\psi}_0 \equiv U_Q\left(y - \frac{y^3}{3h^2}\right) + \hat{\psi}_{Q0} = U_P\left(y - \frac{y^3}{3h^2}\right) + \hat{\psi}_{P0}.$$

Nondimensionalizing by h and U_Q, U_P respectively:

$$\begin{aligned}\hat{\psi}_{P0} &= \left(\frac{U_Q}{U_P} - 1\right)\left(y - \frac{y^3}{3}\right) + \left(\frac{U_Q}{U_P}\right)\hat{\psi}_{Q0} \\ &= \left(\frac{\mathbf{Re_Q}}{\mathbf{Re_P}} - 1\right)\left(y - \frac{y^3}{3}\right) + \left(\frac{\mathbf{Re_Q}}{\mathbf{Re_P}}\right)\hat{\psi}_{Q0}. \end{aligned} \tag{2.12}$$

This can be used to determine the relationship between the two Reynolds numbers by substituting (2.12) into the boundary condition (2.9b)

$$\mathbf{Re_P} = \mathbf{Re_Q}\left(1 - \frac{1}{4}\left[\hat{\psi}_{0Q,yy}\right]_{-1}^{+1}\right). \tag{2.13}$$

These are only the same for the uniform (PPF) flow and generally $\mathbf{Re_P} = f(\mathbf{Re_Q}, \alpha)$ with $\mathbf{Re_P} > \mathbf{Re_Q}$ (Saffman 1983, Rozhdestvensky and Simakin, 1984) for the 2D secondary flows we are considering. It seems that in experiments it is generally easier to compute the flux and thus $\mathbf{Re_Q}$. On the other hand, most computational results have been presented in terms of the pressure Reynolds number $\mathbf{Re_P}$. In this work, unless otherwise noted, all quantities are nondimensionalized by U_Q and results presented in terms of $\mathbf{Re_Q}$.

2.2 Numerical solution method

Equations (2.4)-(2.10) constitute a set of nonlinear ODEs for the disturbance stream-function $\hat{\psi}_n(y)$ and two of the three parameters $(\mathbf{Re_Q}, \alpha, c)$ (the other one being fixed). To solve these ODEs, we truncate the system at some N, and keep modes $n = 0, \ldots, N$. No aliasing from higher Fourier modes is introduced by this truncation because the original spectral decomposition was exact. To solve this truncated set of ODEs, we use the method of spectral tau collocation (See Orszag and Gottlieb, 1977 for the theoretical details of this method). Here the unknown function $\hat{\psi}_n(y)$ is represented as a sum of known functions in y; to accurately resolve the boundary layers in PPF we choose an expansion in Chebyshev modes:

$$\hat{\psi}_n(y) = \sum_{k=0}^{K} a_{nk} T_k(y), \tag{2.14}$$

where $T_k(y) = \cos k(\cos^{-1} y)$. To compute derivatives, we differentiate the Chebyshev modes: e.g., $d\hat{\psi}_n/dy = \sum a_{nk}T_k'(y)$. After substituting this representation into (2.5), the resulting algebraic equations (in a_{nk}, $n = 0, \ldots, N; k = 0, \ldots, K$) are evaluated at the maxima ($\theta_j = j\pi/K$, $y_j = \cos\theta_j$; $j = 0, \ldots, K$) of the Kth Chebyshev mode $T_K(\theta) = \cos K\theta$. This choice minimizes the aliasing in y for linear equations and is suggested by Orszag and Gottlieb (1977) for nonlinear equations also.

Evaluating (2.5) at the $K - 1$ interior points ($\theta_j = j\pi/K$; $j = 1 \ldots, K - 1$), and the four boundary conditions (2.6),(2.7) and (2.9) at their limits, provides $K+3$ equations (for each Fourier mode n) for the $K + 1$ Chebyshev coefficients a_{nk}. To correct this deficiency we introduce the so-called tau factors $\tau_{n,K+1}, \tau_{n,K+2}$ into the interior equations and solve instead

$$(2.5) \quad + \quad \tau_{n,K+1}T_{K+1}(y) + \tau_{n,K+2}T_{K+2}(y) = 0 \qquad (2.15)$$

These tau factors are the first two terms in an infinite series $\sum_{k=K+1}^{\infty} \tau_{nk}T_k(y)$ which measures the discretization error of the approximation (2.14) in solving the equations.

Euler-Newton continuation. Newton's Method was used locally to solve the nonlinear algebraic system of equations $F_i(\mathbf{a}, \mathbf{Re_Q}, \alpha, c) = 0$. To find an initial guess to the solution we used an Euler estimate from a previous solution. The mathematical basis for this method is given in Keller (1977). Our implementation is illustrated in Figure 2.2a, where some characteristic norm of the solution is plotted against the continuation parameter (in this case $\mathbf{Re_Q}$). We find the tangent vector ($\dot{\mathbf{a}}_{\mathrm{A}}$) to the solution curve at A and compute the Euler guess $\mathbf{a}_{\mathrm{Euler}} = \mathbf{a}_{\mathrm{A}} + \Delta\dot{\mathbf{a}}_{\mathrm{A}}$, where Δ is some appropriate step size. Using this as the first estimate for Newton's Method, we iterate into the solution curve at Z, subject to the additional constraint that the Newton iterates B,C,... lie on a perpendicular to the tangent vector $\dot{\mathbf{a}}_{\mathrm{A}}$. This method automatically follows the solution curve round a fold such as that at A′. If a specific value of $\mathbf{Re}_{\mathbf{Q}}$ is desired, the "simple" continuation method shown in Figure 2.2b is used, where we set $\mathbf{a}_{\mathrm{Euler}} = \mathbf{a}_{\mathrm{A}}$ (but change the value of the parameter $\mathbf{Re}_{\mathbf{Q}}$).

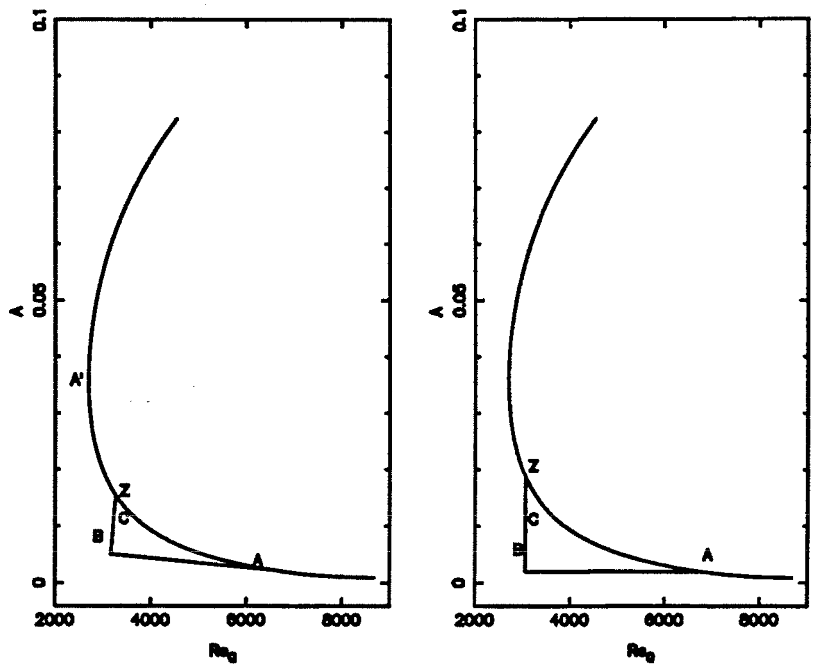

(a) Euler–Newton continuation

(b) "Simple" continuation

FIGURE 2.2. Continuation methods used. (a) Euler-Newton, (b) "Simple"

The most "expensive" computational parts of the algorithm are the calculation of the Jacobian $[F_{ij}] = [\partial F_i/\partial a_j]$ and its LU decomposition (each of which takes about the same time). To save time, the Jacobian was reused from one Newton iteration to the next if the error norms (see below) were smaller than certain tolerances. In addition, because of the form of the continuation methods shown in Figure 2.2, the Jacobian computed for the final Newton step to Z could be used to compute the tangent vector at Z for the next Euler estimate. This can not be done generally with other forms of Euler-Newton continuation.

Convergence criteria. Two norms were used to judge convergence of Newton's Method. The first measures the error in the equations and the second the error in the solution vector. It was assumed the Newton iterates were converged when both the criteria

$$\|F_i\|_2 \leq tol \tag{2.16a}$$

and

$$\left\| \frac{\delta a_i}{tol_{\mathrm{abs}} + tol_{\mathrm{rel}}|a_i|} \right\|_1 \leq 1 \tag{2.16b}$$

were satisfied. Generally we took $tol_{\mathrm{abs}} = tol_{\mathrm{rel}} = tol = 10^{-6}$. The condition (2.16b) ensures that the change (δa_i) in each component of the solution vector $\mathbf{a}$ satisfies a relative error criterion $|\delta a_i / a_i| \leq \textit{tolerance}$ when a_i is large, and an absolute error criterion $|\delta a_i| \leq \textit{tolerance}$ when a_i is small.

Amplitude and energy. It is sometimes convenient to continue in some characteristic amplitude of the disturbance. A natural definition is related to the energy flux of the disturbance:

$$\begin{aligned} A_E^2 = \sum_{n=-N}^{+N}{}' E_n &= \frac{15}{16} \sum_{n=-N}^{+N}{}' \int_{-1}^{+1} |u_n(y)|^2 + |v_n(y)|^2 dy \\ &= \frac{15}{16} \sum_{n=-N}^{+N}{}' \int_{-1}^{+1} |\hat{\psi}_n'(y)|^2 + |i\alpha n \hat{\psi}_n(y)|^2 dy. \end{aligned} \tag{2.17}$$

Note that this does not include the $n = 0$ mode energy, because that would involve a contribution from the basic flow $(\hat{\Psi}_{\mathrm{PPF}}(y))$ as well as the perturbation to the basic flow $(\hat{\psi}_0(y))$. The 15/16 factor results from the nondimensionalization, and makes the basic flow energy $E_{\mathrm{PPF}} = 1$. The integral in (2.17) is transformed to an integral in θ (where $y = \cos\theta$) and computed using the trapezoidal rule at the collocation points $\theta_j = j\pi/K; \quad j = 0, \ldots, K$. This is spectrally accurate; i.e., the quadrature does not introduce any additional truncation error.

A_E is an inconvenient quantity to compute at every Newton iteration if continuation in amplitude is desired. For this purpose we define a characteristic amplitude equal to the L_2-norm of the $n > 0$ Chebyshev coefficients

$$A^2 = \sum_{n=-N}^{+N}{}' \sum_{k=0}^{K} |a_{nk}|^2, \tag{2.18}$$

which is much easier to compute and seems to scale directly with the energy amplitude A_E; see Figure 2.3 which shows the amplitudes for numerically computed 2D secondary flows for a representative wave number.

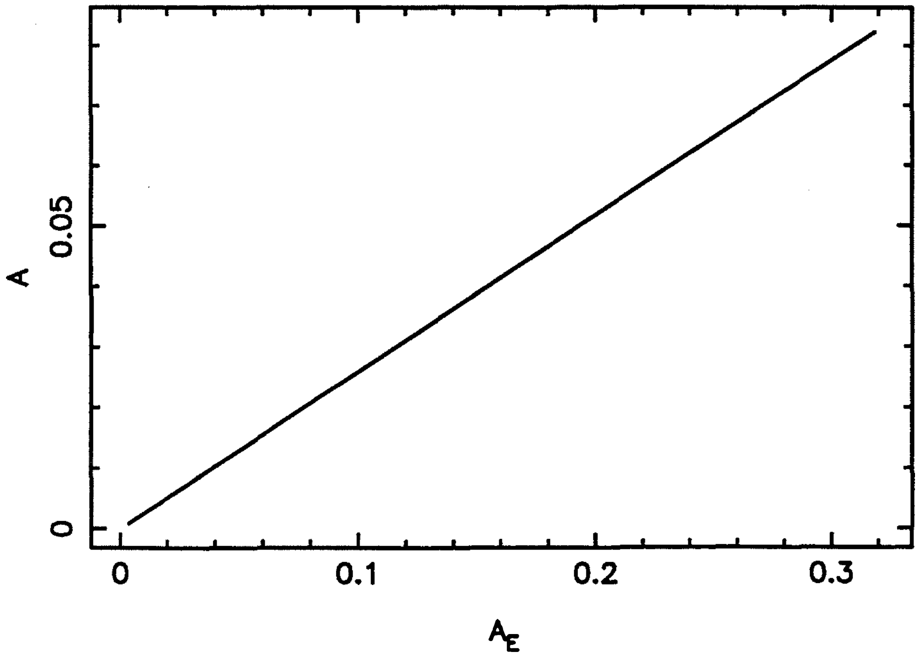

FIGURE 2.3. Comparison of energy amplitude A_E and characteristic amplitude A.

tative behavior (particularly the minimum in $\mathbf{Re_P}$) is present at $N = 1$. In contrast to these excellent results of the spectral method, the pseudo-spectral method (Milinazzo and Saffman, 1985) does not recover this minimum until $N \approx 4$. In Figure 2.4, we compare the E-α cross-section at $\mathbf{Re_P} = 4000$, computed with $N = 1, 2, 4$ and 8, with that of Herbert (1976).

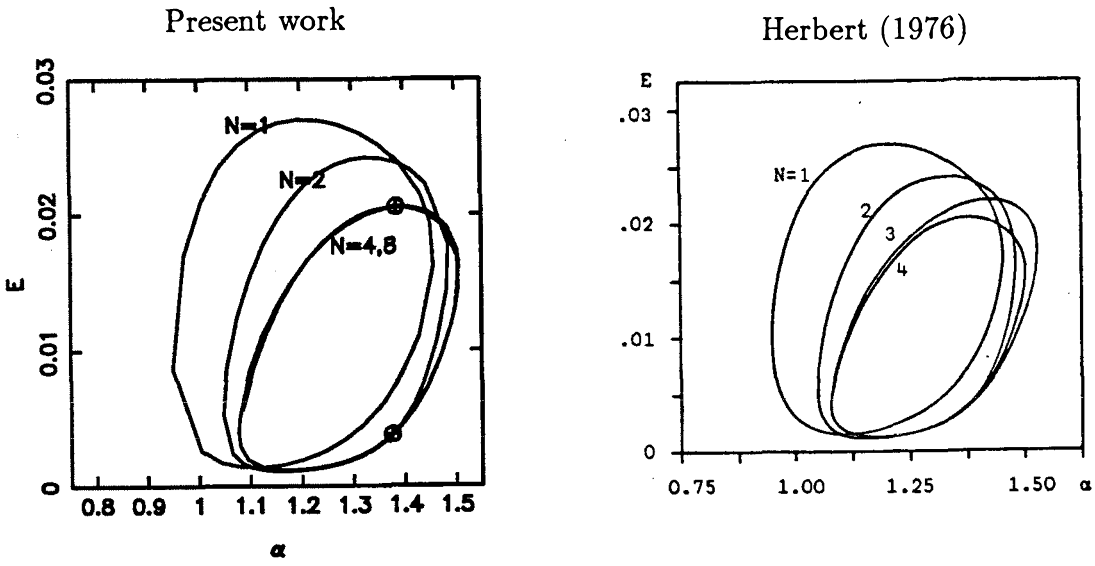
Present work

Herbert (1976)

FIGURE 2.4. Comparison of E-α cross-section at $\mathbf{Re_P} = 4000$. Energies of present work have been scaled to U_P nondimensionalization used by Herbert (1976). Symbols ($\oplus$) show positions of $N = 13$ calculations.

Finally in Table 2.2 we show the modal energies E_n computed with $N = 13$ Fourier modes at $\mathbf{Re_P} = 4000$ for both high and low energies (symbols on Figure 2.4). The energies decay exponentially as expected, and the drop-off in modal energies from E_1 to E_2 ($E_2/E_1 \approx 10^{-3}$) suggests that meaningful results can be obtained with $N = 1$. This point will become more important when we consider 3D steady waves where the size of the system precludes computations with more than

TABLE 2.2. Modal energies computed with $N = 13$ modes

Mode	High energy	Low energy
0	0.99916216	1.0068871
1	3.71613957×10^{-2}	4.28038059×10^{-3}
2	1.06207962×10^{-4}	3.34394083×10^{-6}
3	2.38598938×10^{-5}	1.88078445×10^{-6}
4	8.24742857×10^{-7}	4.95660020×10^{-8}
5	1.76731292×10^{-6}	3.20950278×10^{-8}
6	5.61103956×10^{-7}	4.66200370×10^{-9}
7	2.10982201×10^{-7}	$8.24330839\times 10^{-10}$
8	1.95767996×10^{-7}	$3.05190843\times 10^{-10}$
9	7.40410062×10^{-8}	$5.79105117\times 10^{-11}$
10	5.76822387×10^{-8}	$1.86701174\times 10^{-11}$
11	3.39377293×10^{-8}	$4.29953707\times 10^{-12}$
12	2.38647464×10^{-8}	$1.18960406\times 10^{-12}$
13	2.41571204×10^{-8}	$4.84792340\times 10^{-13}$

$N = 1$ or $N = 2$.

In Appendix I, we plot cross-sections of the 2D secondary flow surface for various values of α, as computed with $N = 1$ and $N = 2$ Fourier modes. These may be used to compute the Reynolds numbers $(\mathbf{Re_Q}, \mathbf{Re_P})$ and characteristic amplitudes (A, A_E) given, for instance, the parameters used by other authors.

CHAPTER 3

2D STABILITY OF 2D SECONDARY FLOWS

3.1 Introduction

We are concerned with the 2D stability of 2D steady waves (secondary flows) in plane Poiseuille flow (PPF), to infinitesimal perturbations of the same wavelength as the secondary flow (i.e., superharmonic disturbances). The secondary flows have been computed by a number of authors in recent years (e.g., Zahn *et al.*, 1974, Herbert, 1976, Milinazzo and Saffman, 1985) and stability analyses of them have focused on the 3D stability problem. One reason is because three-dimensional perturbations grow on a convective time-scale as opposed to the slower growth of two-dimensional disturbances (Orszag and Patera, 1983).

Nevertheless, the 2D superharmonic stability problem is not without interest. In Figure 3.1 we sketch a cross-section (at a representative streamwise wavenumber α) of the 2D secondary flow surface, with a characteristic amplitude plotted against a characteristic Reynolds number for the flow. Orszag and Patera (1981) have used a one-dimensional phase representation of the energy† to predict that the lower branch of the 2D solution curve is unstable and the upper branch is stable to 2D superharmonic disturbances. This stability transition (by which we mean where $\max_{\sigma} R\sigma = 0$) at the "nose" or limit point in Reynolds number is illustrated in Figure 3.1. They admitted that their argument in support of this prediction is oversimplified and we shall demonstrate by numerical examples that it is not in general correct. In §3.2 we formulate the 2D stability problem for the 2D secondary flows

---

† Details are not given in their paper, and we have been unable to reproduce the argument in any rigorous fashion.

mentioned above. There exist neutrally stable eigenmodes (i.e., with $\sigma = 0$) at the nose, whose existence will be proved in §3.3, but as shown by the numerical results presented in §3.4 these coexist with unstable modes. Further, we will demonstrate that there are bifurcations to quasi-periodic flows on the upper branch of the solution curve of Figure 3.1.

The picture of stability transition in Figure 3.1 is complicated by the lack of uniqueness in the parametrization of the 2D flows. As explained in §2.1, two possible choices are a flux Reynolds number ($\mathbf{Re_Q}$) and a pressure Reynolds number ($\mathbf{Re_P}$). In Figure 3.2 we have plotted both $\mathbf{Re_Q}$ and $\mathbf{Re_P}$ curves for a representative α; it is to be understood that only horizontal lines (same amplitude) correspond to the same flow (e.g., at $A = 0.05$, $\mathbf{Re_Q} = 2850$ and $\mathbf{Re_P} = 3650$).

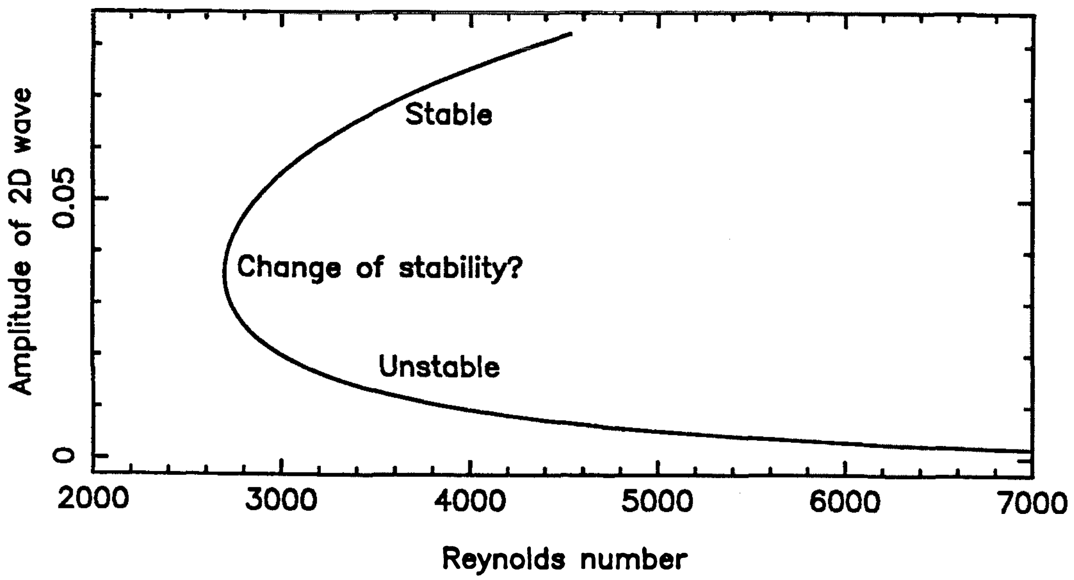

FIGURE 3.1. Naive prediction of stability transition on 2D secondary flow solution curve.

The figure is sketched for a wave-number for which PPF is linearly unstable.

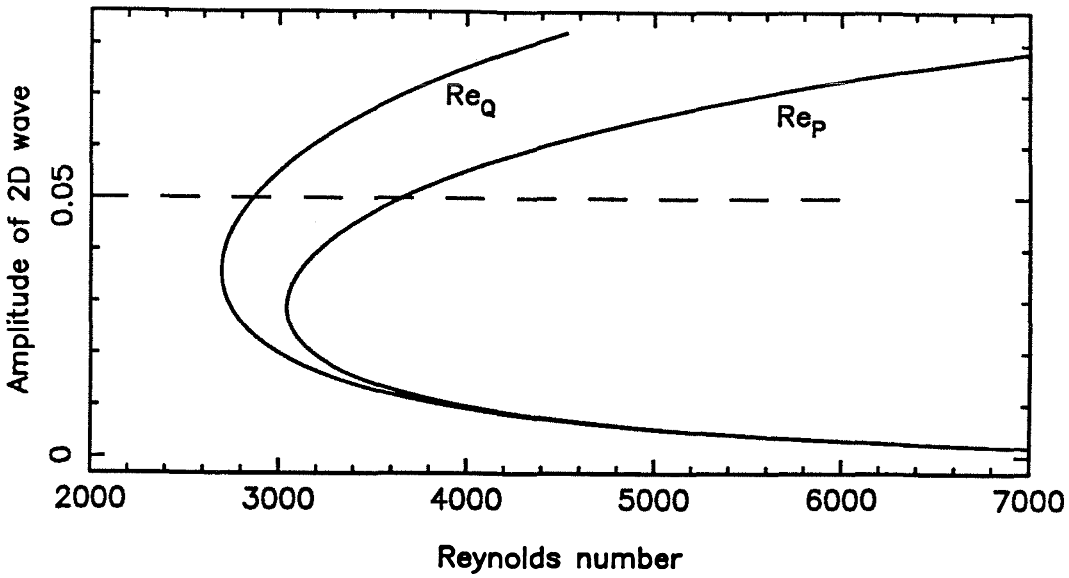

FIGURE 3.2. Comparison of pressure ($\mathbf{Re_P}$) and flux ($\mathbf{Re_Q}$) Reynold numbers (for $\alpha = 1.1$).

A contradiction is reached if the Orszag and Patera energy argument is applied to the linear stability of the 2D secondary flows. If a stability transition is expected at the nose of the $\mathbf{Re_Q}$ curve (as the argument suggests) then it would occur on the upper branch of the $\mathbf{Re_P}$ curve; if expected at the nose of the $\mathbf{Re_P}$ curve then the corresponding point would be on the lower branch of the $\mathbf{Re_Q}$ curve.

If, moreover, the argument is applied to individual eigenmodes another question arises. At minimum amplitude on the 2D solution curve one can expect one unstable eigenvalue. The existence of a zero growth-rate eigenvalue ($R\sigma = 0$, where R denotes the real part of a complex number), at the nose could then correspond to three situations as the amplitude is increased:

(i) The unstable eigenvalue becomes stable at the nose.

(ii) Another (previously stable) eigenvalue becomes unstable at the nose.

(iii) Another (previously stable) eigenvalue becomes unstable on the lower branch and then one of the unstable eigenvalues goes stable at the nose.

Note that only in case (i) does one expect a stability transition.

Thus there are two problems to be considered: To which Reynolds number parametrization does the Orszag and Patera argument apply (if any)? Is the nose a stability transition ($\max\limits_{\sigma} R\sigma = 0$), a zero growth-rate point for an individual eigenvalue ($R\sigma = 0$) or a point of neutral stability ($\sigma = 0$)?

3.2 Problem formulation

The dimensionless form of the 2D Navier-Stokes equations (2.1), for a streamfunction perturbation in a moving reference frame (speed c) is

$$\frac{\partial \nabla^2 \psi}{\partial t} - \frac{1}{\mathbf{Re}} \nabla^4 \psi + (\psi_y - c)\nabla^2 \psi_x - \psi_x \nabla^2 \psi_y = 0. \tag{3.1}$$

We look for solutions of the form

$$\psi(x, y, t) = \Psi_{\mathrm{PPF}}(y) + \psi_{\mathrm{2D}}(x, y) + \epsilon \zeta(x, y, t), \tag{3.2}$$

where ψ_{2D} describes the 2D secondary flows discussed in the previous section. Equation (3.1) is separable in time, so applying the normal mode concept we write

$$\zeta(x, y, t) = e^{\sigma t} \sum_{n=-\infty}^{+\infty} \hat{\zeta}_n(y) e^{in\alpha x}, \tag{3.3}$$

where $R\sigma$ is the growth rate of the (superharmonic) disturbance and α is the streamwise (x-direction) wavenumber of the 2D secondary flow. Substituting (3.3) and the similar spectral representation (with basis functions $\hat{\Psi}_{\mathrm{2D}}$) for $\Psi_{\mathrm{2D}} = \Psi_{\mathrm{PPF}} + \psi_{\mathrm{2D}}$ into (3.1), and linearizing about the basic state ($\epsilon = 0$), we obtain the 2D stability equations for the nth Fourier mode

$$-\frac{1}{\mathbf{Re}}(S_x^4 \hat{\zeta}_n + 2S_x^2 \hat{\zeta}_{n,yy} + \hat{\zeta}_{n,yyyy}) + S_x((U - c)(S_x^2 \hat{\zeta}_n + \hat{\zeta}_{n,yy}) - U'' \hat{\zeta}_n)$$

$$
\begin{aligned}
&+\hat{\Psi}_y * (S_x(S_x^2\hat{\zeta} + \hat{\zeta}_{yy})) + \hat{\zeta}_y * (S_x(S_x^2\hat{\Psi} + \hat{\Psi}_{yy})) \\
&-(S_x\hat{\Psi}) * (S_x^2\hat{\zeta}_y + \hat{\zeta}_{yyy}) - (S_x\hat{\zeta}) * (S_x^2\hat{\Psi}_y + \hat{\Psi}_{yyy}) \qquad = -\sigma(S_x^2\hat{\zeta}_n + \hat{\zeta}_{n,yy}) \quad (3.4)
\end{aligned}
$$

where $U(y) = 1 - y^2, \quad y \in (-1, +1)$. We now fix the characteristic velocity as $U_0 = U_Q$ (and thus $\mathbf{Re} \equiv \mathbf{Re_Q}$); this also affects the form of the 2D flow $\hat{\Psi}_{\mathrm{2D}}$. It is straightforward to show that the eigenvalues are either real or occur in complex conjugate pairs. The accompanying boundary conditions are

$$
\begin{aligned}
n \neq 0 \qquad & \hat{\zeta}_{n,y}(\pm 1) = 0 \quad (u_n(\pm 1) = 0) \\
& \hat{\zeta}_n(\pm 1) = 0 \quad (v_n(\pm 1) = 0)
\end{aligned}
$$

$$
n = 0 \qquad \hat{\zeta}_{0,y}(\pm 1) = 0 \quad (u_0(\pm 1) = 0). \qquad (3.5)
$$

The boundary condition on v_0 is again automatically satisfied. $\hat{\zeta}_0$ is arbitrary to within a constant so we set

$$
\hat{\zeta}_0(-1) = 0. \qquad (3.6)
$$

Equations (3.4)-(3.6) describe an infinite set of 2D disturbances, the form of which is specified by the final boundary condition. Two reasonable choices might be

$$
\hat{\zeta}_0(+1) - \hat{\zeta}_0(-1) = 0 \qquad \text{(Constant flux)} \qquad (3.7a)
$$

or

$$
\hat{\zeta}_{0,yy}(+1) - \hat{\zeta}_{0,yy}(-1) = 0 \qquad \text{(Constant pressure).} \qquad (3.7b)
$$

Equations (3.7a) and (3.7b) are only two of many possibilities for boundary conditions. One can look for solutions of a particular y-symmetry; both antisymmetric

($\hat{\zeta}_n(-y) = (-1)^{n+1}\hat{\zeta}_n(+y)$) and symmetric ($\hat{\zeta}_n(-y) = (-1)^n\hat{\zeta}_n(+y)$) disturbances satisfy the equations. In fact all computed eigensolutions appear to be of one of these two forms for constant flux disturbances. Note that (3.7a) and (3.7b) are both satisfied identically for symmetric disturbances.

To solve the set of ODEs and boundary conditions in (3.4)-(3.7) we applied the technique of spectral collocation and wrote $\hat{\zeta}_n(y) = \sum_{k=0}^{K} a_{nk}T_k(y)$ where $T_k(y)$ is the kth Chebyshev polynomial. Evaluating the resulting equations at the maxima of the Kth Chebyshev polynomial (as suggested in Orszag and Gottlieb, 1977) yielded a (discrete) generalized eigenvalue problem of the form $\mathrm{G}\mathbf{a} = \sigma\mathrm{B}\mathbf{a}$ for the complex eigenvalue σ and the associated eigenvector $\mathbf{a}$. This was solved using standard numerical methods.

3.3 Eigensolutions with $\sigma = 0$

Phase-shift solution. If we substitute $\psi \equiv \Psi_{2\mathrm{D}}$ (as defined in §3.2) into (3.1) the nonlinear equation for the 2D secondary flow can be written

$$-\frac{1}{\mathbf{Re}}\nabla^4\Psi_{2\mathrm{D}} + (\Psi_{2\mathrm{D},y} - c)\nabla^2\Psi_{2\mathrm{D},x} - \Psi_{2\mathrm{D},x}\nabla^2\Psi_{2\mathrm{D},y} = 0 \tag{3.8}$$

which is of the form

$$N(\Psi_{2\mathrm{D}}(x,y), \mathbf{Re}, \alpha, c) = 0 \tag{3.9}$$

and we can derive the 2D stability equations (3.4) in a formal manner. A general unsteady solution $\Psi_{2\mathrm{D}}(x,y) + \epsilon e^{\sigma t}\zeta(x,y)$ satisfies

$$\left.\frac{\partial}{\partial\epsilon}\right|_{\epsilon=0} N(\Psi_{2\mathrm{D}}(x,y) + \epsilon e^{\sigma t}\zeta(x,y), \mathbf{Re}, \alpha, c) = \frac{\partial\nabla^2(e^{\sigma t}\zeta(x,y))}{\partial t} \tag{3.10}$$

whence

$$\frac{\delta N}{\delta\Psi}\zeta = \sigma\nabla^2\zeta. \tag{3.11}$$

Also, differentiating (3.9) in the x-direction

$$\frac{\delta N}{\delta \Psi}\frac{\partial \Psi}{\partial x} = 0 \tag{3.12}$$

and comparing (3.11) and (3.12) shows that the eigenvalue $\sigma = 0$ is always a solution of the stability equations, with associated eigenfunction $\zeta_{ps} = \partial\Psi/\partial x$. (We note that this also satisfies the boundary conditions on ζ, regardless of the choice of boundary condition for mode $n = 0$). We can call this the *phase-shift solution*, since it represents the trivial 2D "disturbance" caused by shifting a known 2D secondary flow along the x-axis.

Neutral stability at the "nose". We want to show now that there is an additional zero eigenvalue at the nose of the appropriate $\mathbf{Re}$ curve; on the $\mathbf{Re_P}$ curve for constant pressure (P) disturbances and on the $\mathbf{Re_Q}$ curve for constant flux (Q) disturbances. Furthermore, the eigenfunction corresponding to this zero eigenvalue is also the phase-shift eigenfunction; that is, at the nose there is a zero eigenvalue of algebraic multiplicity 2 and geometric multiplicity 1 (which we will denote for brevity as AM 2, GM 1).

Consider (3.9), at some fixed α, parametrized by some arclength s:

$$N(\Psi, \mathbf{Re}, c; s) = 0,$$

where $\Psi \equiv \Psi_{2\mathrm{D}}$ for convenience. Differentiating this along the solution curve

$$\begin{aligned}\frac{dN}{ds} &\equiv \frac{\delta N}{\delta \Psi}\frac{d\Psi}{ds} + \frac{\partial N}{\partial \mathbf{Re}}\frac{d\mathbf{Re}}{ds} + \frac{\partial N}{\partial c}\frac{dc}{ds} \\ &= N_\Psi \dot{\Psi} + N_{\mathbf{Re}}\dot{\mathbf{Re}} + N_c \dot{c} = 0. \end{aligned}\tag{3.13}$$

At the limit point ("nose") in $\mathbf{Re}$, $\dot{\mathbf{Re}} = 0$, whence

$$N_\Psi \dot{\Psi} = -\dot{c} N_c. \tag{3.14}$$

If $\dot{c} = 0$, then $\sigma = 0$ is a second eigenvalue of the stability problem (3.11), with associated eigenfunction $\zeta = \dot{\Psi}$ (the "tangent vector"), where $\dot{\Psi}$ satisfies appropriate boundary conditions. In this case we have AM 2 and GM 2 (i.e., index one). But in general $\dot{c} \neq 0$, and then $\dot{\Psi}$ is a generalized eigenfunction for the phase-shift eigenfunction $\zeta_{ps} \equiv \partial\Psi/\partial x$.

To see this, note that from (3.8), $N_c \equiv -\nabla^2 \frac{\partial}{\partial x}\Psi = -\nabla^2 \zeta_{ps}$ whence (3.14) implies

$$N_\Psi \phi = \nabla^2 \zeta_{ps}, \tag{3.15}$$

where $\phi = \dot{\Psi}/\dot{c}$ satisfies the same boundary conditions as ψ (because $\dot{\Psi} = \dot{\Psi}_{\mathrm{PPF}} + \dot{\psi} = \dot{\psi}$). That is, on the $\mathbf{Re_Q}$ curve

$$\hat{\phi}_n(\pm 1) = \hat{\phi}'_n(\pm 1) = 0 \tag{3.16a}$$

and on the $\mathbf{Re_P}$ curve

$$\begin{aligned} &n > 0 \qquad & \hat{\phi}_n(\pm 1) &= \hat{\phi}'_n(\pm 1) = 0 \\ &n = 0 \qquad & \hat{\phi}_0(-1) = [\hat{\phi}''_0]^{+1}_{-1} &= \hat{\phi}'_0(\pm 1) = 0, \end{aligned} \tag{3.16b}$$

where $\hat{\phi}_n(y) = \dot{\hat{\psi}}_n/\dot{c}$.

Suppose now we have a generalized eigenvalue problem, $S\xi = \sigma T\xi$, with $\sigma = 0$ an eigenvalue of GM 1 and AM 2 and associated eigenfunction $\xi = \eta$. Then the resolvent $(S - \sigma T)^{-1}$ has a double pole at $\sigma = 0$ (Kato, 1966). If

$$(S - \sigma T)^{-1} = \left(\frac{1}{\sigma^2} + \frac{A_1}{\sigma} + A_0 + \cdots\right)$$

then

$$(S - \sigma T)\left(\frac{1}{\sigma^2} + \frac{A_1}{\sigma} + A_0 + \cdots\right)\eta = \eta.$$

Equating powers of σ:

$$\frac{1}{\sigma^2}: \qquad S\eta = 0 \tag{3.17}$$

$$\frac{1}{\sigma}: \qquad SA_1\eta - T\eta = 0 \tag{3.18}$$

With $S \equiv N_\Psi, T \equiv \nabla^2$ and $\eta \equiv \zeta_{ps}$, (3.12) satisfies (3.17) and (3.15) satisfies (3.18), where $\phi \equiv A_1 \zeta_{ps}$. Thus there is an eigenvalue $\sigma = 0$ of GM 1 and at least AM 2 at the nose $\dot{\mathbf{Re}} = 0$†.

To which **Re** this corresponds depends on the particular stability problem being solved. On the $\mathbf{Re_Q}$ curve, ψ satisfies (2.6), (2.7) and (2.9a), and thus (3.16a) is satisfied. By (3.7a), these are just the conditions for the Q-stability problem. A similar argument applies to the $\mathbf{Re_P}$ curve. In summary we find constant flux disturbances have a zero eigenvalue (with algebraic multiplicity 2 and geometric multiplicity 1) at the nose of the $\mathbf{Re_Q}$ curve, and constant pressure disturbances have a zero eigenvalue (i.e., neutral stability) at the nose of the $\mathbf{Re_P}$ curve. The associated eigenfunction is the phase-shift solution ζ_{ps}.

The contradictory conclusions reached by applying the Orszag and Patera energy argument can thus be reconciled if one accounts for a non-uniqueness in the form of the 2D disturbance considered in the stability problem; it has to be of a form appropriate to the particular Reynolds number parametrization.

3.4 Numerical results

The above results are illustrated for 2D stability at various points along the solution curve for $\alpha = 1.1$. The curve appears to bifurcate from infinity for this wavenumber. Calculations show that the behavior at $\alpha = 1$ (where the curve bifurcates from $\mathbf{Re_Q} \approx 5800$) is similar to that shown here. The 2D secondary flows were computed with $N = 1$ Fourier modes in the x-direction and $K = 50$ Chebyshev modes in the y-direction. The 2D stability was computed with $N = 1, K = 32$ and $N = 1, K = 50$ (at high Reynolds numbers). The resolution in x is insufficient to give more than qualitative results. A number of calculations with $N = 2$ (for both secondary flow and stability) indicate that although the positions of the bifurcation

---

† We are grateful to Tim Minzoni for showing us this improvement upon our previous proof.

points change from $N = 1$ to $N = 2$, the nature of the bifurcation and $I\sigma$ at the bifurcation point remain the same. The secondary flows and stability calculations were performed on a VAX-11/750; calculation of all the eigenvalues of the stability problem for one secondary flow took about 10 minutes CPU time for $N = 1, K = 32$ and 40 minutes for $N = 2, K = 32$. The secondary flows themselves took 1-5 minutes and 5-30 minutes for $N = 1, K = 50$ and $N = 2, K = 50$ respectively, the exact time depending on the number of Newton iterations necessary.

We first consider constant flux disturbances ("Q-stability") (boundary condition (3.7a)) and plot the maximum growth rate (max $R\sigma$) in Figure 3.3. The maximum eigenvalue is purely real in the Reynolds number range shown. At the nose of the $\mathbf{Re_Q}$ curve this eigenvalue passes through zero and consequently there is a stability transition. However on the $\mathbf{Re_P}$ curve this stability transition occurs on the "upper branch", after the nose is reached. Of course the actual flow where this stability transition occurs (and the amplitude of that flow) is the same. Although a stability transition occurs at the $\mathbf{Re_Q}$ nose, the upper branch does not remain stable. As is shown in Figure 3.4, a different eigenvalue becomes unstable at $\mathbf{Re_Q} = 6300$. Because this eigenvalue has $I\sigma \neq 0$ at the zero growth-rate point ($R\sigma = 0$), a Hopf bifurcation to a family of travelling wave solutions occurs. Combined with the underlying steady travelling wave, this is a bifurcation to a spatially periodic flow with two frequencies (quasi-periodic) in time. Jimenez (private communication, 1986) has used an unsteady code for $\alpha = 1$ to follow this bifurcation and has found quasi-periodic flows, period-doublings and evidence of chaos. The Reynolds number increases along the stable branch of quasi-periodic solutions, as is expected for a supercritical Hopf bifurcation.

Turning now to constant pressure disturbances ("P-stability") (boundary condition (3.7b)), we might expect a similar behavior; a stability transition at the $\mathbf{Re_P}$

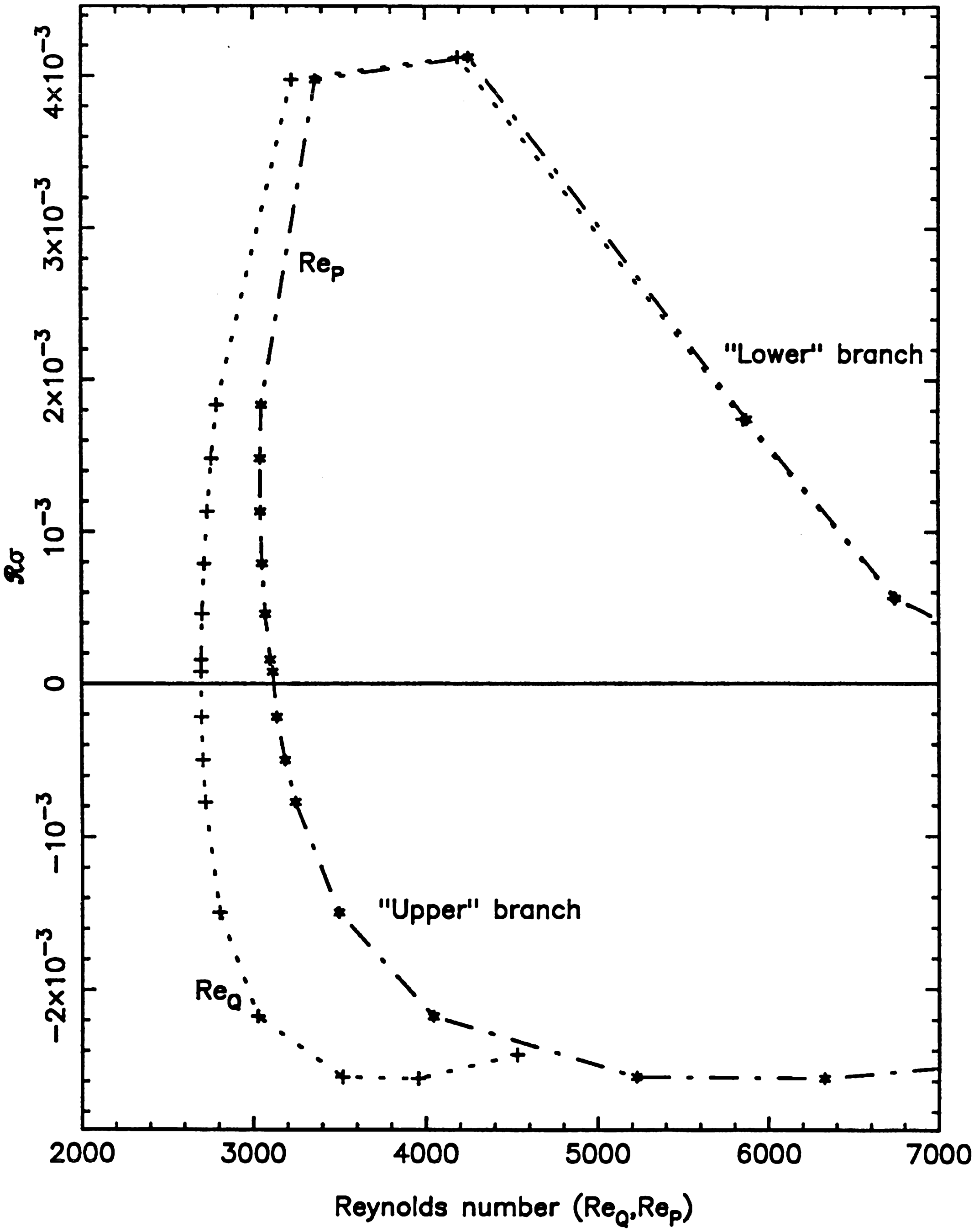

FIGURE 3.3. Maximum growth rate (max $R\sigma$) for 2D Q-stability, for $\alpha = 1.1$.

The most unstable eigenvalue is always purely real ($I\sigma = 0$) in this case.

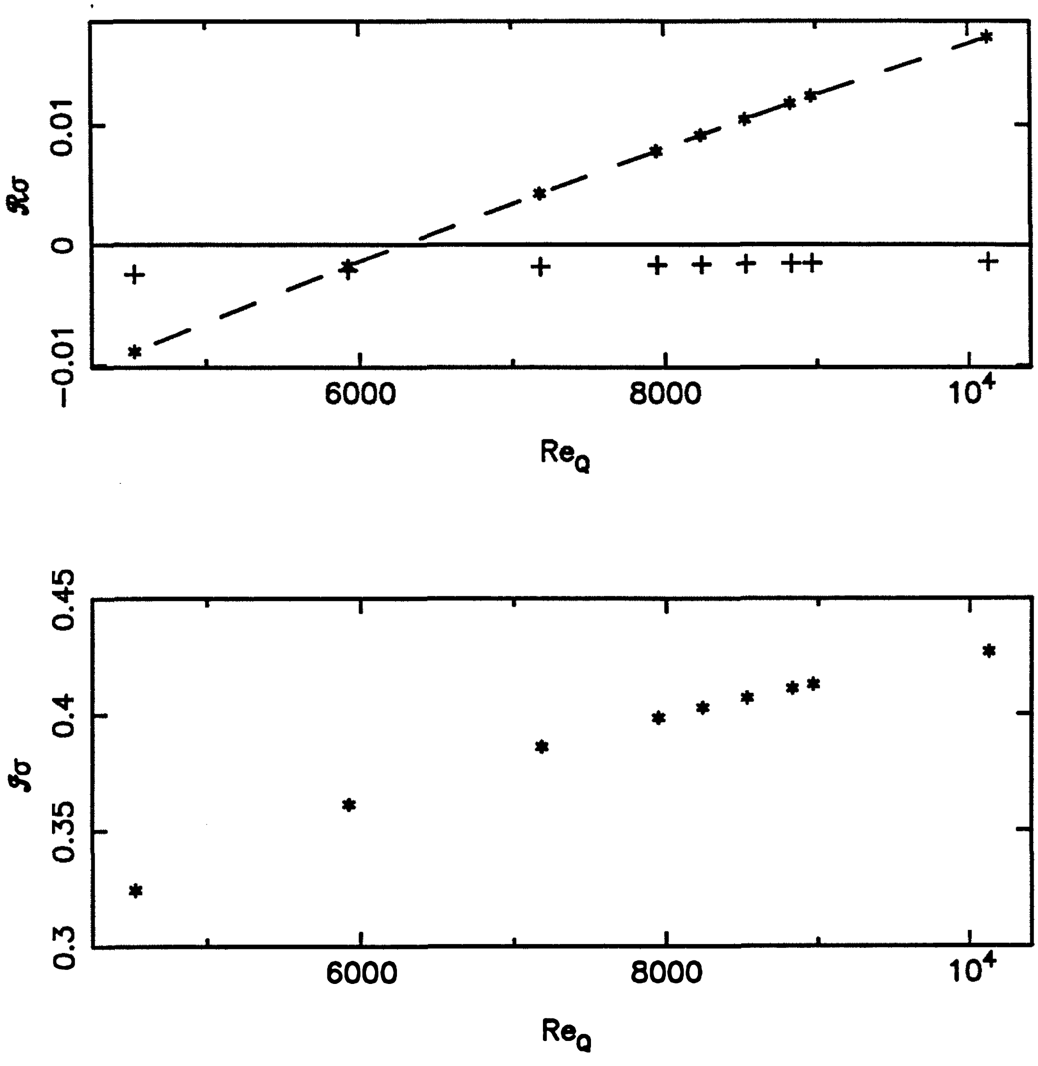

FIGURE 3.4. Stability transition for Q-disturbances, on upper branch, for $\alpha = 1.1$.

This is a continuation of Figure 3.3; the most unstable (real) eigenvalue at $\mathrm{Re_Q} = 4530$ (+ in both figures) is overtaken by another (complex) eigenvalue ($*$) at $\mathrm{Re_Q} = 5920$.

nose and at some point on the lower branch of the $\mathbf{Re_Q}$ curve (because the nose of the $\mathbf{Re_Q}$ curve occurs at higher amplitude than that of the $\mathbf{Re_P}$ curve). At least at $\alpha = 1.1$ this does not occur. As Figure 3.5 illustrates, the maximum eigenvalue remains unstable on the lower branch and part of the upper branch of the $\mathbf{Re_P}$ curve. Thus no stability transition occurs at the $\mathbf{Re_P}$ nose.

As expected from §3.3, however, there is a neutrally stable eigenvalue at the nose of the $\mathbf{Re_P}$ curve. Figure 3.6 shows the three most unstable eigenvalues. At low amplitude there is only one (real) unstable eigenvalue. At the nose there is a zero eigenvalue as predicted, but it is that of another mode becoming unstable. On the upper branch these two unstable real modes coalesce to form a complex conjugate pair with $R\sigma \rightarrow 0$ at $A = 0.047$, where $\mathbf{Re_P} = 3500$ (the nose occurs at $A = 0.028, \mathbf{Re_P} = 3041$). Since $I\sigma \neq 0$ at this point, this is a bifurcation to a quasi-periodic flow, but at a significantly lower Reynolds number ($\mathbf{Re_Q} = 2800$ at the bifurcation point) than for constant flux disturbances. Thus the upper branch becomes stable to P-disturbances with increasing Reynolds number. Since the theory of Hopf bifurcations (Marsden and McCracken, 1976) predicts that a supercritical bifurcation from this point would be stable, this raises the possibility of this bifurcation leading to stable quasi-periodic flows at lower Reynolds numbers (possibly smaller than the minimum for 2D secondary flows).

Note that the principal eigenvalues plotted in Figures 3.3-3.6 are associated with asymmetric or antisymmetric eigensolutions. If, on the other hand, the maximum eigenvalues corresponded to symmetric eigensolutions, satisfying both flux and pressure boundary conditions identically (§3.2), there would be no difference in the stability behavior of constant flux and constant pressure disturbances.

3.5 Summary

We have examined the 2D superharmonic stability of 2D secondary flows in

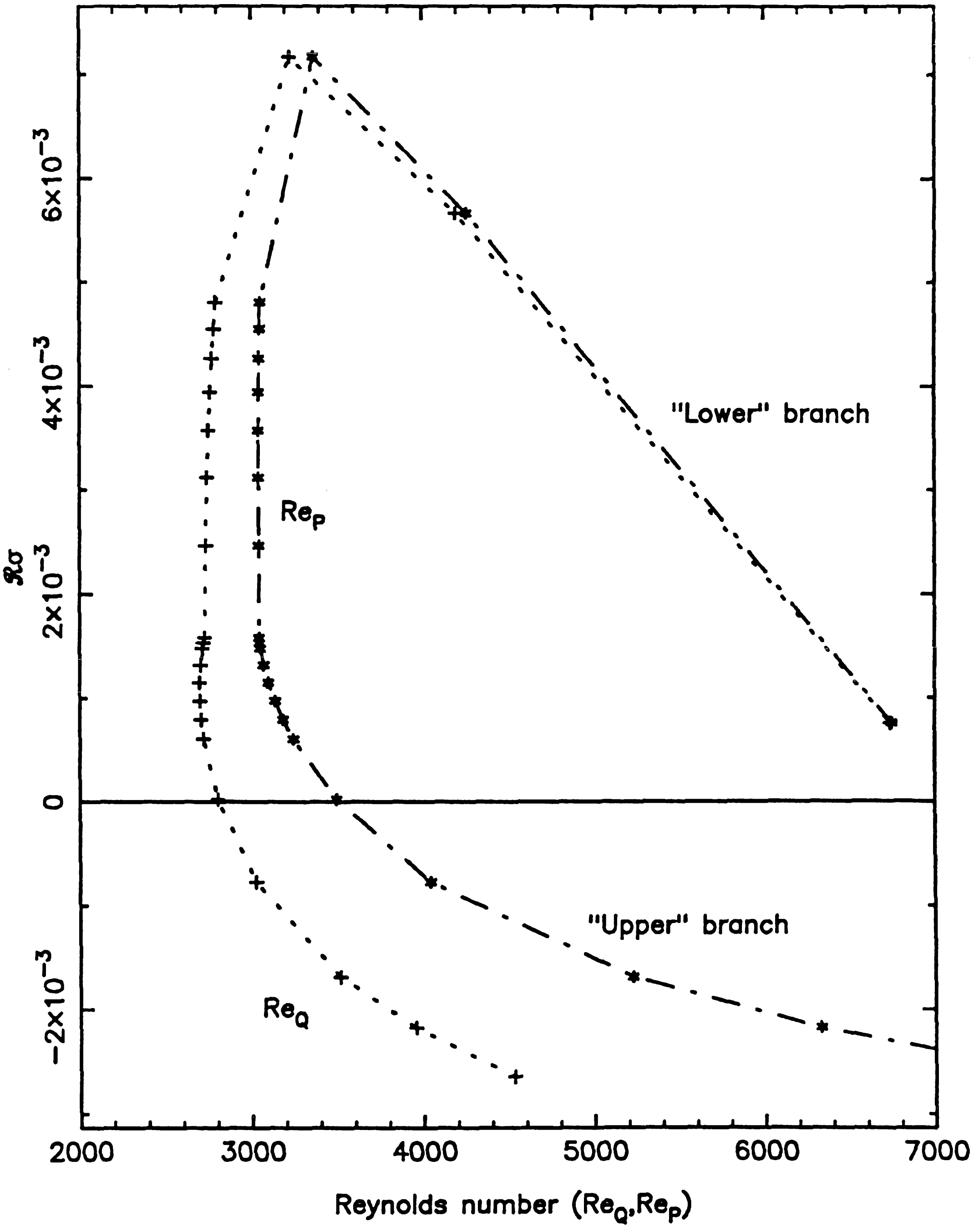

FIGURE 3.5. Maximum growth rate (max $R\sigma$) for 2D P-stability, for $\alpha = 1.1$.

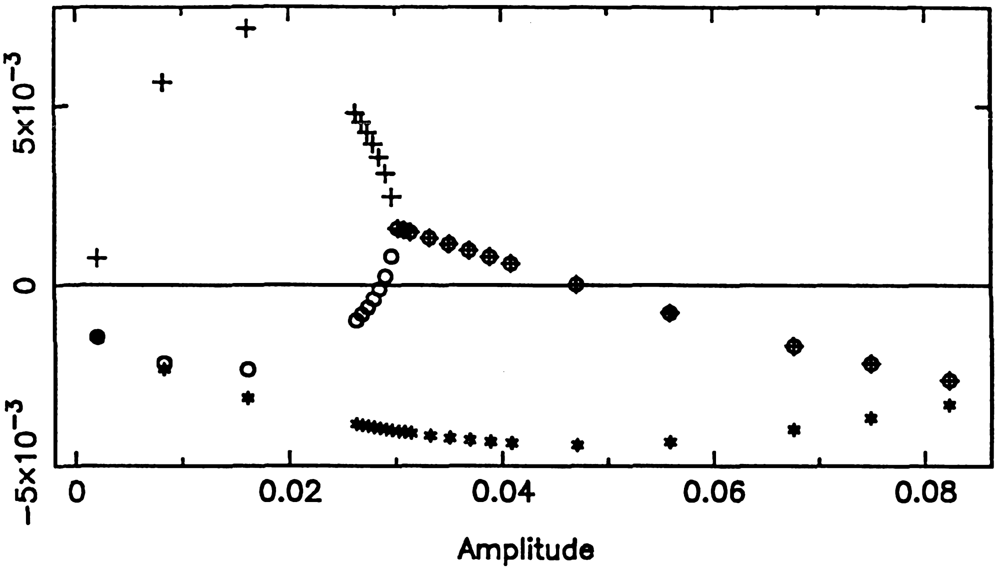

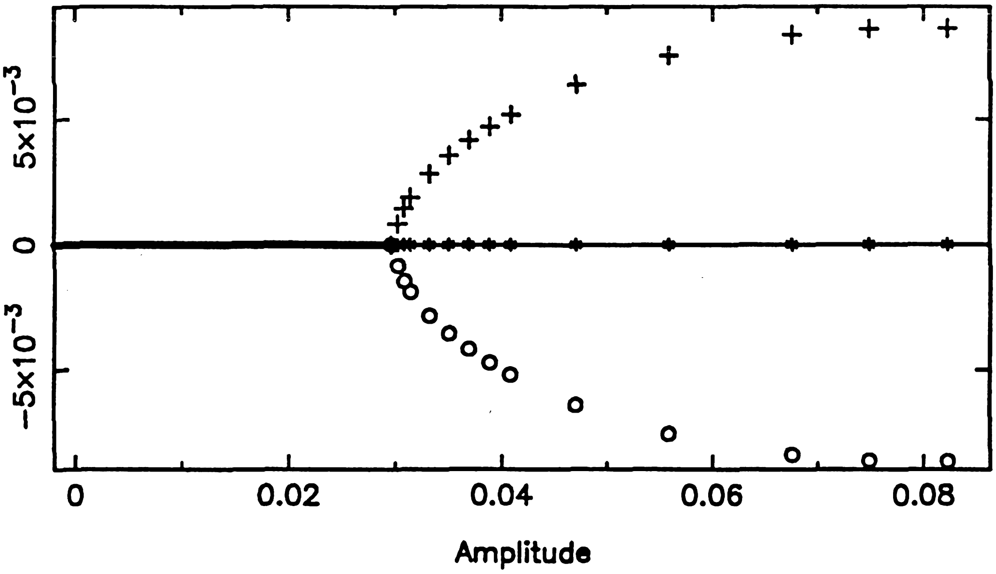

FIGURE 3.6. Stability transition for P-disturbances, on upper branch, for $\alpha = 1.1$. The nose occurs at $A = 0.028, \mathrm{Re_P} = 3041$ and the bifurcation at $A = 0.047, \mathrm{Re_P} = 3500, \mathrm{Re_Q} = 2800$. The heavy line for $A < 0.028$ indicates that $I\sigma = 0$ for the eigenvalues shown.

plane Poiseuille flow. Previously simplistic energy arguments have been used to predict (incorrectly) a stability transition at the "nose" of the 2D solution curve. A neutrally stable eigenvalue ($\sigma = 0$) does occur at the "nose" of the 2D curve, at least if one considers 2D disturbances of a form appropriate to the particular curve Reynolds number. However, this does not necessarily correspond to a change from unstable to stable for this eigenvalue as the amplitude increases. Furthermore, a stability transition will not occur at the nose if other eigenvalues remain unstable at this point.

It was found that the neutrally stable eigenvalue at the nose is of algebraic multiplicity 2 and geometric multiplicity 1, with the corresponding eigenfunction just the phase-shift solution. The proof of this is general, and should apply to other systems where the stability of travelling waves to travelling disturbances of the form (3.3) is considered. Numerical evidence of the above assertions is given for a streamwise wavenumber of $\alpha = 1.1$. Eigenvalues with zero growth-rate ($R\sigma = 0$) were found on the upper branch of the 2D secondary flow curve for both constant flux and constant pressure disturbances; because $I\sigma \neq 0$ when $R\sigma = 0$, these are bifurcations to quasi-periodic flows.

We have not investigated the stability behavior at higher Reynolds numbers to ascertain whether the upper branch restabilizes to Q-disturbances or destabilizes to P-disturbances, and we have not followed the quasi-periodic flows shed at the bifurcation points. Nevertheless, the stability behavior of the 2D secondary flows and the nature of the Hopf bifurcations give a much richer picture of possible instabilities instead of the accepted one of a simple stability transition at the nose of the 2D secondary flow curve.

CHAPTER 4

3D STABILITY OF 2D SECONDARY FLOWS

4.1 Introduction

As discussed in §1.7, experimental studies of the evolution of TS waves in boundary layer flows and PPF indicate that they are explosively unstable to 3D disturbances. This instability acts on a convective time scale, with growth rates 10-100 times as large as those of the primary instability (which controls the growth of the TS waves).

Orszag and Patera (1981,1983) investigated the 3D stability of both true equilibrium states (2D secondary flows) and also of so-called quasi-equilibria which exist for $\mathbf{Re} < 2700$. Herbert (1983c) noted the importance of subharmonic stability in both the boundary layer and PPF and computed some stability results. However, the size of the parameter space (with, for instance, variable $\alpha, \mathbf{Re}$ and β) makes it difficult to conduct any exhaustive search. By restricting ourselves to the consideration of 2D secondary flows, we have computed their superharmonic and subharmonic stability flows for a range of parameters and are thus able to draw out the trends in the instability growth rate with the above parameters.

This work is also a prerequisite for finding neutral stability points (where $\sigma \equiv 0$) and thus bifurcations to 3D steady flows, which forms the subject of Chapter 5.

4.2 **3D superharmonic stability: Problem formulation**

The 2D stability problem can be formulated in terms of a stream-function perturbation; in the 3D case a primitive-variable formulation must be used. We consider disturbances of the form

$$\mathbf{u}(x,y,z,t) = (U_{\mathrm{PPF}} - c)\mathbf{i} + \mathbf{U}_{2\mathrm{D}} + \epsilon e^{\sigma t}\mathbf{u}_{3\mathrm{D}}(x,y,z), \tag{4.1}$$

where x is in the moving frame of reference (speed c) and the phase speed ($I\sigma$) of the disturbance is thus measured relative to the travelling wave, $U_{\mathrm{PPF}} = 1 - y^2$, and $\mathbf{U}_{2\mathrm{D}}$ is the previously computed 2D secondary flow. The 3D incompressible Navier-Stokes equations are, in their vorticity formulation

$$\frac{\partial \boldsymbol{\omega}}{\partial t} + (\mathbf{u}\cdot\nabla)\boldsymbol{\omega} - (\boldsymbol{\omega}\cdot\nabla)\mathbf{u} - \frac{1}{\mathbf{Re}}\nabla^2\boldsymbol{\omega} = 0, \tag{4.2}$$

where $\boldsymbol{\omega} = \xi\mathbf{i} + \eta\mathbf{j} + \zeta\mathbf{k} = \boldsymbol{\nabla}\times\mathbf{u}$.

We substitute (4.1) in (4.2), linearize about the basic state ($\epsilon = 0$) and choose $U_0 = U_Q$ (and thus $\mathbf{Re} \equiv \mathbf{Re_Q}$). Combining the x and z vorticity equations and using continuity of the basic flow $U_x + V_y = 0$ yields the 3D stability equations:

$$\begin{aligned}\frac{1}{\mathbf{Re_Q}}\nabla^4 v - \left(\frac{\partial^2}{\partial x^2} + \frac{\partial^2}{\partial z^2}\right)(Uv_x + uV_x + Vv_y + vV_y)&\\ + \frac{\partial}{\partial x}((uU_y)_x + Uu_{xy} + Vu_{yy} + U_y v_y + vU_{yy})&\\ + \frac{\partial}{\partial z}(U_y w_x + Uw_{xy} + V_y w_y + Vw_{yy}) &= \sigma\nabla^2 v,\end{aligned} \tag{4.3}$$

$$\begin{aligned}\frac{1}{\mathbf{Re_Q}}\nabla^2(u_z - w_x) + \frac{\partial}{\partial x}(Uw_x + Vw_y)&\\ - \frac{\partial}{\partial z}(Uu_x + uU_x + Vu_y + vU_y) &= \sigma(u_z - w_x),\end{aligned} \tag{4.4}$$

$$u_x + v_y + w_z = 0, \tag{4.5}$$

with boundary conditions $u(\pm 1) = v(\pm 1) = w(\pm 1) = 0$. For convenience, we have written $U = U_{2\mathrm{D}} + (U_{\mathrm{PPF}} - c)$.

The stability equations are separable in z, so we look for a spectral decomposition of the form

$$\mathbf{u}_{3\mathrm{D}}(x, y, z) = e^{i\beta z} \sum_{n=-\infty}^{+\infty} \hat{\mathbf{u}}_n(y) e^{i\alpha n x}. \tag{4.6}$$

Substituting in the equations (4.3)-(4.5), with a spectral representation for $(U, V) : (\hat{U}_n, \hat{V}_n) = (\hat{\psi}'_n, i\alpha n\hat{\psi}_n)$ (where ψ is the streamfunction for the total 2D secondary flow of Chapter 2), and zeroing termwise (by modes) we obtain the stability equations for mode n

$$\begin{aligned}
&\frac{1}{\mathbf{Re_Q}}\left((S_x^2 + S_z^2)^2 + 2(S_x^2 + S_z^2)\frac{d^2}{dy^2} + \frac{d^4}{dy^4}\right) v_n \\
&- (S_x^2 + S_z^2)(U * v_x + u * V_x + V * v_y + v * V_y) \\
&+ S_x((u * U_y)_x + U * u_{xy} + V * u_{yy} + U_y * v_y + v * U_{yy}) \\
&+ S_z(U_y * w_x + U * w_{xy} + V_y * w_y + V * w_{yy}) = \sigma\left(S_x^2 + S_z^2 + \frac{d^2}{dy^2}\right) v_n,
\end{aligned} \tag{4.7}$$

$$\begin{aligned}
&\frac{1}{\mathbf{Re_Q}}(S_x^2 + S_z^2 + \frac{d^2}{dy^2})(S_z u_n - S_x w_n) + S_x(U * w_x + V * w_y) \\
&- S_z(U * u_x + u * U_x + V * u_y + v * U_y) = \sigma(S_z u_n - S_x w_n),
\end{aligned} \tag{4.8}$$

$$\text{Continuity:} \quad S_x u_n + v_{n,y} + S_z w_n = 0, \tag{4.9}$$

$$\text{Boundary conditions:} \quad u_n(\pm 1) = v_n(\pm 1) = w_n(\pm 1) = 0, \tag{4.10}$$

where $S_x f_n = i\alpha n f_n, S_z f_n = i\beta f_n$, but for brevity we have written f_x in the convolutions to indicate the product $f_x = i\alpha n f_n$. Once again, the convolution $f * g$ for mode n is defined as $f * g = \sum_{q=-\infty}^{+\infty} f_{n-q} g_q$. In addition the hats have been dropped.

We use the continuity equation (4.9) to eliminate w_n from the equations (4.7), (4.8) and (4.10), leaving fourth-order and second-order equations for u_n, v_n. The fourth-order equation may be regarded as a finite amplitude Orr-Sommerfeld equation (where the basic flow is now the previously computed 2D secondary flows). To solve the set of ODEs and boundary conditions in (4.7)-(4.10) we apply the technique of spectral collocation and write $u_n(y) = \sum_{k=0}^{K} a_{nk} T_k(y)$ (with a similar representation for $v_n(y)$), where $T_k(y)$ is the kth Chebyshev polynomial. Evaluating the resulting equations at the maxima of the Kth Chebyshev polynomial yields a (discrete) generalized eigenvalue problem of the form $\mathbf{G}\mathbf{a} = \sigma \mathbf{B}\mathbf{a}$ for the complex eigenvalue σ and the associated eigenvector $\mathbf{a}$. This was solved using standard numerical methods.

4.3 Numerical results and discussion

We have solved the full stability problem, without assuming any symmetries, for a range of points on the 2D secondary flow solution surface. The 2D flows were computed with $N = 1$ Fourier modes and $K = 50$ Chebyshev modes. The stability problem was then solved with $N = 1$ and $K = 32$ and $K = 50$. It was found that $K = 32$ was adequate to resolve the stability eigenfunction. In Table 4.1 we demonstrate the agreement of our computed eigenvalues with those computed by Herbert (1983c) at an arbitrary point.

As mentioned in §1.7, it is of interest to compute the threshold amplitude of the 2D secondary flows, and the dependence of this threshold on the 2D parameters $\mathbf{Re_Q}, \alpha$ and the 3D spanwise wavenumber β. To do this we examine the low amplitude stability behavior. In Figure 4.1 we have plotted the most unstable eigenvalue for $\alpha = 1$ and $A_E < 0.05$ (where A_E is defined in (2.17)).

At $A_E = 0$ the 3D disturbances (plotted for different spanwise wavenumbers, β) are all stable (with $R\sigma \approx -1.3 \times 10^{-3}$) while the 2D disturbance is unstable ($R\sigma \approx 2 \times 10^{-3}$). As the 2D wave amplitude is increased, the 2D instability remains approximately constant, but the 3D growth rates increase linearly with amplitude.

TABLE 4.1. Comparison of computed superharmonic eigenvalues with Herbert (1983c)

Eigenvalue	Herbert (1983c)	Present
σ_s	0.0487	0.0489
	$0.0211 \pm i0.1050$	$0.0210 \pm i0.1050$
σ_a	0.0462	0.0462
	$0.0172 \pm i0.1053$	$0.0172 \pm i0.1053$

Superharmonic stability computed at $\mathbf{Re_P} = 5000, \mathbf{Re_Q} = 4954.29, \alpha = 1.12, \beta = 2, A = 5.848 \times 10^{-3}$ with $N = 1, K = 32$. σ_s, σ_a are for symmetric and antisymmetric modes respectively. Eigenvalues of present work have been scaled to U_P nondimensionalization of Herbert.

The threshold amplitude (the point where $\max R\sigma > 0$) is $A_E \approx 0.007$ for $\beta \approx 1$. However note the broadband behavior in β means that all 3D disturbances with $0.5 < \beta < 3$ have about the same growth rates near this point.

Turning now to Figure 4.2, we show the comparable low amplitude behavior for $\alpha = 1.1$ superharmonic disturbances. We note that the maximum α on the Orr-Sommerfeld neutral curve is $\alpha_{\mathrm{cr}} \approx 1.097$ and that 2D secondary flows computed for $\alpha > \alpha_{\mathrm{cr}}$ do not bifurcate from the Orr-Sommerfeld curve at $A_E = 0$. Thus for $\alpha = 1.1$, true equilibrium flows exist only down to an amplitude of about $A_E = 0.0035$. In this case all disturbances become unstable at about $0.004 < A_E < 0.005$ and grow linearly with amplitude. As is confirmed by examining the similar low amplitude plots for $\alpha = 1.15, 1.25, 1.3$, the growth rate $R\sigma$ at given A_E increases with α, suggesting that the threshold amplitude is lowest at higher α. This effect is counter-balanced by the increase in the minimum amplitude for existence of a 2D secondary flow. Hence, in considering superharmonic stability of true 2D equilibrium solutions, the threshold amplitude is about $A_E = 0.004$ for $0.5 < \beta < 3$ at $\alpha = 1.1$.

For larger α, the minimum 2D flow amplitude is greater than the threshold

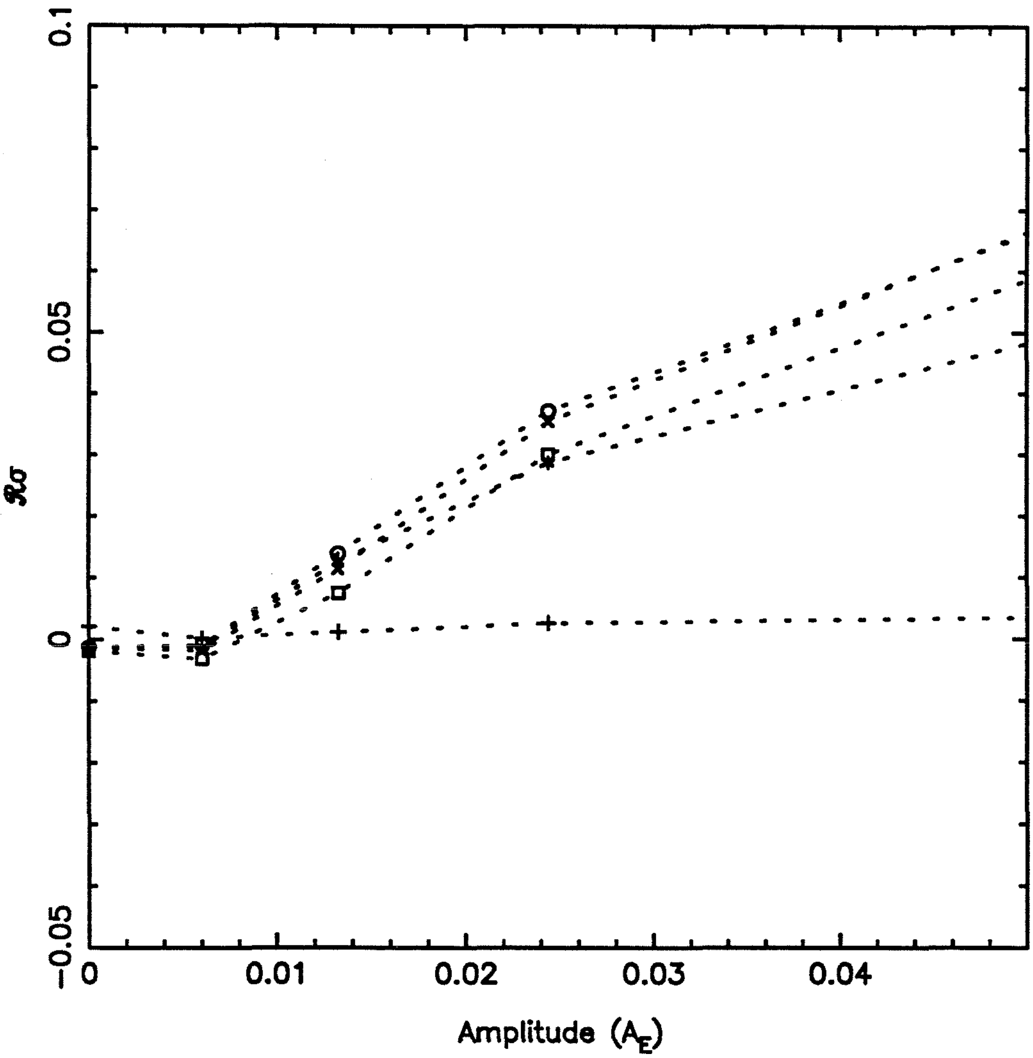

FIGURE 4.1. Growth rate of principal eigenvalue at $\alpha = 1.0$ ($N = 1, K = 32, 50$).

Most unstable eigenvalue of the superharmonic stability problem for 2D (+) and 3D disturbances $\beta = 0.5$ ($*$), 1.0 (○), 2.0 (×), 3.0 (□) vs. the amplitude of the 2D secondary flow, for low amplitude.

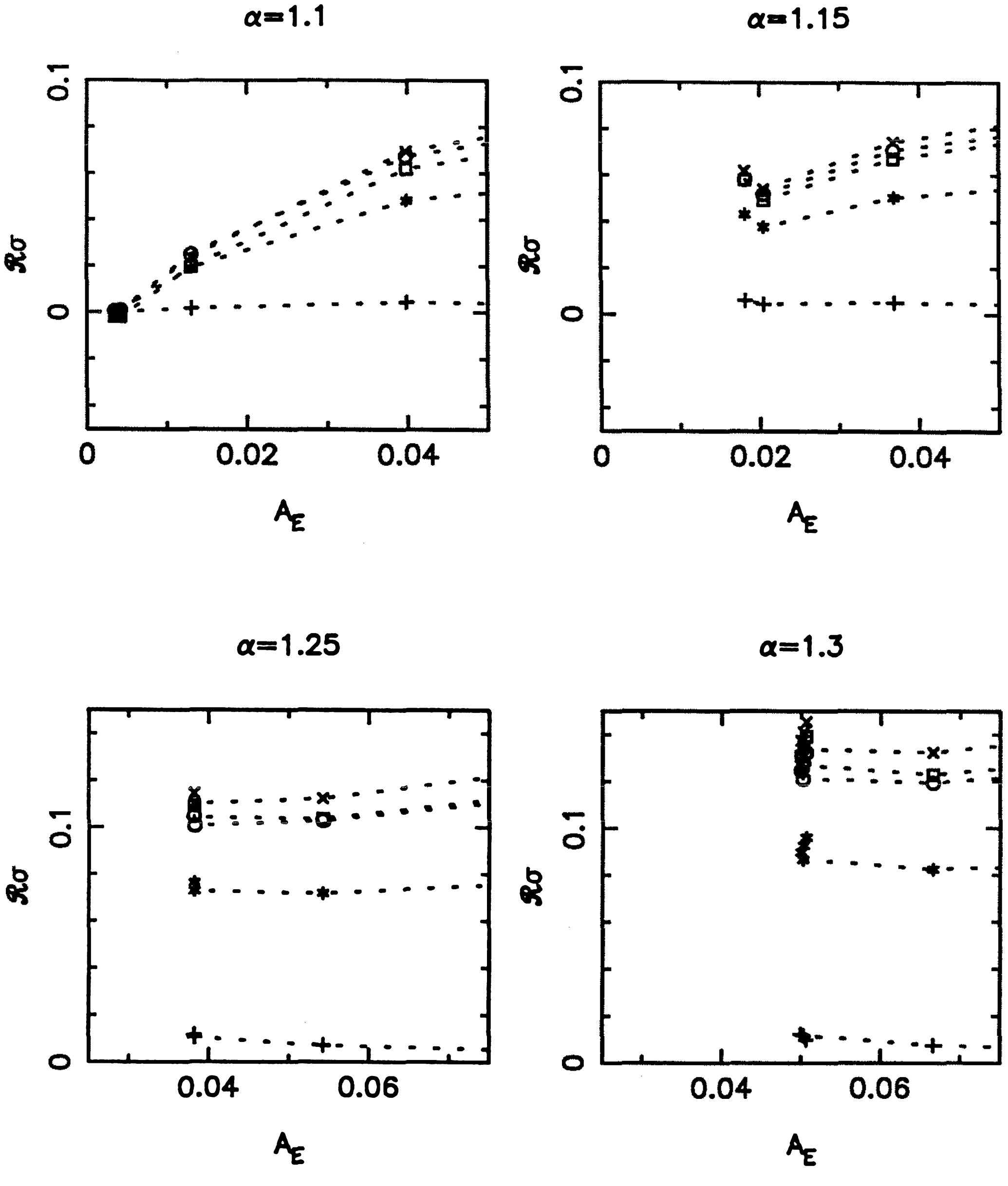

FIGURE 4.2. Growth rates for $\alpha = 1.1, 1.15, 1.25, 1.3$ ($N = 1, K = 32, 50$).

Most unstable eigenvalue of the superharmonic stability problem for 2D (+) and 3D disturbances $\beta = 0.5$ ($*$), 1.0 (o), 2.0 ($\times$), 3.0 (□) vs. the amplitude of the 2D secondary flow, for low amplitude.

amplitude, so 3D disturbances are always most unstable. At higher amplitudes on both these figures, there is a peaking in the $R\sigma$ vs. β dependence.

The behavior at minimum amplitude, visible especially in Figure 4.2 for $\alpha = 1.3$, shows the growth rate increasing quickly with small increases in amplitude. This is because as the Reynolds number increases on the lower branch, the amplitude changes slowly, so in fact the growth rate $R\sigma$ increases slowly with **Re**.

Turning now to the high amplitude behavior, in Figures 4.3-4.5 we have plotted the growth rate ($R\sigma$) of the most unstable eigenmode for streamwise wavenumbers $1 < \alpha < 1.4$. Without exception, in the parameter range considered, the most unstable eigenvalues are purely real, although a number of complex eigenvalues have comparable growth rates.

To demonstrate that $N = 1$ is sufficient x-resolution, in Figure 4.6 we plot the most unstable eigenvalue for the same conditions as Figure 4.3 (e.g., $\alpha = 1$) computed with $N = 2, K = 50$ for the secondary flow and $N = 2, K = 32$ for the stability problem. Apart from a slight shift to higher growth rates and a narrowing of the peak in σ, there is no significant change. The highest 2D amplitude plotted in Figure 4.6 ($A_E \approx 0.3$) corresponds to a point on the upper "branch" of the 2D secondary flow at $\mathbf{Re_Q} = 7598, \mathbf{Re_P} = 13741$.

As Figures 4.3-4.5 show, the increase in $R\sigma$ with 2D amplitude levels off to reach a maximum growth rate of about $R\sigma = 0.1 - 0.2$ for $\beta = 2$. There is a general shift towards higher growth rates at larger α. Orszag and Patera (1983) examined the energetics of some of their direct simulations and concluded that the secondary flow mediates the transfer of energy from the basic flow to the 3D disturbance. Our results support that conclusion since the growth rate does not continue to grow with the amplitude of the 2D secondary flow, as might be expected if energy transfer occurred directly from the 2D secondary flow.

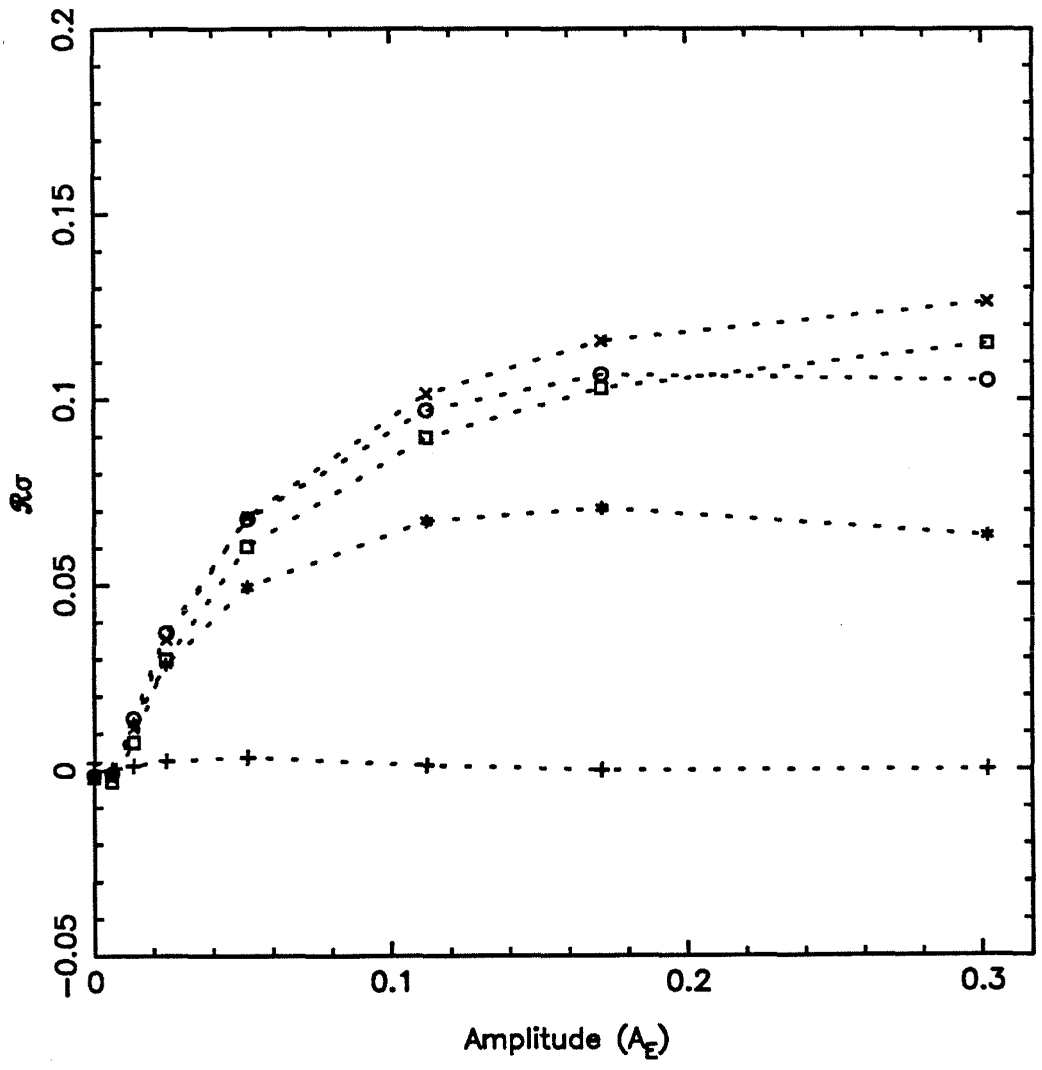

FIGURE 4.3. Growth rate of principal eigenvalue at $\alpha = 1.0$ ($N = 1, K = 32, 50$)

Most unstable eigenvalue of the superharmonic stability problem for 2D (+) and 3D disturbances $\beta = 0.5$ (∗), 1.0 (o), 2.0 (×), 3.0 (□) vs. the amplitude of the 2D secondary flow.

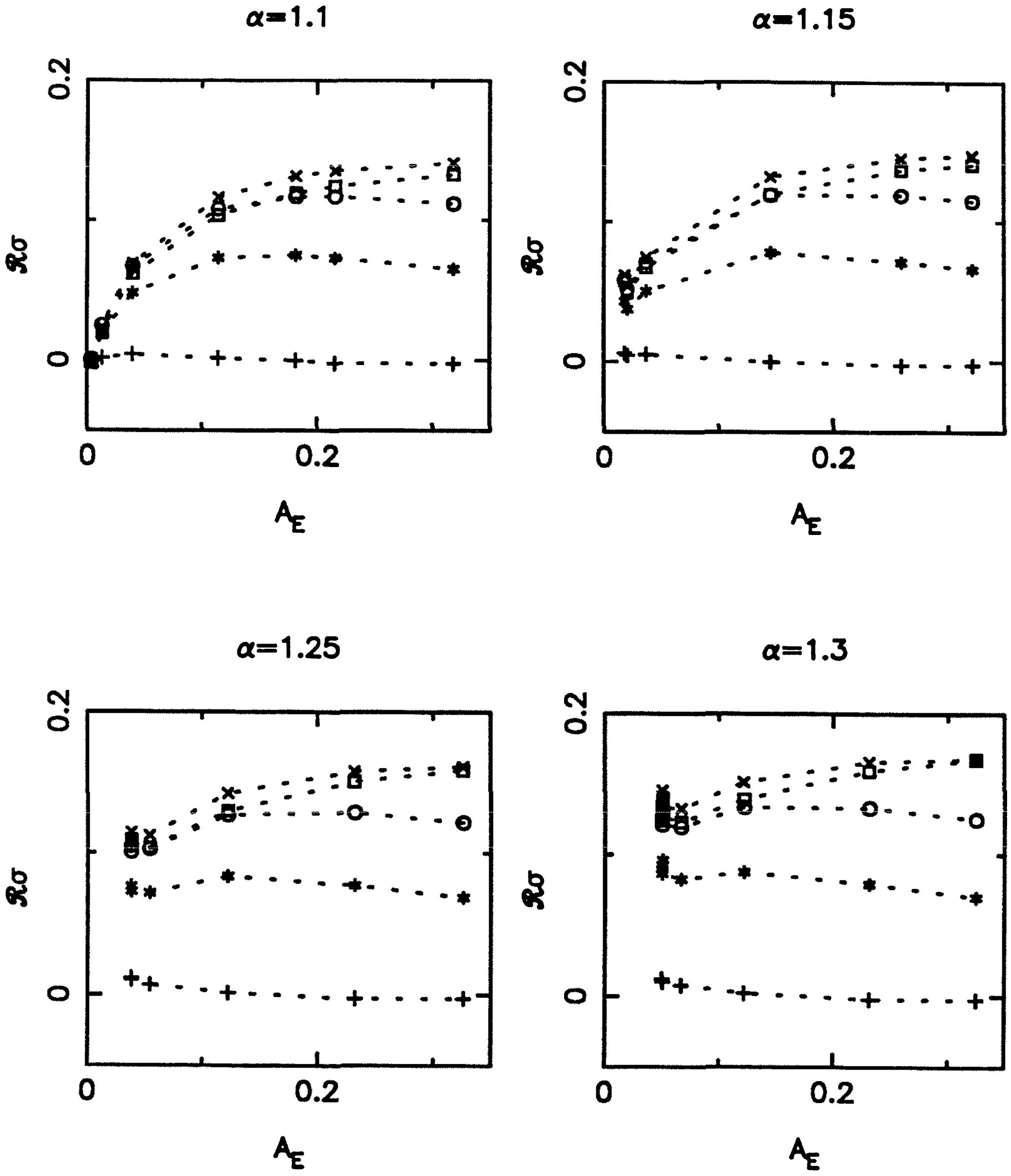

FIGURE 4.4. Growth rates for $\alpha = 1.1, 1.15, 1.25, 1.3$ ($N = 1, K = 32, 50$).

Most unstable eigenvalue of the superharmonic stability problem for 2D (+) and 3D disturbances $\beta = 0.5$ ($*$), 1.0 (o), 2.0 ($\times$), 3.0 ($\Box$) vs. the amplitude of the 2D secondary flow.

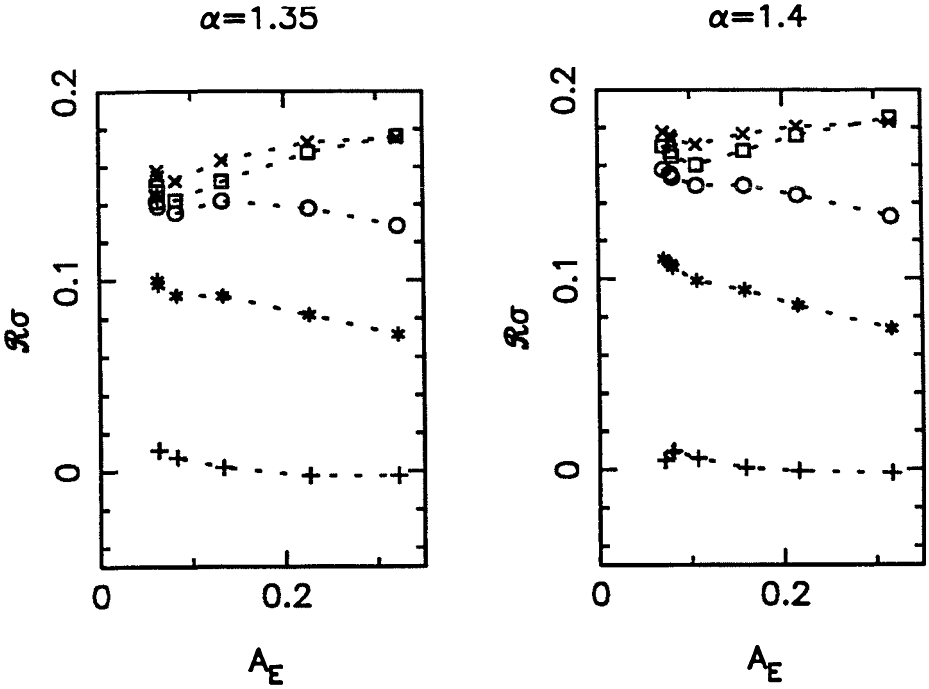

FIGURE 4.5. Growth rates for $\alpha = 1.35, 1.4$ ($N = 1, K = 32, 50$).

Most unstable eigenvalue of the superharmonic stability problem for 2D (+) and 3D disturbances $\beta = 0.5$ ($*$), 1.0 (o), 2.0 ($\times$), 3.0 (□) vs. the amplitude of the 2D secondary flow

The dependence on spanwise wavenumber (β) is more clearly shown in Figure 4.7 at $\alpha = 1$, for various different amplitudes of the 2D secondary flow. In this case, the eigenvalues for symmetric and antisymmetric disturbances, which are also the most unstable, are plotted. These disturbances are of the form:

$$u_n(-y) = (-1)^{n+1} u_n(y) \quad \text{(antisymmetric)} \qquad (4.11a)$$

$$u_n(-y) = (-1)^n u_n(y) \quad \text{(symmetric)} \qquad (4.11b)$$

The broad-band dependence on β is clear, particularly at high amplitude. In general, $\beta \approx 2$ is the most unstable wavenumber, but significant growth rates are observed for $1 < \beta < 3$.

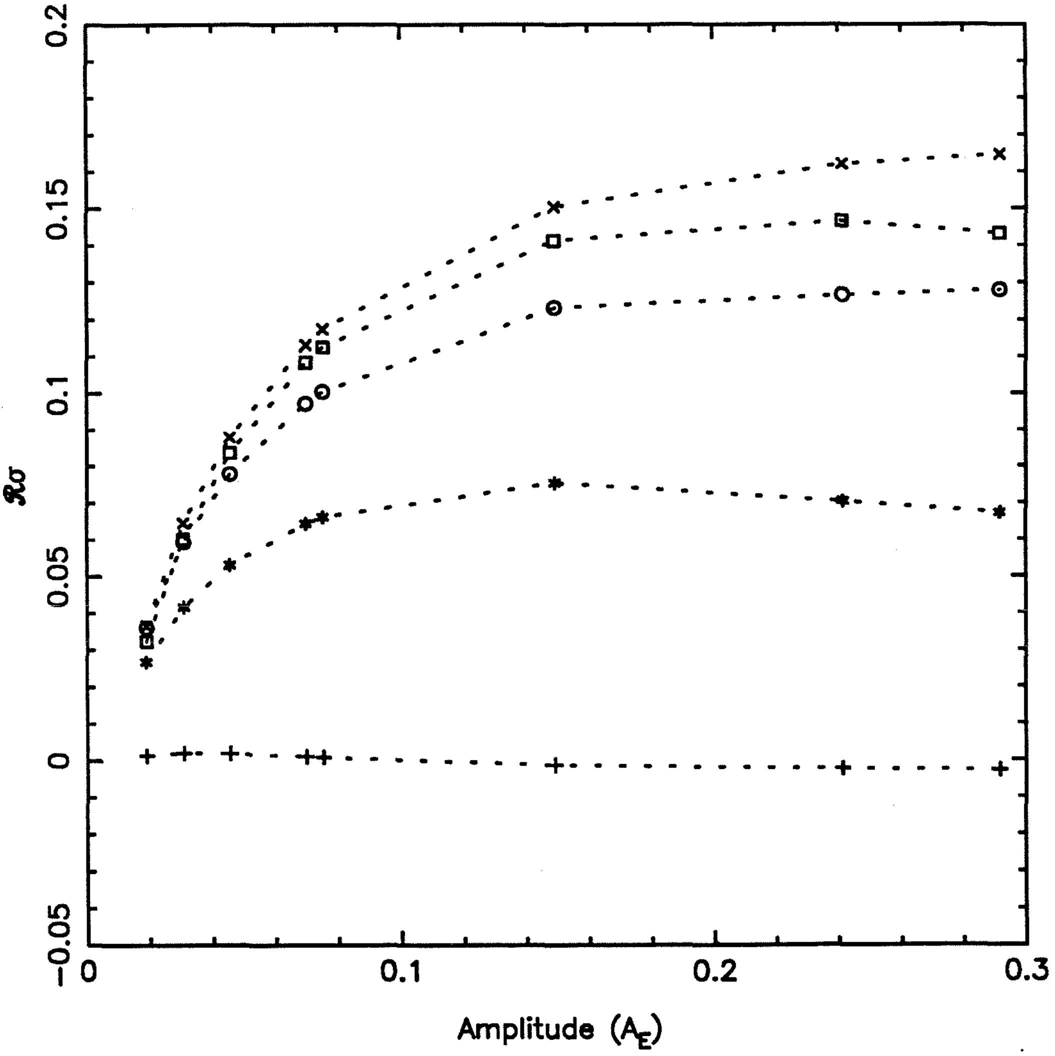

FIGURE 4.6. Growth rate of principal eigenvalue at $\alpha = 1$ ($N = 2, K = 32, 50$).

Most unstable eigenvalue of the superharmonic stability problem for 2D (+) and 3D disturbances $\beta = 0.5$ ($*$), 1.0 ($\circ$), 2.0 ($\times$), 3.0 ($\square$) vs. the amplitude of the 2D secondary flow.

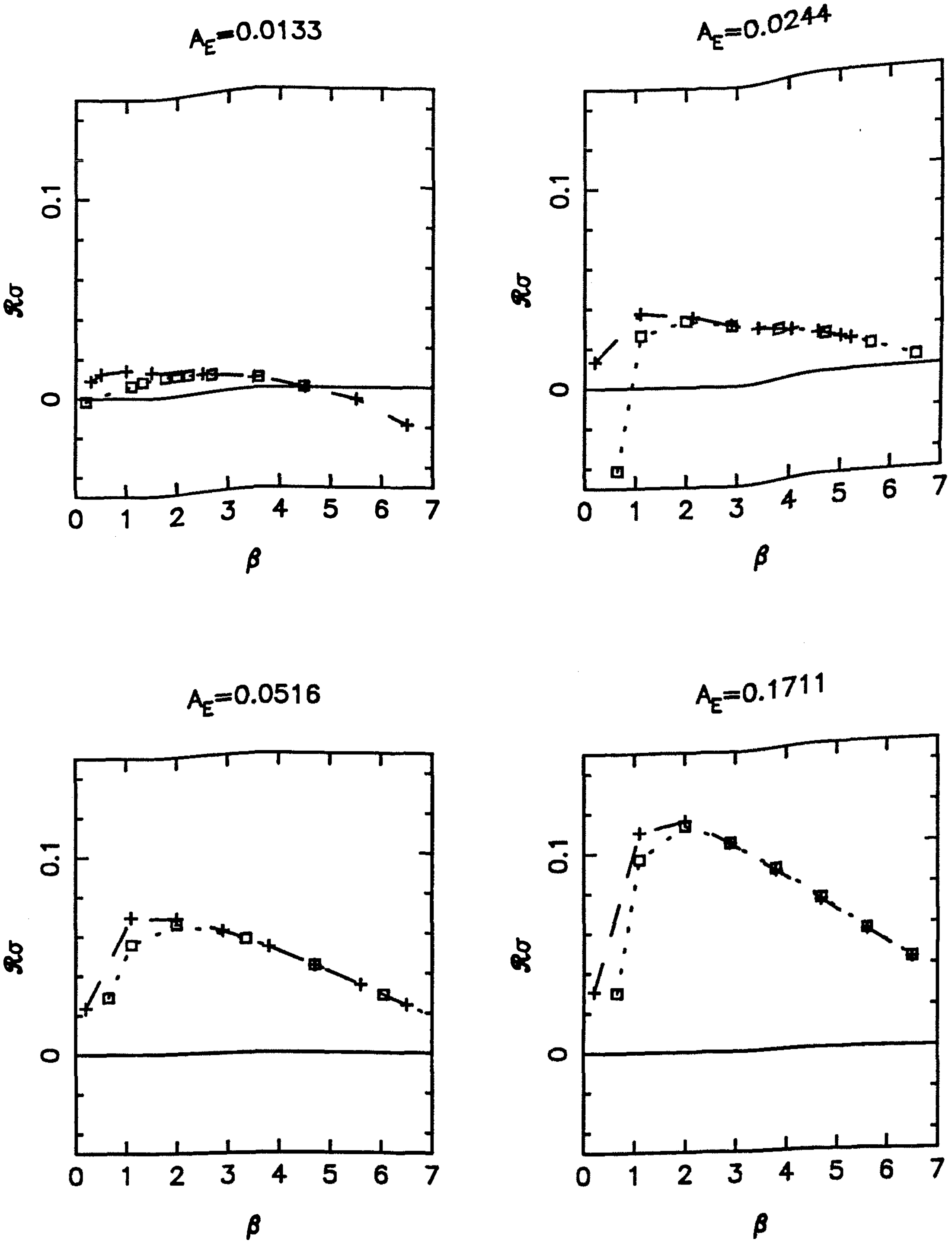

FIGURE 4.7. Dependence of instability growth rate ($R\sigma$) on spanwise wavenumber β, at $\alpha = 1$. Principal eigenvalues for both symmetric (+) and antisymmetric (□) disturbances are plotted at various 2D secondary flow amplitudes.

4.4 Instability mechanism for 2D secondary flows

Although we include this discussion here, to allow convenient comparison with superharmonic stability results, the conclusions are applicable to subharmonic stability also since the mechanism being considered is local and independent of the computational domain outside a small region of the flow (the ellipse mentioned below).

Pierrehumbert (1986) numerically found a short-wave, scale-independent instability of the Euler equations applied to a locally elliptical flow. He proposed that this mechanism is responsible for the 3D instability of shear flows containing 2D coherent structures. Landman and Saffman (1987) have used the work of Bayly (1986) and Craik and Criminale (1986) to compute the Floquet problem for a locally elliptical flow, including the effects of viscosity. They found that the inviscid instability mechanism persists when viscosity is introduced, leading to a stability boundary in Ekman number (a measure of the ratio of viscous dissipation to vorticity in the basic flow) versus a streamline eccentricity parameter (reproduced in Figure 4.8). Thus, if this mechanism is operative, we would expect convective, rather than viscous growth rates with a short wavelength cutoff caused by the action of viscosity.

In Figure 4.9 we have plotted the streamlines of the flow in the moving reference frame at the amplitudes of Figure 4.7, and in Figure 4.10 the corresponding vorticity contours. Although at high amplitudes the closed streamline region is more pear-shaped than elliptical, there is a significant region where the assumption of elliptical flow is reasonable, with constant contained vorticity. We note the increase in streamline eccentricity with decreasing 2D amplitude.

As Landman and Saffman (1987) pointed out, their results can be used as a linear stability theory and thus compared with our exact linear stability calculations. The

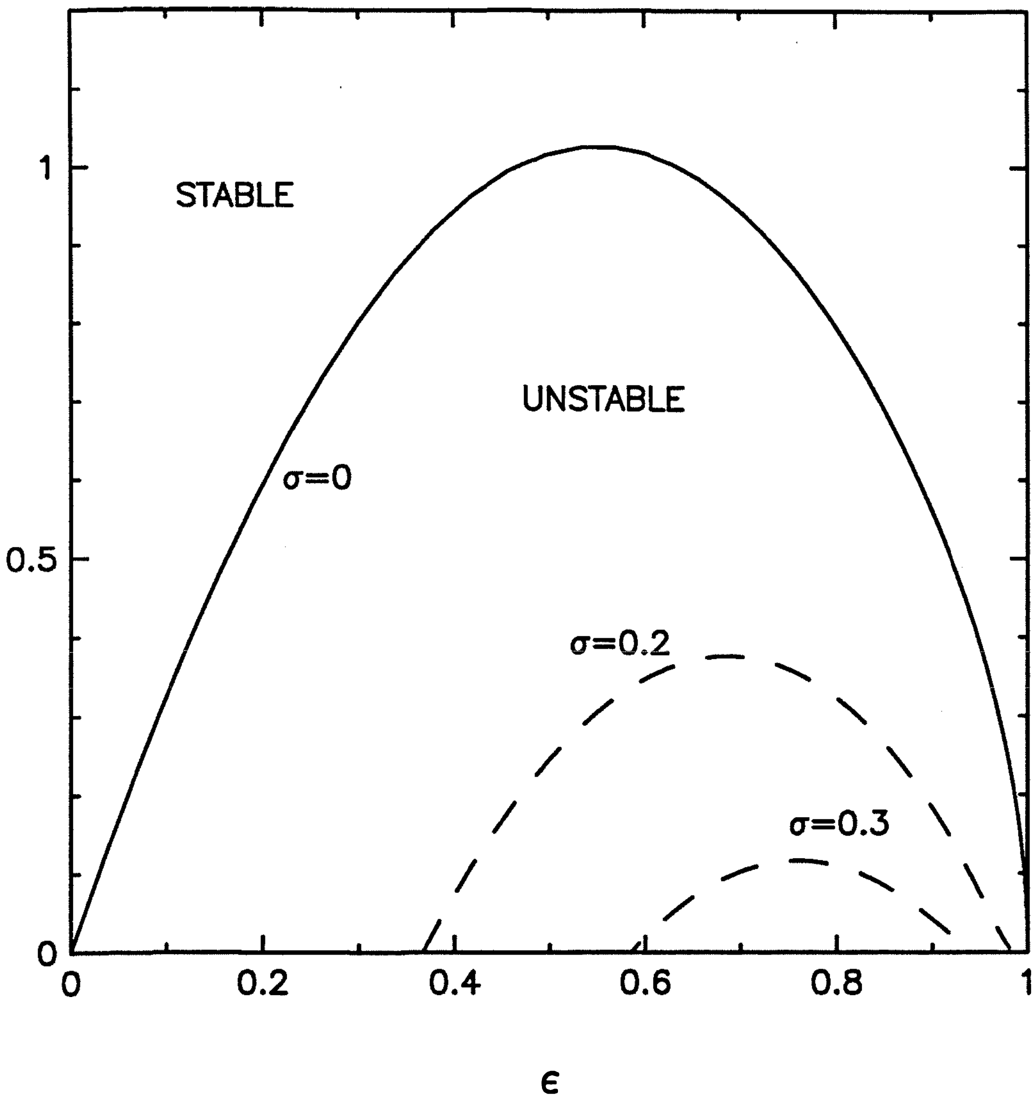

FIGURE 4.8. Stability boundary in the ϵ (streamline eccentricity parameter) – Ekman number plane. From Landman and Saffman (1987).

Here $\epsilon = ((a/b)^2 - 1)/((a/b)^2 + 1)$, with a, b the major and minor axes of the ellipse, and $E_\gamma = 2\pi k_x^2/(\gamma \mathrm{Re})$. Note that they used β to denote the streamline eccentricity parameter, and the growth rates shown should be halved to compare with our results (because of a different parametrization). 2γ is the (constant) vorticity in the elliptical region and k_x the wave-number of the instability.

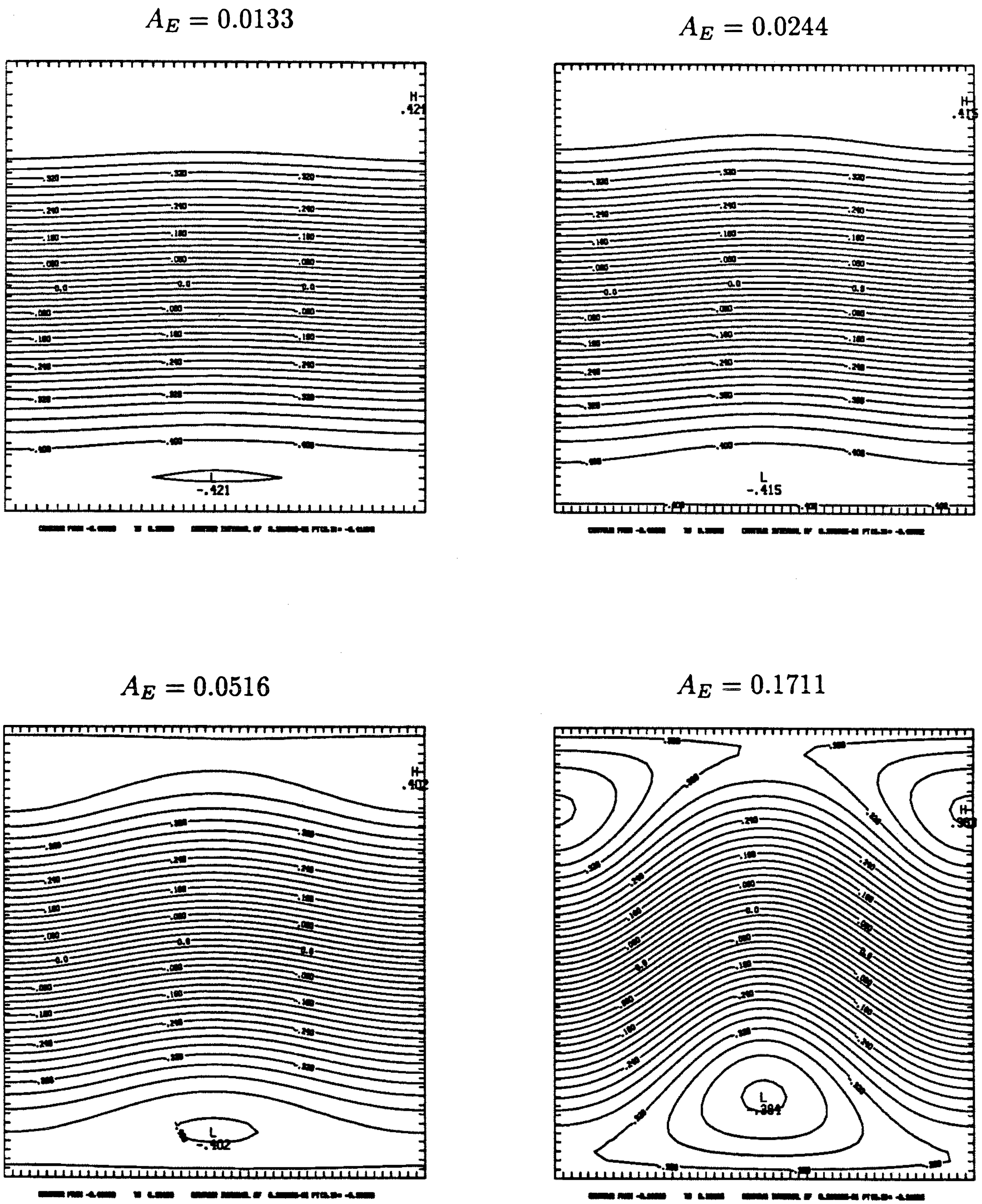

$A_E = 0.0133$

$A_E = 0.0244$

$A_E = 0.0516$

$A_E = 0.1711$

FIGURE 4.9. Streamlines of the 2D secondary flows of Figure 4.7. Note that the x and y axes are not to scale: the length of the x-domain is 2π and of the y-domain 2, in units scaled by h, the channel half-width.

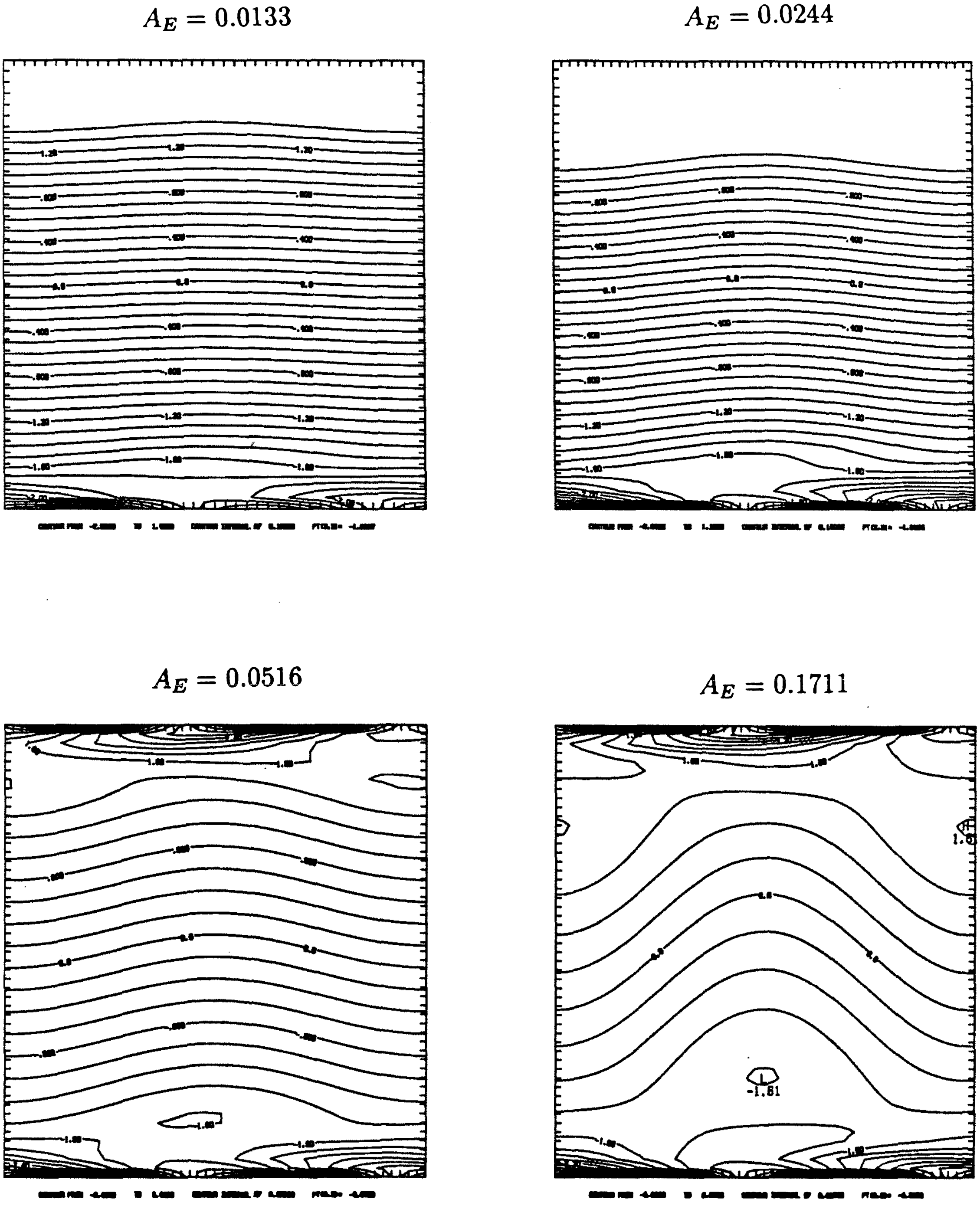

$A_E = 0.0133$

$A_E = 0.0244$

$A_E = 0.0516$

$A_E = 0.1711$

FIGURE 4.10. Vorticity contours of the 2D secondary flows of Figure 4.7. Note that the x and y axes are not to scale: the length of the x-domain is 2π and of the y-domain 2, in units scaled by h, the channel half-width.

qualitative agreement is clear; at large spanwise wavenumber β (where the elliptical model predicts that $\beta \propto k_x$, the wavenumber of the instability), there is a cutoff due to viscosity. As β decreases, the Ekman number (E_γ) decreases and σ increases up to a maximum, σ_{max}, where the minimum wavelength of the elliptical instability exceeds the dimension of the ellipse and the mechanism will no longer operate. This implies a sharp cutoff for $\beta < \beta_{\sigma_{\max}}$, as is observed in Figure 4.7. The behavior for $\beta < \beta_{\sigma_{\max}}$ is not predicted by the theory, but the observed sharp drop in growth rate suggests that the elliptical instability is the dominant mechanism in the flow. Furthermore, as the 2D flow amplitude (A_E) decreases and the ellipse eccentricity $\epsilon \rightarrow 1$, the model predicts a decrease in both $\beta_{\sigma=0}$ and σ_{max} in agreement with the actual behavior.

Landman and Saffman (1987) computed the asymptotic growth rate in the inviscid limit, assuming the form of the flow remained essentially unchanged and found reasonable agreement with the numerical results of Orszag and Patera (1983).

At the small wavelength limit of the instability (large wavenumber), the quantitative agreement between the elliptical model and our numerical results is good. This is an important test because it requires no assumption about the size of the relevant elliptical region. The long wavelength cutoff presumably depends on where the assumption of local ellipticity breaks down and is much more subjective; we thus compare σ_{max} at the observed $\beta_{\sigma_{max}}$. For $\alpha = 1$, $A_E = 0.1711$, we find $\beta_{\sigma=0} \approx 10, \beta_{\sigma_{max}} = 2$ and $\sigma_{\max} = 0.12$ from Figure 4.7 which is in good agreement with $\beta_{\sigma=0} = 12$ and $\sigma_{max} = 0.12$ (at $\beta = 2$), computed from the model following Landman and Saffman's procedure. At an amplitude of $A_E = 0.0516$, we find (with actual values in parentheses): $\beta_{\sigma=0} = 8.1(8.9)$ and $\sigma_{max} = 0.08(0.07)$ at $\beta \approx 2$. Below this amplitude the high eccentricity of the closed streamline region makes accurate computation of ϵ and E_γ difficult. The long wavelength cutoff is at $l_{max} \approx 4.4$ in x (for both cases) which is well outside the elliptical region shown in Figure 4.9, indicative of the robustness of the elliptical instability theory, as Pierrehumbert originally hypothesized.

In Figure 4.11, we plot the perturbation z-vorticity (i.e., of the 3D stability eigensolution) for the various spanwise wavenumbers shown for $A_E = 0.1711, \alpha = 1$ in Figure 4.7. The vorticity is plotted on the half-domain $-1 < y < 0$ and is for the symmetric solution. Vorticity contours for the anti-symmetric solution are similar. Because of the indeterminacy in the eigensolution to the extent of an arbitrary constant, neither the absolute magnitude nor the sign of the vorticity can be determined. However, using the zero vorticity contour as a delineator, we note that for $\beta > 2$ the instability is confined to the elliptical region discussed above and shown in Figure 4.9 for this amplitude, and agrees well with the vorticity contours shown by Pierrehumbert for high strain rate (corresponding to the high ellipse eccentricity observed in all the 2D secondary flows) in Figure 2 of his paper. Furthermore, the instability appears to be confined within an $O(\beta^{-1})$ of the vortex center, as was noted by Orszag and Patera (1983) and in agreement with Pierrehumbert's results.

As noted above, there is a long wavelength cutoff to the theory's applicability when the instability wavelength is larger than the vortex itself and the assumption of local ellipticity breaks down. As the plots for $\beta = 0.2, 1.1$ in Figure 4.11 show, the instability does indeed "break out" of the vortex region, corresponding to the drop-off in instability growth rate shown in Figure 4.7 at low β.

As was noted above, there is a general trend of growth in the instability growth rate $R\sigma$ with increasing α at fixed 2D secondary flow amplitude A_E. As we show below, the elliptical instability model predicts this behavior also. In Figure 4.12 we show the streamlines for three different streamwise wavenumbers ($\alpha = 1, 1.15, 1.3$) at the same amplitude ($A_E \approx 0.32$), with the vorticity contours in Figure 4.13.

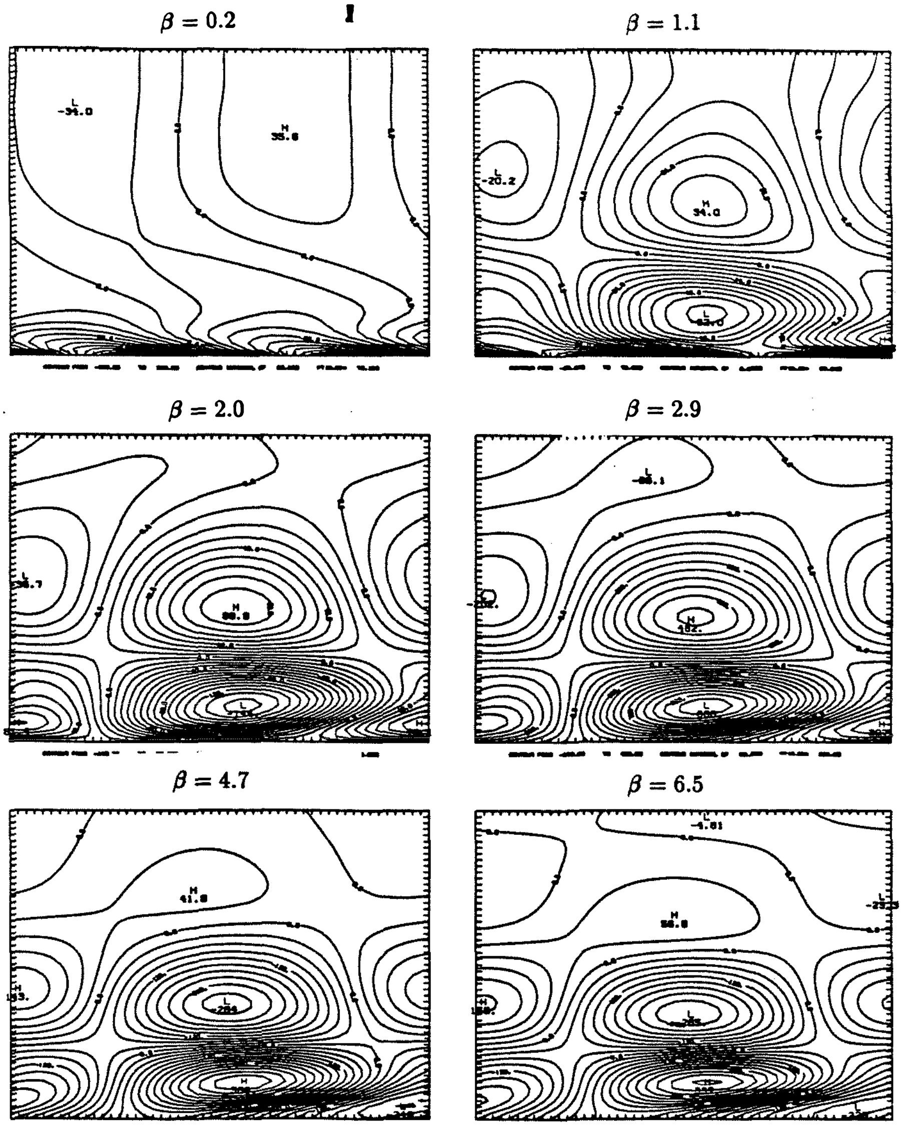

$\beta = 0.2$

$\beta = 1.1$

$\beta = 2.0$

$\beta = 2.9$

$\beta = 4.7$

$\beta = 6.5$

FIGURE 4.11. Perturbation z-vorticity contours (of the 3D stability eigensolution) for $A_E = 0.1711, \alpha = 1$. The domain of each sub-plot is $0 < x < 2\pi$, $-1 < y < 0$. Contours shown for the β values plotted in Figure 4.7.

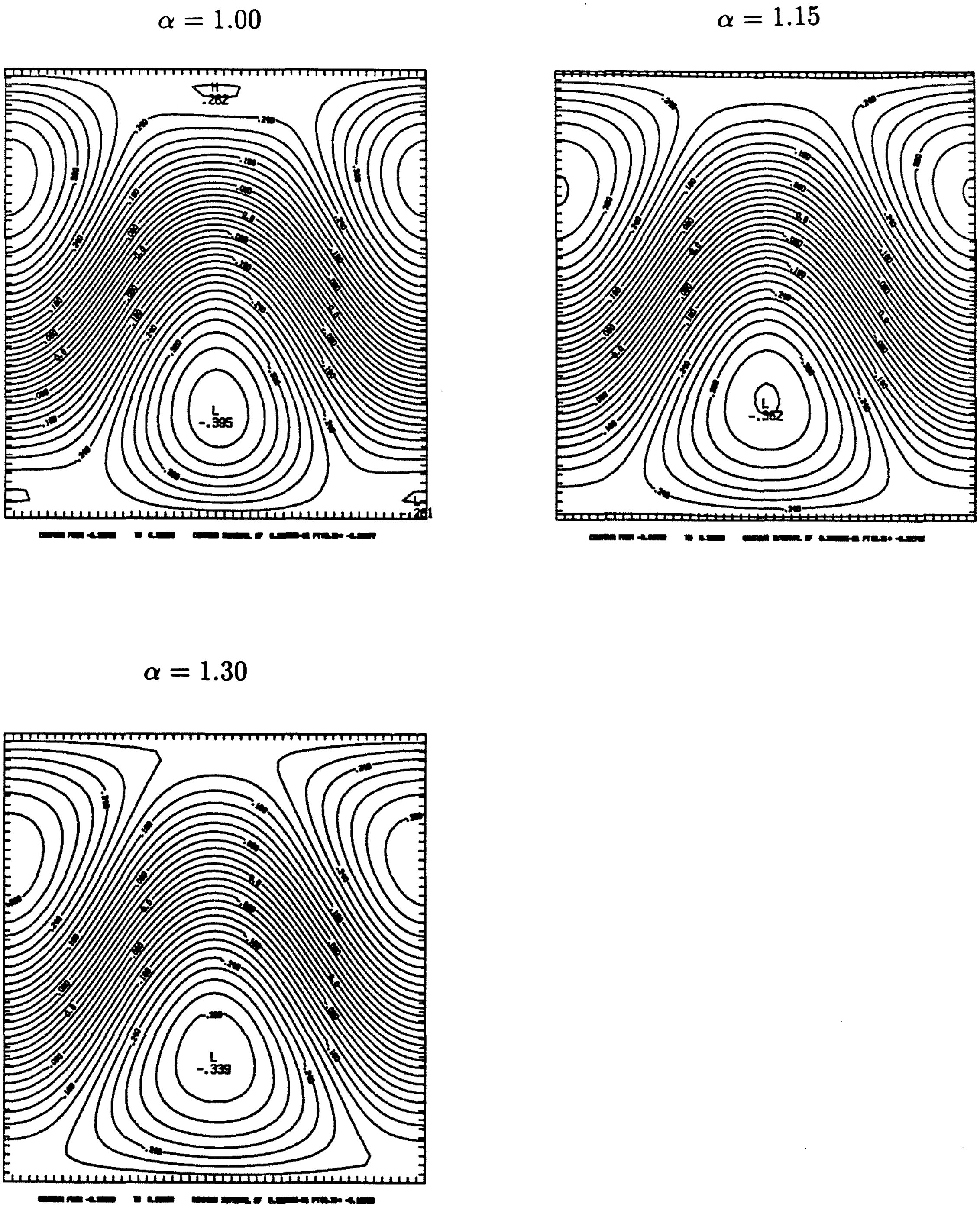

$\alpha = 1.00$

$\alpha = 1.15$

$\alpha = 1.30$

FIGURE 4.12. Streamlines of 2D secondary flows for different α.

Flows computed with $N = 2, K = 50$ at $A_E \approx 0.32$, and $\alpha = 1, 1.15$ and 1.3. The domains of each sub-plot are $0 < x < 2\pi/\alpha$ and $-1 < y < +1$.

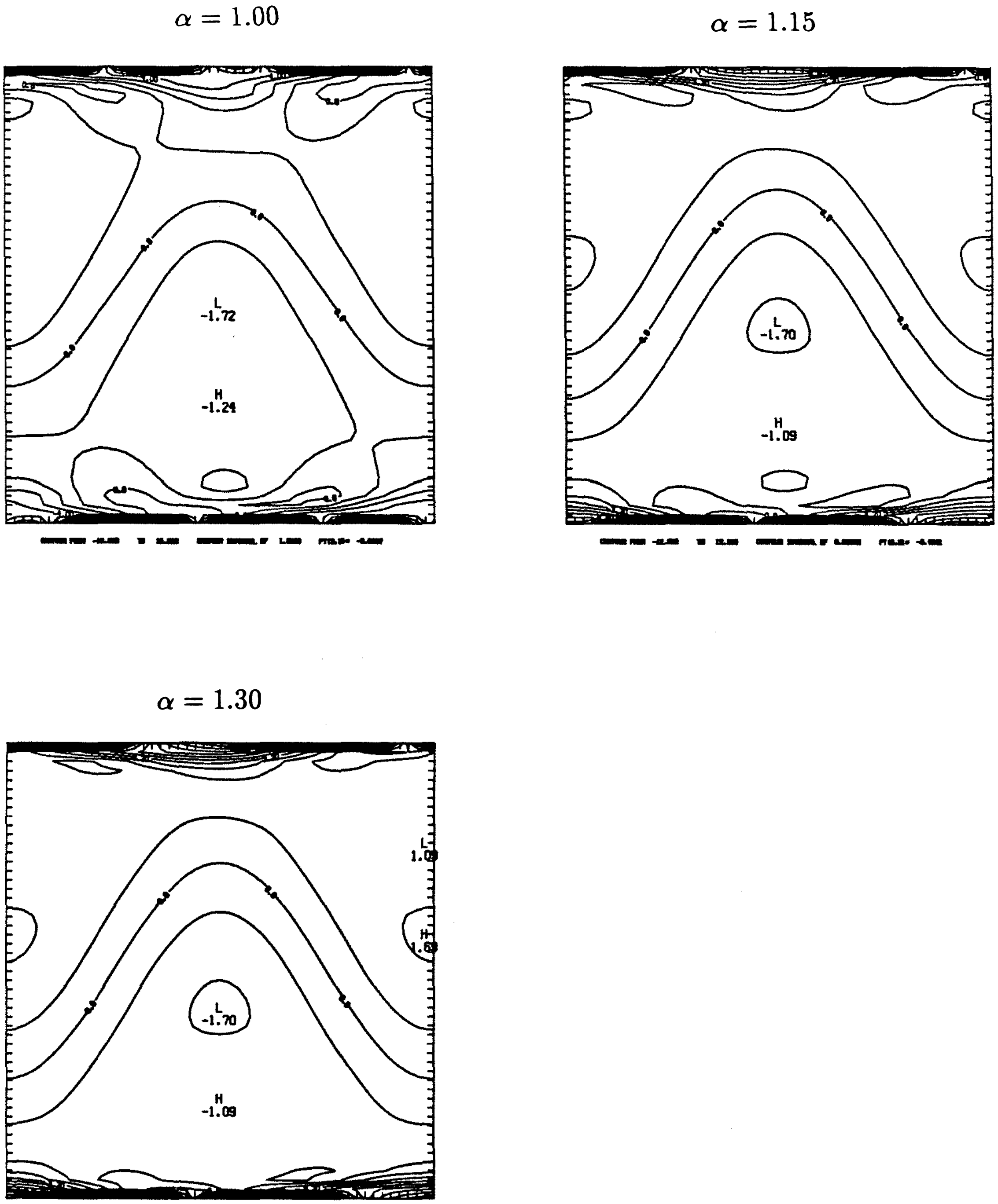

FIGURE 4.13. Vorticity contours of 2D secondary flows in Figure 4.11. Flows computed with $N = 2, K = 50$ at $A_E \approx 0.32$, and $\alpha = 1, 1.15$ and 1.3. The domains of each sub-plot are $0 < x < 2\pi/\alpha$ and $-1 < y < +1$.

Because of the high amplitude it was necessary to compute both the 2D secondary flows and the stability with $N = 2$. The similarity of the three flows is clear. Although the unscaled ellipticity of the closed streamline region is the same in each, the x-scale (being $2\pi/\alpha$) means that the ellipse eccentricity a/b and the eccentricity parameter $\epsilon = ((a/b)^2 - 1)/((a/b)^2 + 1)$ decrease with increasing α. From Figure 4.8, this implies a shift towards higher growth rates (provided $\epsilon > 0.8$ and E_γ is small). In Table 4.2, we list the growth rates computed using the elliptical instability model (σ in the table) and the actual values (σ_{obs}) at a reference spanwise wavenumber of $\beta = 2$ (at which point we take $k_x \approx 2.8$). At this long wavelength, we took as our "elliptical" approximation the largest smooth closed streamline; with such a subjective choice the comparison should be viewed as qualitative only. As Table 4.2 shows, the trend in α is approximately correct and the predicted growth rates are reasonably close to those computed using Floquet theory.

TABLE 4.2. Comparison of actual instability growth rates with those predicted by elliptical model, showing change with increasing α at similar amplitudes.

α	A_E	$\mathbf{Re_Q}$	a/b	ϵ	γ	E_γ	σ	σ_{obs}
1.00	0.33	10280	3.34	0.84	0.7	0.007	0.172	0.169
1.15	0.32	6230	3.29	0.83	0.6	0.013	0.171	0.163
1.30	0.32	5065	2.91	0.79	0.6	0.016	0.176	0.164

In summary, the elliptical instability proposed by Pierrehumbert, as modified for viscosity by Landman and Saffman, does give quantitative agreement with σ vs. β results computed with a full stability code. In addition, it qualitatively explains many of the stability features of the 2D secondary flows and indicates that only the *local* flow field is important for stability considerations.

4.5 3D bifurcations to 3D steady waves

We note that solutions to (4.7)-(4.10) occur in complex conjugate pairs. For if σ is an eigenvalue with associated eigenvector (u_n, v_n, w_n), then taking the complex conjugate of (4.7)-(4.10) shows that $\tilde{\sigma} = \sigma^*$ is also an eigenvalue with associated eigenvector $(\tilde{u}_n, \tilde{v}_n, \tilde{w}_n) = (u^*_{-n}, v^*_{-n}, -w^*_{-n})$. This also suggests looking for purely real eigenvalues ($I\sigma = 0$) with associated eigenvector $(u_n, v_n, w_n) = (u^*_{-n}, v^*_{-n}, -w^*_{-n})$. Such a 3D disturbance is phase-locked with the 2D steady wave. As noted above, the most unstable eigenvalues are generally of this form. When looking for bifurcations from the 2D secondary flows into 3D secondary flows (steady waves), we are interested in $\sigma = 0$ stability solutions (neutrally stable, phase-locked solutions) and so can restrict ourselves to the purely real eigenvalue stability problem for each 2D secondary flow $(\mathbf{Re}_{\mathbf{Q}}, \alpha)$, and then search for a β such that $I\sigma = 0$.

As is suggested by Figure 4.7, zeroes in σ exist for both antisymmetric and symmetric solutions. By adding appropriate amplitude and phase conditions to equations (4.7)-(4.10) we have solved for these zeroes using Euler-Newton continuation. Of course, other zeroes (from less unstable modes) are possible and to each zero there corresponds a different family of 3D steady waves which bifurcate off a point on the 2D solution surface at $(\mathbf{Re}_{\mathbf{Q}}, \alpha)$ with some β and can be continued into the 3D space $(\mathbf{Re}_{\mathbf{Q}}, \alpha, \beta)$. We have followed several of these families into 3D space and their behavior is described in detail in Chapter 5, 3D STEADY WAVES.

4.6 3D subharmonic stability: Problem formulation

Instead of seeking the superharmonic stability of 2D secondary flows in the form of (4.6), we can also examine 3D subharmonic instability. In the general subharmonic case, we look for a modal decomposition involving exponents of the form $i\alpha pnx$. If we look for period-doubling ($p = 1/2$), the disturbance can be written

$$\begin{aligned} \mathbf{u}_{3D}(x,y,z) &= e^{i\beta z} \sum_{n=-\infty}^{+\infty} \hat{\mathbf{u}}_n(y) e^{i\alpha \frac{n}{2} x} \\ &= e^{i\beta z} \sum_{n=-\infty}^{+\infty} \hat{\mathbf{u}}_n(y) e^{i\alpha n x} \qquad \text{(superharmonic)} \qquad (4.12) \\ &+ e^{i\beta z} \sum_{n=-\infty}^{+\infty} \hat{\mathbf{u}}_n(y) e^{i\alpha (n+\frac{1}{2}) x}. \qquad \text{(subharmonic)} \end{aligned}$$

Substituting into the 3D stability equations (4.3)-(4.5), we find that the superharmonic and subharmonic terms uncouple (because the basic flow $(U, V, 0)$ is purely superharmonic). Consequently, equations (4.7)-(4.10) hold with $n = \pm 1/2, \pm 3/2, \ldots$, where now the subharmonic disturbance is

$$\mathbf{u}_{3D}(x,y,z) = e^{i\beta z} \sum_{n=\pm\frac{1}{2},\pm\frac{3}{2},\ldots} \hat{\mathbf{u}}_n(y) e^{i\alpha n x}. \qquad (4.13)$$

The resulting equations were solved in an identical fashion to the superharmonic case.

4.7 Numerical results and discussion

In Table 4.3, we compare the most unstable subharmonic eigenvalues with those of Herbert (1983c) for the same conditions as those in Table 4.1.

TABLE 4.3. Comparison of computed subharmonic eigenvalues with Herbert (1983c).

Eigenvalue	Herbert (1983c)	Present
σ_{sub}	$0.0465 \pm i0.0020$	$0.0465 \pm i0.0020$
	$0.0209 \pm i0.1014$	$0.0209 \pm i0.1014$
	$0.0142 \pm i0.1044$	$0.0142 \pm i0.1044$

Subharmonic stability computed at $\mathbf{Re_P} = 5000, \mathbf{Re_Q} = 4954.29, \alpha = 1.12, \beta = 2, A = 5.848 \times 10^{-3}$ with $N = 1, K = 32$. Eigenvalues of present work have been scaled to U_P nondimensionalization of Herbert.

In Figure 4.14, we show the most unstable eigenvalue for various different spanwise and streamwise wavenumber (β, α) plotted at low secondary flow amplitude in the same way as the superharmonic stability plot, Figure 4.1. In the $\alpha = 1$ plot we find the threshold amplitude (where the 3D disturbances first become unstable for some β) is at $A_E \approx 0.004$ for $\beta = 1$. Note that unlike the superharmonic threshold amplitude at $\alpha = 1$ (plotted in Figure 4.3) there is much greater variation in threshold amplitude with β (i.e., the σ vs. β curve is much more peaked at this point).

For $\alpha = 1.1$, shown with $\alpha = 1.15$ and $\alpha = 1.3$ in Figure 4.15, the 3D disturbances are unstable for the minimum amplitude 2D secondary flow at $A_E \approx 0.0035$ (because $\alpha_{\text{cr}} < 1.1$ the secondary flow curve does not intersect $A_E = 0$). As for the superharmonic stability case there is an increase in the growth rate with increasing α at fixed amplitude, as well as an increase in the minimum 2D secondary flow amplitude. The balance of these effects means that the threshold amplitude for subharmonic disturbances occurs approximately at $\alpha = 1.1, A_E = 0.004$ for $0.5 < \beta < 3$. This is no different from the superharmonic threshold amplitude, suggesting that the "window" that Herbert (1983c) proposed between subharmonic

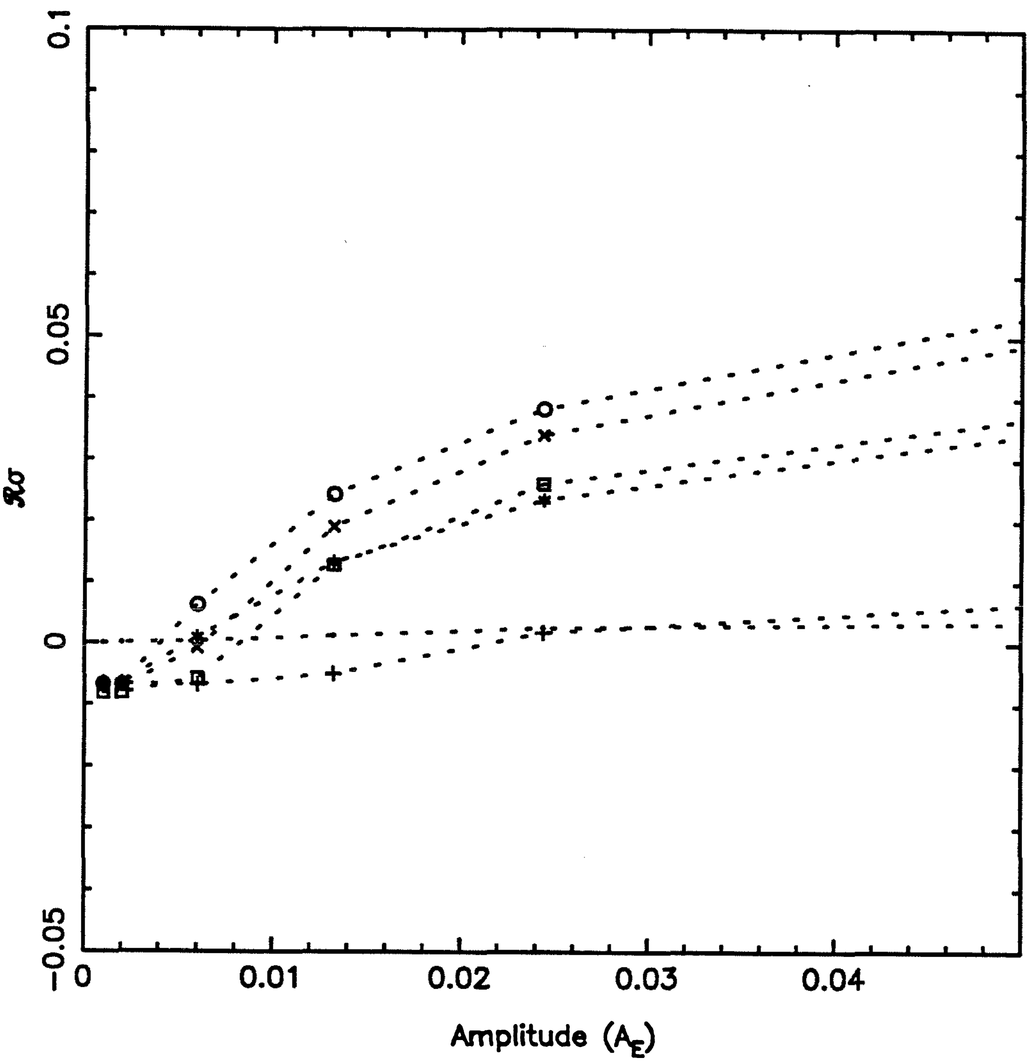

FIGURE 4.14. Growth rate of principal eigenvalue at $\alpha = 1.0$ $(N = 1, K = 32, 50)$.

Most unstable eigenvalue of the subharmonic stability problem for 2D (·) and 3D disturbances β =0.25 (+), 0.5 (×), 1.0 (o), 2.0 (×),3.0 (□) vs. the amplitude of the 2D secondary flow, for low amplitude.

and superharmonic threshold amplitudes may be small or non-existent for PPF. Nevertheless, at this low amplitude the subharmonic instability is stronger, suggesting that it is initially dominant. At slightly higher amplitudes, the growth rates are comparable, so that in this regime both subharmonic and superharmonic instability mechanisms are viable ones for breakdown of PPF.

At higher amplitudes ($A_E > 0.05$), we found that $N = 1$ was insufficient resolution (unlike the superharmonic stability calculations), so in Figures 4.16 and 4.17 we show the instability growth rate for $\alpha = 1$ and $\alpha = 1.1, 1.15$ and 1.3 respectively, computed with $N = 2, K = 50$ for the 2D secondary flows and $N = 2, K = 32, 40$ for the 3D subharmonic stability. The low amplitude data (which were computed with $N = 1$) are not included in these figures. As discussed in §4.3, the most unstable superharmonic instability is always one of the symmetric or antisymmetric eigenmodes, leading to the smooth envelopes shown in Figures 4.3. In the subharmonic stability problem, there are many unstable (generally complex) eigenvalues of similar magnitude, giving an envelope with the dips and peaks of Figures 4.16 and 4.17. Also there appears to be no drop-off in growth rate to a constant value as the 2D amplitude is increased as there is in the superharmonic stability case. The variation with β is much more pronounced than for superharmonic disturbances.

Consequently, although at intermediate amplitudes the superharmonic growth rates are greater than the subharmonic, there are indications that at high amplitudes ($A_E > 0.3$) this may not remain true.

4.8 Bifurcations to subharmonic waves

Unlike the 3D superharmonic stability case, there are no purely real eigenvalues $I\sigma = 0$ with symmetry. If one assumes that all eigensolutions satisfy y symmetry (as seems to be the case) then

$$u_n(-y) = (-1)^{n+\frac{1}{2}} u_n(+y) \tag{4.14a}$$

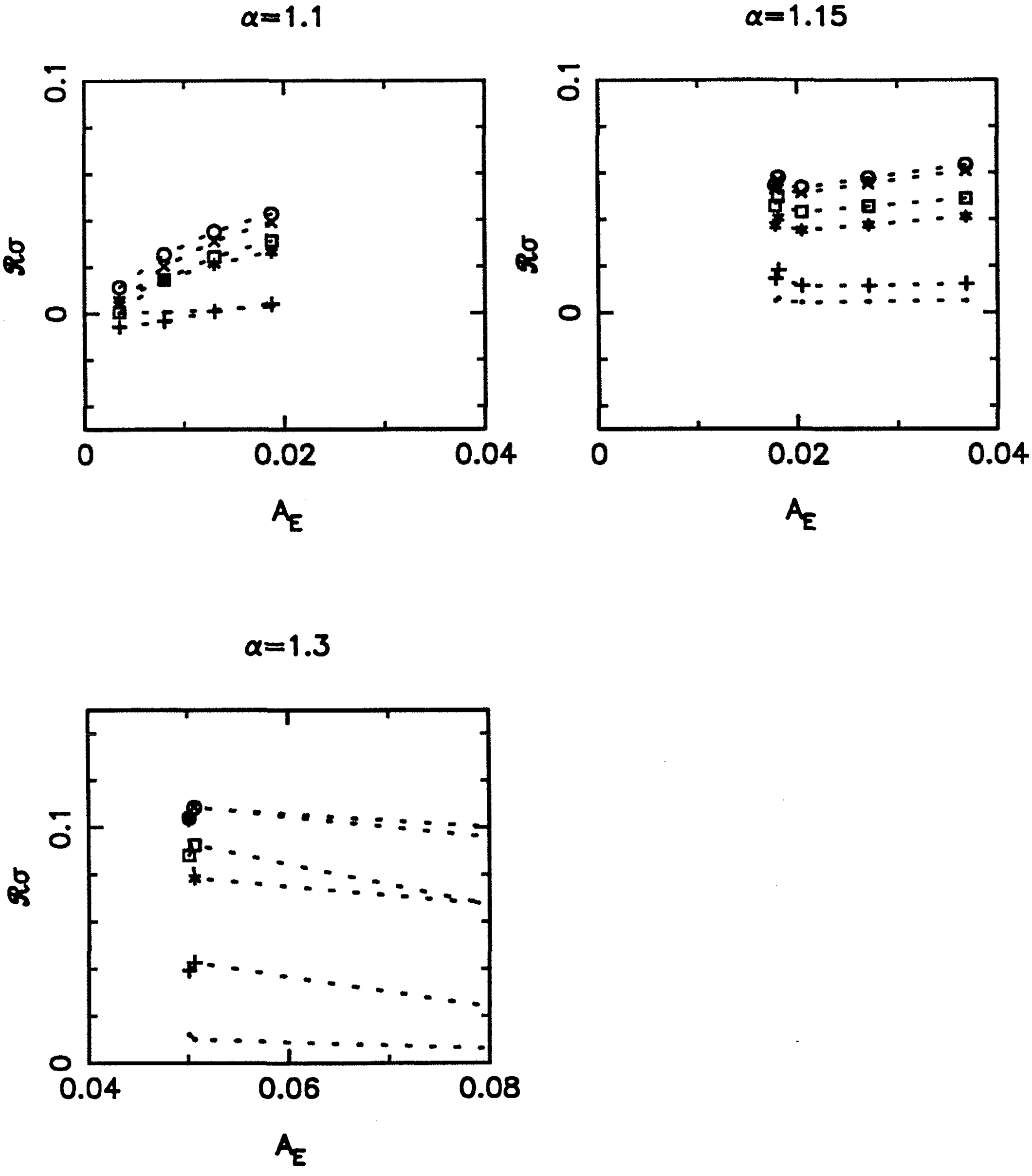

FIGURE 4.15. Growth rates for $\alpha = 1.1, 1.15, 1.3$ ($N = 1, K = 32, 50$).

Most unstable eigenvalue of the subharmonic stability problem for 2D ($\cdot$) and 3D disturbances β =0.25 (+), 0.5 (×), 1.0 (o), 2.0 (×),3.0 (□) vs. the amplitude of the 2D secondary flow, for low amplitude.

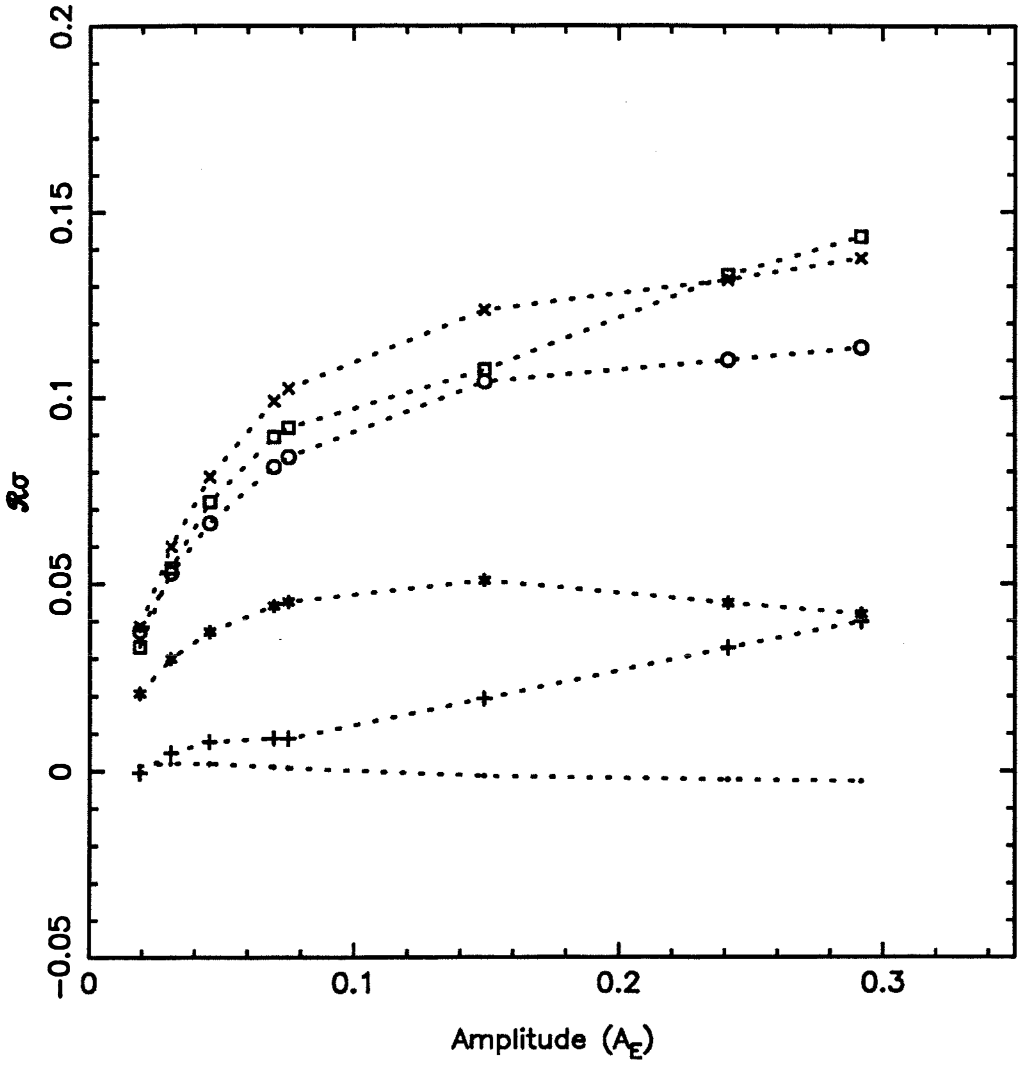

FIGURE 4.16. Growth rate of principal eigenvalue at $\alpha = 1$ ($N = 2, K = 32$).

Most unstable eigenvalue of the subharmonic stability problem for 2D (·) and 3D disturbances β =0.25 (+), 0.5 (×), 1.0 (o), 2.0 (×),3.0 (□) vs. the amplitude of the 2D secondary flow.

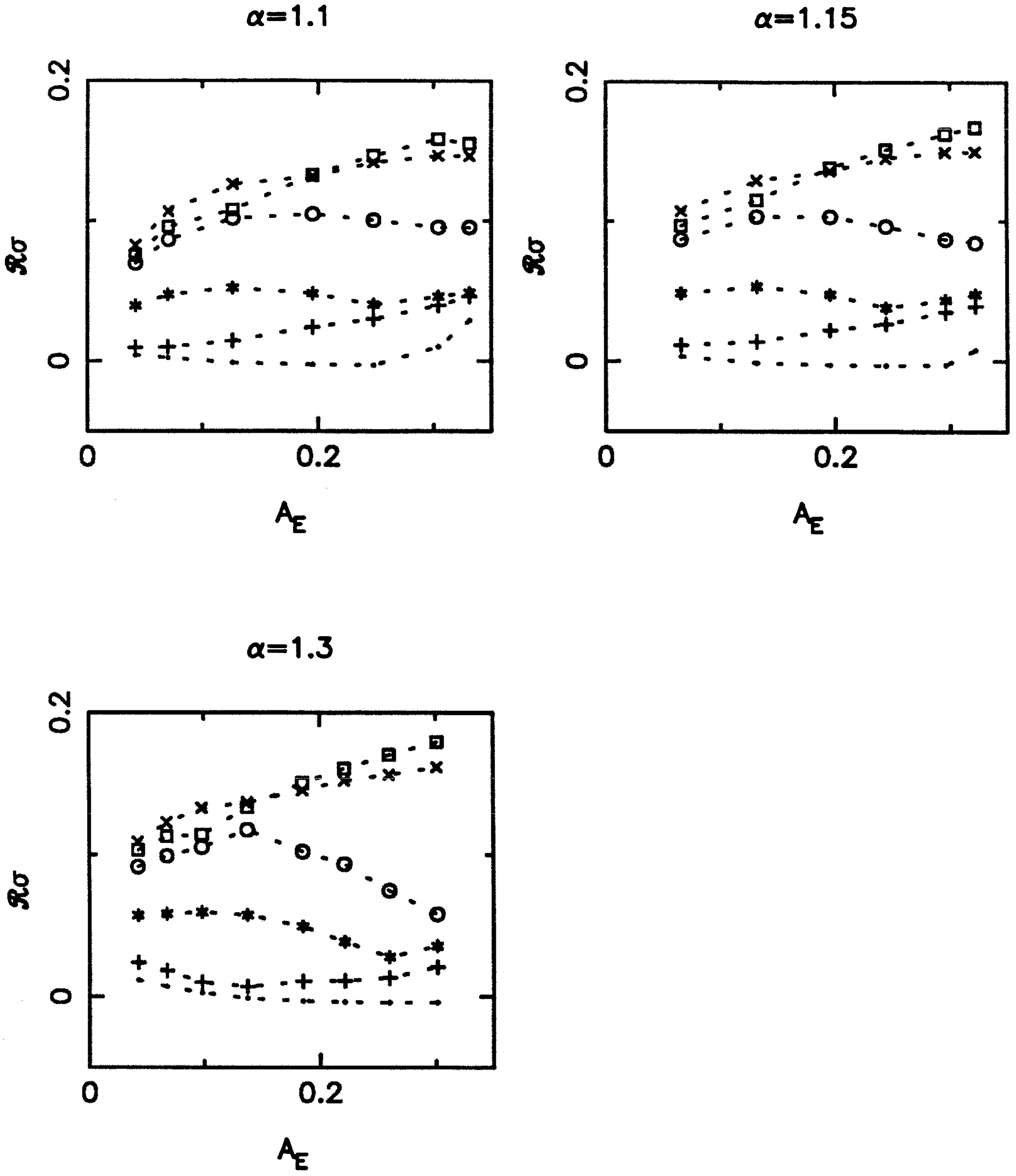

FIGURE 4.17. Growth rates for $\alpha = 1.1, 1.15, 1.3$ ($N = 2, K = 32$).

Most unstable eigenvalue of the subharmonic stability problem for 2D ($\cdot$) and 3D disturbances β =0.25 (+), 0.5 (×), 1.0 (o), 2.0 (×),3.0 (□) vs. the amplitude of the 2D secondary flow.

or

$$u_n(-y) = (-1)^{n+\frac{3}{2}} u_n(+y) \tag{4.14b}$$

(where $n = \pm 1/2, \pm 3/2, \ldots$), and an additional relation of the form

$$(u_{-n}, v_{-n}, w_{-n}) = (u_n^*, v_n^*, -w_n^*) \tag{4.15}$$

is not possible. If it did hold:

$$\begin{aligned} u_{\frac{1}{2}}(+y) &= u^*_{-\frac{1}{2}}(+y) && \text{by (4.15)} \\ &= (-1)^0 u^*_{-\frac{1}{2}}(-y) && \text{by (4.14a) for } n = -1/2 \\ &= u_{\frac{1}{2}}(-y) && \text{by (4.15)} \end{aligned}$$

which contradicts (4.14a) for $n = 1/2$.

Since (4.15) does not hold, then there are no purely real eigenvalues. It follows that, in general, for each point $(\mathbf{Re_Q}, \alpha)$ on the 2D secondary flow solution surface there is a spanwise wavenumber β which gives $R\sigma = 0, I\sigma \neq 0$ or maybe $R\sigma \neq 0, I\sigma = 0$ but not $\sigma \equiv 0$. However, by keeping $R\sigma = 0$ and varying one of the 2D parameters, we can find a point $(\mathbf{Re_Q}, \alpha)$ with a certain β which gives $\sigma \equiv 0$. Thus for subharmonic stability there exists a *curve* of bifurcation points on the 2D solution surface, as opposed to superharmonic stability where every point on the 2D surface is a bifurcation point.

It is not easy to continue in β and $\mathbf{Re_Q}$ (say), because the basic 2D steady flow changes for each stability problem. It is tedious, although possible, to fix α, compute the stability problem over a range of $\mathbf{Re_Q}$ and find the β which gives $I\sigma = 0$ (by continuation in β) at each $\mathbf{Re_Q}$. Then one can use bisection to refine the $\mathbf{Re_Q}$ value to eventually find $\sigma = 0$.

This process can be improved by starting near the Orr-Sommerfeld curve, for which the appropriate $(\mathbf{Re_Q}, \alpha, \beta)$ bifurcation point is easy to compute. The form of the 2D neutrally stable ($\sigma = 0 + i\sigma_i$) Orr-Sommerfeld curve in $(\mathbf{Re_Q}, \alpha, 0)$ can be computed. The intersection point of the 3D subharmonic bifurcation curve with the Orr-Sommerfeld curve is that point where the 3D subharmonic disturbance $(\alpha/2, \beta)$ has the same phase speed $c = \sigma_i$ as the 2D superharmonic disturbance $(\alpha, 0)$. This point is easily found using Squire's transformation, which for any 3D disturbance $(\mathbf{Re_Q}, \alpha/2, \beta)$ gives a 2D disturbance $(\tilde{\mathbf{Re}}_\mathbf{Q}, \tilde{\alpha}, 0)$ with the same stability $\tilde{\sigma} = \sigma$, where

$$\tilde{\alpha}^2 = \left(\frac{\alpha}{2}\right)^2 + \beta^2, \tag{4.16}$$

$$\tilde{\mathbf{Re}}_\mathbf{Q}\tilde{\alpha} = \left(\frac{\alpha}{2}\right) \mathbf{Re_Q}. \tag{4.17}$$

The problem is thus reduced to finding two points on the 2D Orr-Sommerfeld curve $(\mathbf{Re_Q}, \alpha)$ and $(\tilde{\mathbf{Re}}_\mathbf{Q}, \tilde{\alpha})$, related by (4.17), with the same phase speed $c = \tilde{c}$. This is true for only one point $(\mathbf{Re_Q}^*, \alpha^*)$. The 3D subharmonic disturbance is then $(\mathbf{Re_Q}^*, \alpha^*/2, \beta^*)$ with β^* given by (4.16). This bifurcation point was found to be approximately $\mathbf{Re_Q}^* = 11664, \alpha^* = 1.0881, \beta^* = 0.709$ with $c^* = 0.2391$. Although it was not possible to continue directly from here onto 3D waves, a nearby point on the 2D secondary flow surface gave the necessary starting point. The resulting solutions are presented in Chapter 5, 3D STEADY WAVES.

CHAPTER 5

3D STEADY WAVES

5.1 **Problem formulation**

We take the 3D incompressible Navier-Stokes equations in their vorticity formulation:

$$\frac{\partial \boldsymbol{\omega}}{\partial t} + (\mathbf{u} \cdot \nabla)\boldsymbol{\omega} = (\boldsymbol{\omega} \cdot \nabla)\mathbf{u} + \nu\nabla^2\boldsymbol{\omega}, \tag{5.1}$$

$$\boldsymbol{\nabla} \cdot \mathbf{u} = 0, \tag{5.2}$$

where $\boldsymbol{\omega} = \xi\mathbf{i} + \eta\mathbf{j} + \zeta\mathbf{k} = \boldsymbol{\nabla} \times \mathbf{u}$. Nondimensionalizing by the channel half-width h and some characteristic velocity U_0, looking for steady travelling waves $\mathbf{u}(x, y, z, t) = \mathbf{u}(x - ct, y, z)$ (but putting x for $x - ct$ for convenience) and then writing $\mathbf{u}(x, y, z) = (U - c)\mathbf{i} + \mathbf{u}_{3\mathrm{D}}(x, y, z)$ (with $\Omega = -dU/dy$, the z-vorticity of the PPF), (5.1) becomes

$$\begin{aligned} -\frac{1}{\mathbf{Re}}\nabla^2\boldsymbol{\omega} + \left((U - c)\frac{\partial}{\partial x} + (\mathbf{u} \cdot \nabla)\right) (\Omega\mathbf{k} + \boldsymbol{\omega}) \\ - \left((\boldsymbol{\omega} \cdot \nabla) + \Omega\frac{\partial}{\partial z}\right)((U - c)\mathbf{i} + \mathbf{u}) = 0, \end{aligned} \tag{5.3}$$

where the 3D subscript has been dropped. After expansion, (5.3) becomes

$$\begin{aligned} -\frac{1}{\mathbf{Re}}\nabla^2\boldsymbol{\omega} + (U - c)\frac{\partial \boldsymbol{\omega}}{\partial x} - \Omega\frac{\partial \mathbf{u}}{\partial z} + v\frac{d\Omega}{dy}\mathbf{k} - \eta\frac{dU}{dy}\mathbf{i} \\ + (\mathbf{u} \cdot \nabla)\boldsymbol{\omega} - (\boldsymbol{\omega} \cdot \nabla)\mathbf{u} = 0. \end{aligned} \tag{5.4}$$

Combining the x and z vorticity equations by subtracting the x derivative of the z equation from the z derivative of the x equation gives

$$\frac{1}{\mathbf{Re}}\nabla^4 v - (U-c)\frac{\partial}{\partial x}\nabla^2 v - \frac{d\Omega}{dy}\frac{\partial v}{\partial x}$$
$$+\frac{\partial}{\partial z}((\mathbf{u}\cdot\nabla)\xi - (\boldsymbol{\omega}\cdot\nabla)u) - \frac{\partial}{\partial x}((\mathbf{u}\cdot\nabla)\zeta - (\boldsymbol{\omega}\cdot\nabla)w) = 0, \quad (5.5)$$

$$-\frac{1}{\mathbf{Re}}\nabla^2\eta + (U-c)\frac{\partial\eta}{\partial x} - \Omega\frac{\partial v}{\partial z} + (\mathbf{u}\cdot\nabla)\eta - (\boldsymbol{\omega}\cdot\nabla)v = 0, \quad (5.6)$$

$$\nabla\cdot\mathbf{u} = 0. \quad (5.7)$$

We now look for solutions periodic in x and z (with wavenumbers α and β respectively):

$$\mathbf{u}(x,y,z) = \sum_{m=-\infty}^{+\infty} e^{i\beta mz} \sum_{n=-\infty}^{+\infty} e^{i\alpha nx}\hat{\mathbf{u}}_{mn}(y). \quad (5.8)$$

Substituting in (5.5)-(5.7) and zeroing termwise, the modal equations for mode (m,n) are

$$\frac{1}{\mathbf{Re}}\left((S_x^2+S_z^2)^2 + 2(S_x^2+S_z^2)\frac{d^2}{dy^2} + \frac{d^4}{dy^4}\right)v_{mn}$$
$$-(U-c)S_x\left(S_x^2+S_z^2+\frac{d^2}{dy^2}\right)v_{mn} - \frac{d\Omega}{dy}S_x v_{mn}$$
$$+S_z((u*\xi_x + v*\frac{d\xi}{dy} + w*\xi_z) - (\xi*u_x + \eta*\frac{du}{dy} + \zeta*u_z))$$
$$-S_x((u*\zeta_x + v*\frac{d\zeta}{dy} + w*\zeta_z) - (\xi*w_x + \eta*\frac{dw}{dy} + \zeta*w_z) = 0, \quad (5.9)$$

$$-\frac{1}{\mathbf{Re}}\left(S_x^2+S_z^2+\frac{d^2}{dy^2}\right)\eta_{mn} + (U-c)S_x\eta_{mn} - \Omega S_z v_{mn}$$
$$+(u*\eta_x + v*\frac{d\eta}{dy} + w*\eta_z) - (\xi*v_x + \eta*\frac{dv}{dy} + \zeta*v_z) = 0, \quad (5.10)$$

$$S_x u_{mn} + \frac{dv_{mn}}{dy} + S_z w_{mn} = 0, \tag{5.11}$$

(having dropped the hats on $\mathbf{u}_{mn}$), where the convolution $f * g$ for mode (m,n) is defined as $f * g = \sum_{p=-\infty}^{+\infty} \sum_{q=-\infty}^{+\infty} f_{m-p,n-q} g_{pq}$. Also, $S_x = i\alpha n x$ and $S_z = i\beta m z$ but for convenience we have used f_x in the convolutions to denote $i\alpha n f_{mn}$. The applicable no-slip boundary conditions at the channel walls are

$$u_{mn}(\pm 1) = v_{mn}(\pm 1) = w_{mn}(\pm 1) = 0. \tag{5.12}$$

We restrict our search to solutions with the reflectional symmetry

$$(u(-z), v(-z), w(-z)) = (u(z), v(z), -w(z)),$$

which corresponds to a modal symmetry of the form

$$(u_{-mn}, v_{-mn}, w_{-mn}) = (u_{mn}, v_{mn}, -w_{mn}). \tag{5.13}$$

Such a symmetry is consistent with periodic pairs of counter-rotating longitudinal vortices, aligned in the x-direction (as observed by Nishioka *et al.*, 1978). In addition, we impose a reality condition $\mathbf{u}_{-mn} = \mathbf{u}^*_{m-n}$ which, with (5.13), implies $(u_{m-n}, v_{m-n}, w_{m-n}) = (u^*_{mn}, v^*_{mn}, -w^*_{mn})$.

The use of these symmetries means we can solve for only modes $m \geq 0, n \geq 0$. Some further simplifications are possible, depending on the particular modes. If $m > 0, n \geq 0$, we solve for (u_{mn}, v_{mn}) and use the continuity equation (5.11) to compute w_{mn}. If $m = 0, n > 0$ then (5.13) implies that $w_{0n} = -w_{0n} = 0$. Since (5.10) is satisfied identically in this case, we use (5.9) only, solve for v_{0n} and use (5.11) to compute u_{0n}.

Finally, if $m = n = 0$, in addition to (5.13) implying that $w_{00} = 0$, the continuity equation (5.11) shows that $dv_{00}/dy \equiv 0$, which with (5.12) shows $v_{00} \equiv 0$. Furthermore, in this case (5.9) and (5.10) are identically zero and we must return to the z-vorticity equation which in modal form appears

$$\frac{1}{\mathbf{Re}}\frac{d^3u_{00}}{dy^3} + (u * \zeta_x + v * \frac{d\zeta}{dy} + w * \zeta_z) - (\xi * w_x + \eta * \frac{dw}{dy} + \zeta * w_z) = 0, \qquad (5.14)$$

with boundary condition $u_{00}(\pm 1) = 0$. This leaves one boundary condition undetermined. As in the 2D case, this corresponds to fixing the parametrization (the nondimensionalization velocity U_0). We used a flux boundary condition (corresponding to $U_0 \equiv U_Q, \mathbf{Re} \equiv \mathbf{Re_Q}$) which here is written

$$\int_{-1}^{+1} u_{00}(y)dy = 0. \qquad (5.15)$$

In practice, the above scheme proved to be exceedingly ill-conditioned and convergence was not possible, even to existing 2D secondary flow solutions. However, by defining a stream-function such that $u_{00} = d\hat{\psi}_{00}/dy$ in (5.14), with boundary conditions

$$\hat{\psi}_{00}(\pm 1) = 0 \qquad (5.16a)$$

$$\hat{\psi}'_{00}(\pm 1) = 0 \qquad (5.16b)$$

the condition number in a typical case improved from 10^{18} to 10^8 and convergence to both 2D and 3D solutions was obtained. This redefinition of the $m = n = 0$ modes does not change the counting, so it is not immediately clear why there is an improvement in the conditioning. However, the highest order term in the stream-function formulation of (5.14) is the viscous 4th-order term. In the discretized equations, these 4th-order terms appear in the diagonal and close off-diagonal elements of the coefficient matrix, along with the 4th- and 2nd-order terms from the remaining primitive variable equations, (5.9) and (5.10). The particular coefficients appearing are derivatives of the Chebyshev modes, $T_k^{(p)}(y)$. Because $T_k^{(p)}(y) \sim k^{2p}$ (Orszag and Gottlieb, 1977), it is plausible that the stream-function formulation of (5.14) (with $p = 4$ for the viscous terms) tends to be more diagonally dominant than the primitive variable formulation (with $p = 3$), with a consequent improvement in the conditioning of the equations (Strang, 1980).

Auxiliary equations. As described in Chapter 2, 2D STEADY WAVES, a phase condition is necessary to remove the x-origin degeneracy. In the primitive variable case (2.10) becomes

$$I \int_{-1}^{+1} v_{01}(y)dy = 0.$$

Normally a similar phase condition would be necessary to fix the z-origin. However, the assumption of the symmetry (5.13) precludes any phase shift in the solution (since if u_{mn} is a solution satisfying (5.13), the shifted solution $u_{mn}e^{i\beta m\delta} \neq u_{-mn}e^{i\beta(-m)\delta}$ unless $\delta = 0$).

Flux and pressure Reynolds numbers are related by (2.13). Both a 2D and 3D amplitude can be defined using energy or L_2-norm methods:

$$\begin{aligned} A_{E,\mathrm{2D}}^2 &= {\sum_{n=-N}^{+N}}' E_{0n} \\ &= \frac{15}{16} {\sum_{n=-N}^{+N}}' \int_{-1}^{+1} |u_{0n}(y)|^2 + |v_{0n}(y)|^2 dy \end{aligned} \tag{5.17a}$$

$$\begin{aligned} A_{E,\mathrm{3D}}^2 &= {\sum_{m=-M}^{+M}}' \sum_{n=-N}^{+N} E_{mn} \\ &= \frac{15}{16} {\sum_{m=-M}^{+M}}' \sum_{n=-N}^{+N} \int_{-1}^{+1} |u_{mn}(y)|^2 + |v_{mn}(y)|^2 + |w_{mn}(y)|^2 dy \end{aligned} \tag{5.17b}$$

and

$$A_{2\mathrm{D}}^2 = \sum_{n=-N}^{+N}{}' \sum_{k=0}^{K} |a_{0nk}|^2 \tag{5.18a}$$

$$A_{3\mathrm{D}}^2 = \sum_{m=-M}^{+M}{}' \sum_{n=-N}^{+N} \sum_{k=0}^{K} |a_{mnk}|^2 + |b_{mnk}|^2. \tag{5.18b}$$

5.2 Numerical solution

Having truncated the systems of ODEs (5.9)-(5.12), (5.15) and (5.16) to some $m = 0, \ldots, M; n = 0, \ldots, N$, we used the same technique of spectral tau collocation as was described in Chapter 2, 2D STEADY WAVES. In the general $m > 0, n > 0$ case we used a Chebyshev expansion for both u and v, $u_{mn}(y) = \sum_{k=0}^{K} a_{mnk} T_k(y)$ and $v_{mn}(y) = \sum_{k=0}^{K} b_{mnk} T_k(y)$ and solved the resulting nonlinear algebraic system $F_i(\mathbf{a}, \mathbf{b}, \mathbf{Re_Q}, c, \alpha, \beta) = 0$ (with three fixed parameters) using Euler-Newton continuation.

5.3 Numerical results

As described in Chapter 4, 3D SUPERHARMONIC STABILITY, we used the 3D eigensolution from the linear stability problem as a starting guess for bifurcations into the space of 3D steady waves. As noted there, it is possible to start from several different bifurcation points, corresponding to different families in 3D space. We followed two antisymmetric families (A_1, A_2) (corresponding to the symmetry $u_{10}(-y) = -u_{10}(+y)$) and one symmetric family (S_1) (of the form $u_{10}(-y) = u_{10}(+y)$). Although the calculations were performed on a Cray-XMP, they are exceedingly time-consuming, so we had to be selective with the range of parameters considered. In Figures 5.1-5.3 we have plotted the 3D waves in $(\mathbf{Re_Q}, \beta, A_{E,3\mathrm{D}})$ space for the S_1 family at $\alpha = 1$, computed with $M = N = 1$ and $K = 50$. Figures 5.4-5.6 show the A_1 family for similar parameters.

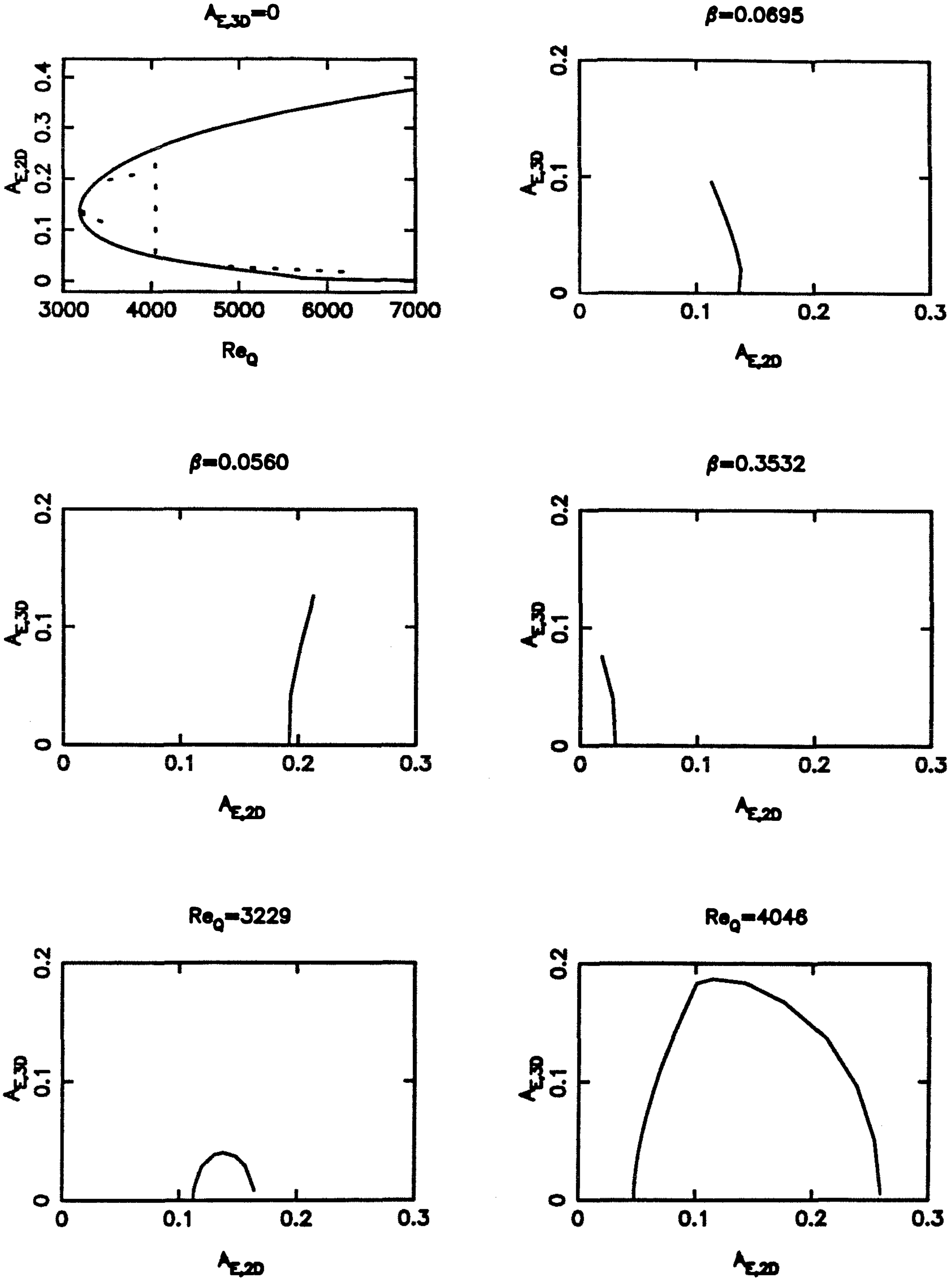

FIGURE 5.1. S_1 family at $\alpha = 1$ ($M = N = 1, K = 50$): $A_{E,2D}$-$A_{E,3D}$ plots.

Intersection with Re_Q-$A_{E,2D}$ plane (dashed lines show projections onto $A_{E,3D} = 0$ plane) and cross-sections in 3D space. The constant β plots are projections onto the $A_{E,2D}$-$A_{E,3D}$ plane.

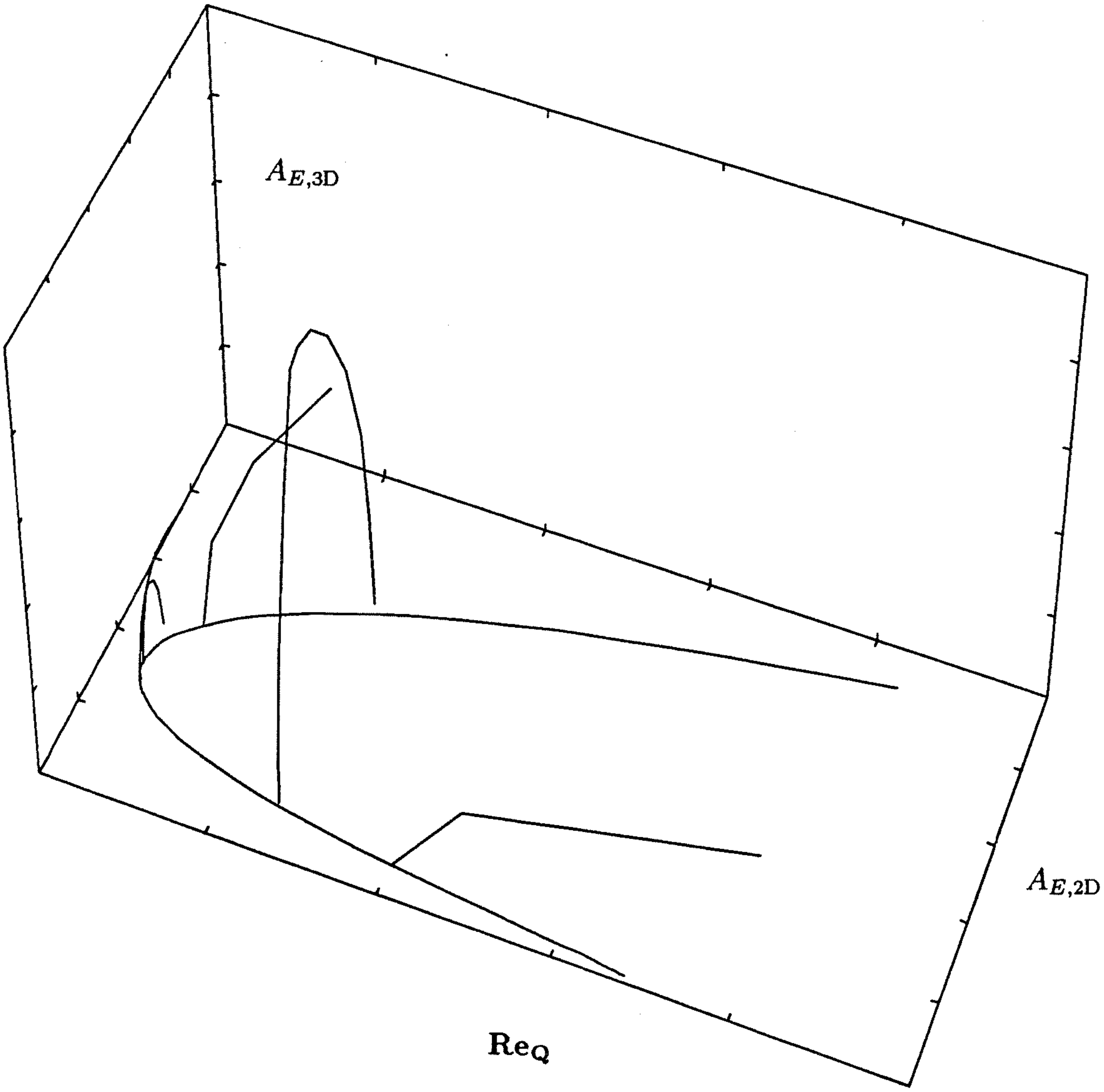

FIGURE 5.2. S_1 family at $\alpha = 1$ ($M = N = 1, K = 50$): Perspective sketch in ($\mathbf{Re_Q}, A_{E,2D}, A_{E,3D}$) space.

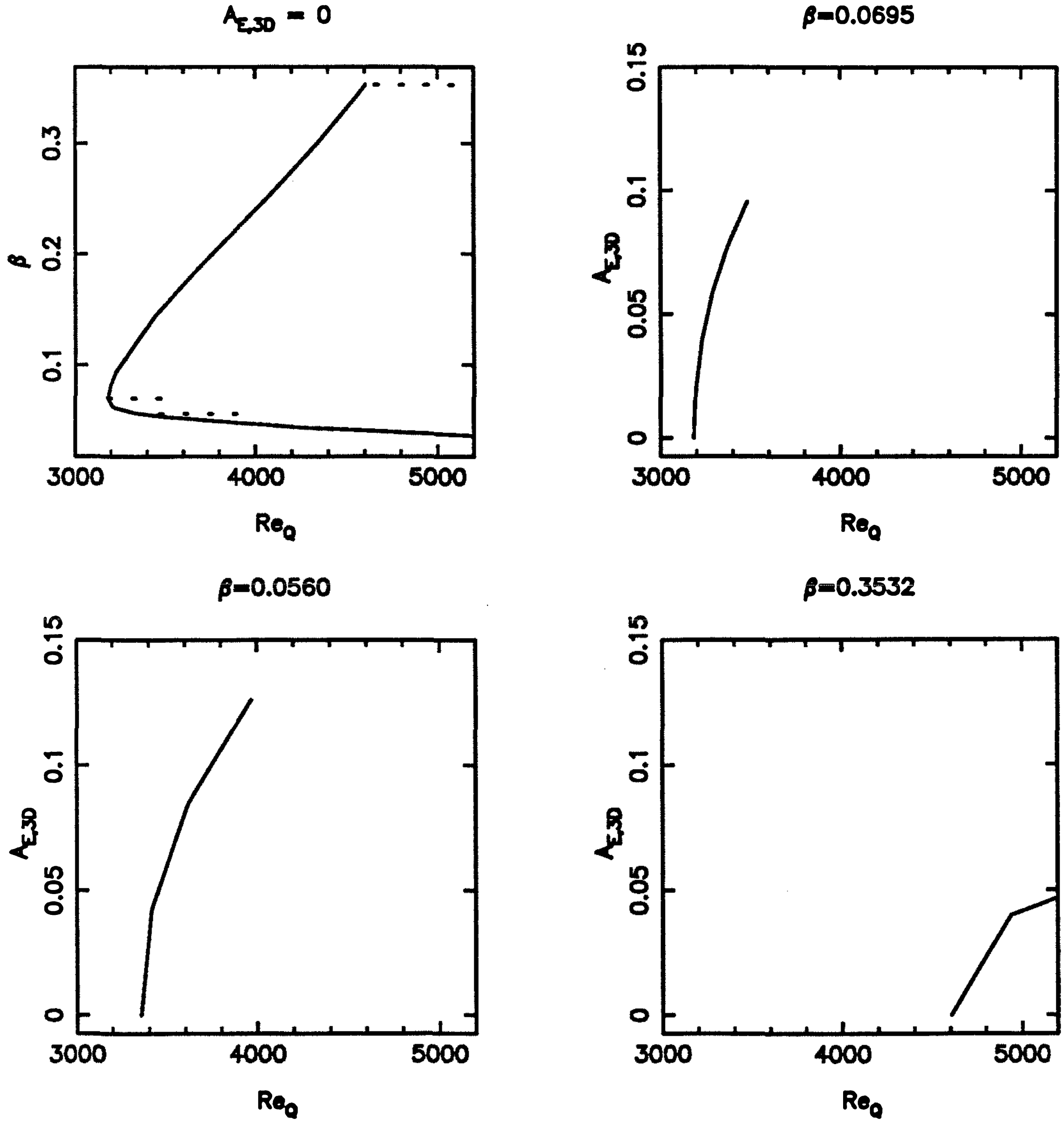

FIGURE 5.3. S_1 family at $\alpha = 1$ ($M = N = 1, K = 50$): constant β plots. Intersection with $\mathbf{Re_Q}$-β plane (dashed lines show projections onto $A_{E,3D} = 0$ plane) and cross-sections (at constant β) in 3D space.

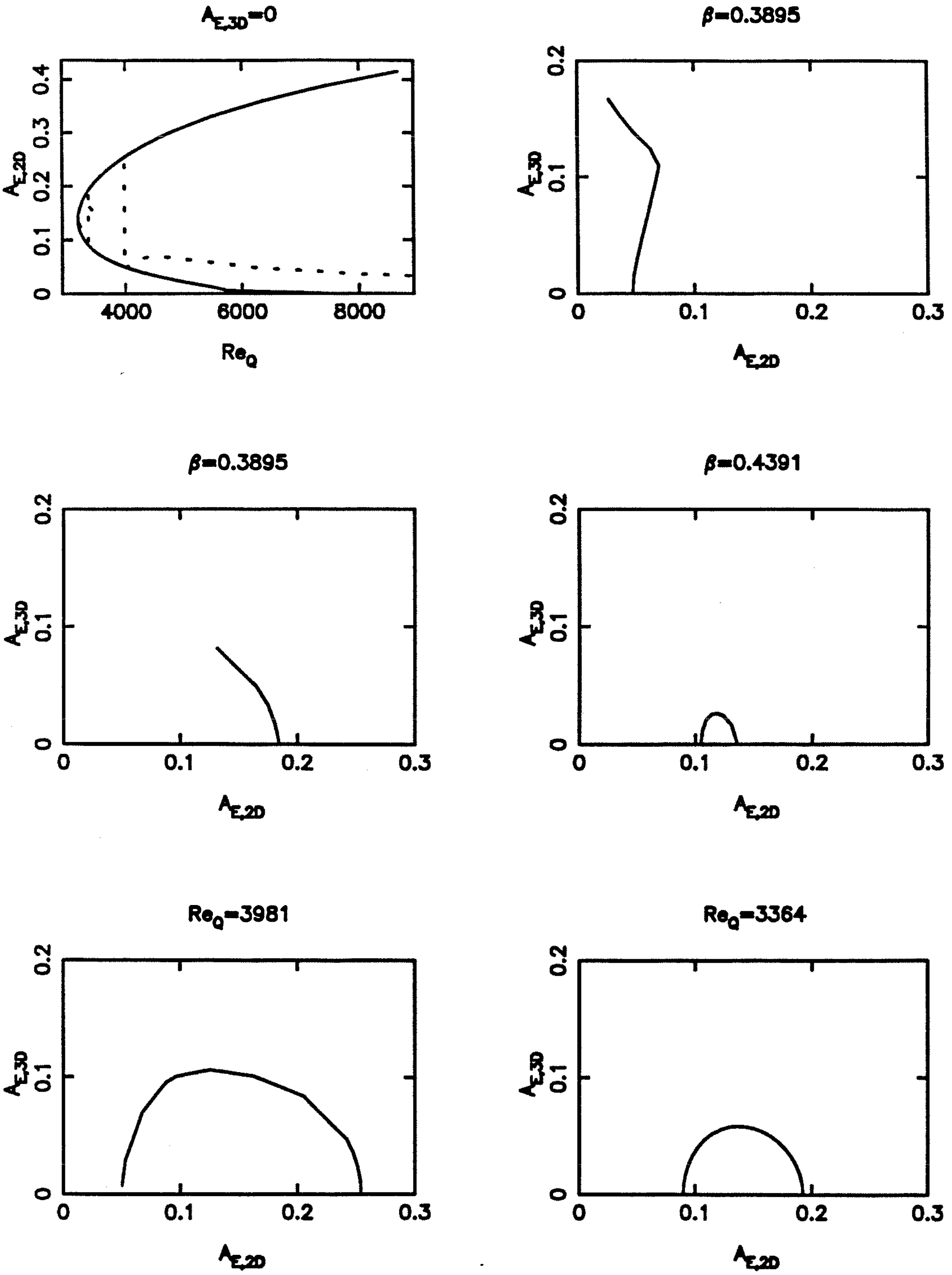

FIGURE 5.4. A_1 family at $\alpha = 1$ $(M = N = 1, K = 50)$: $A_{E,2D}$-$A_{E;3D}$ plots.

Intersection with Re_Q-$A_{E,2D}$ plane (dashed lines show projections onto $A_{E,3D} = 0$ plane) and cross-sections in 3D space. The constant β plots are projections onto the $A_{E,2D}$-$A_{E,3D}$ plane.

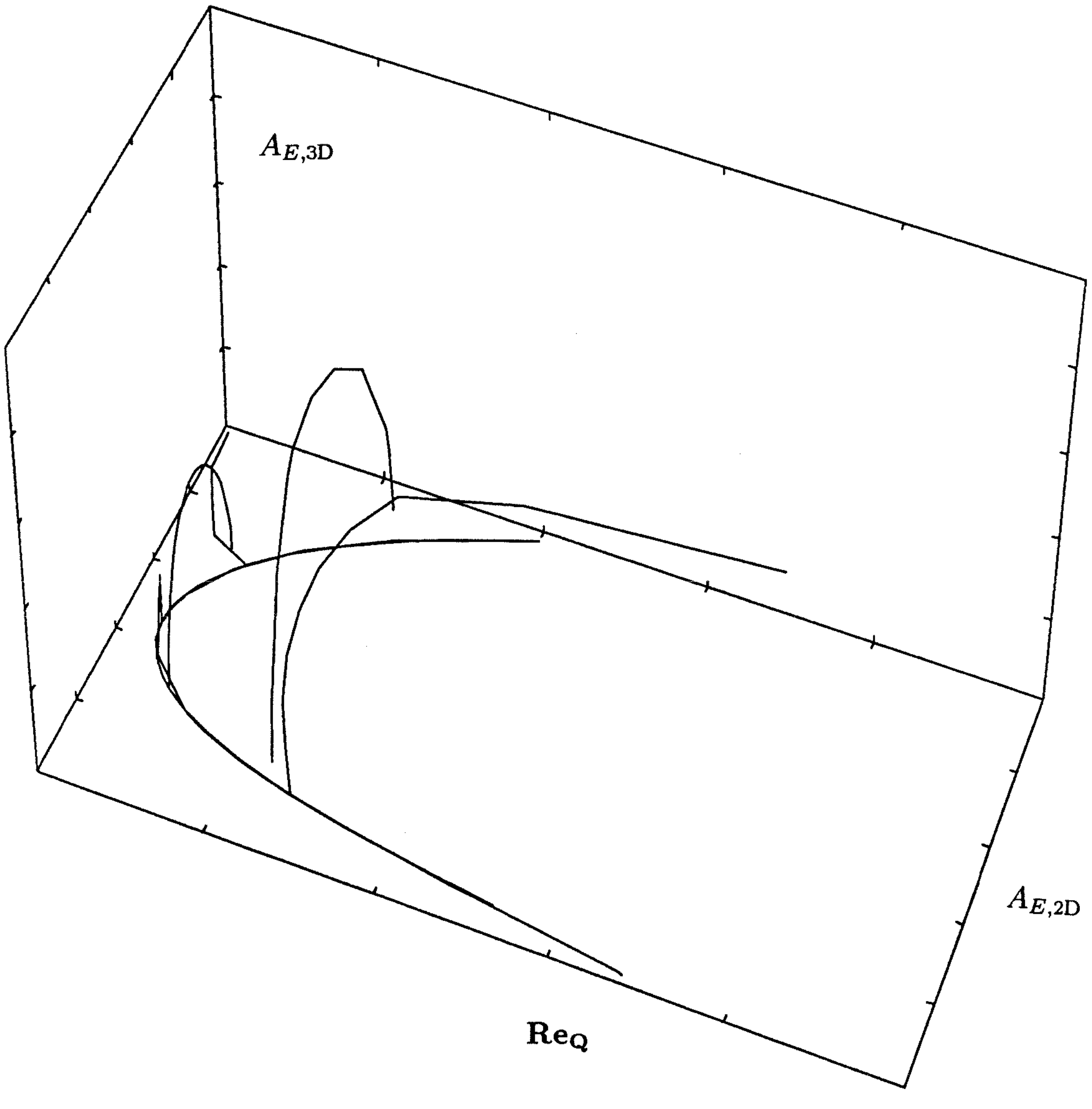

FIGURE 5.5. A_1 family at $\alpha = 1$ ($M = N = 1, K = 50$): Perspective sketch in $(\mathbf{Re_Q}, A_{E,2D}, A_{E,3D})$ space.

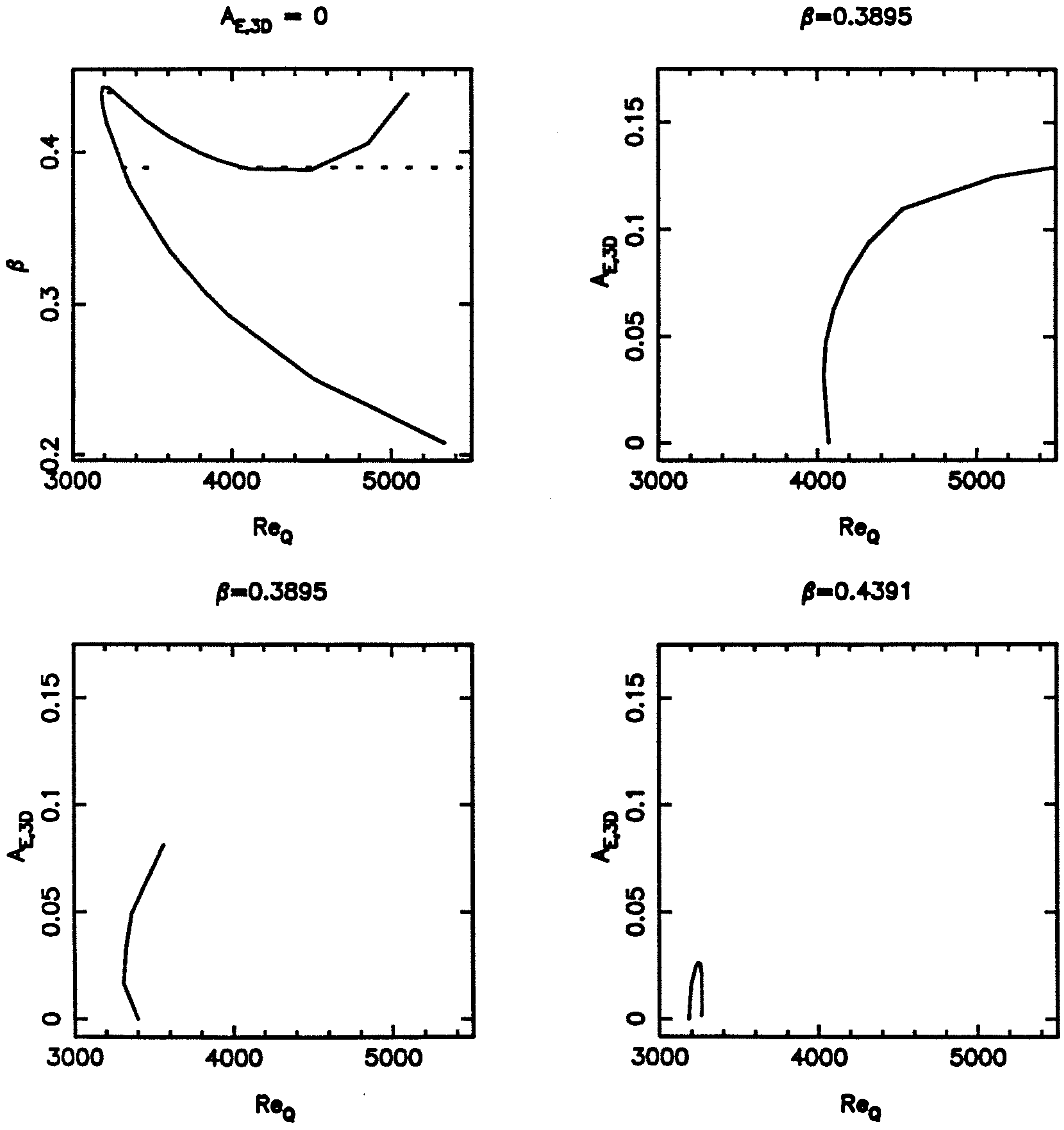

$A_{E,3D}$ = 0

β=0.3895

β=0.3895

β=0.4391

FIGURE 5.6. A_1 family at $\alpha = 1$ ($M = N = 1, K = 50$): constant β plots. Intersection with $\mathrm{Re_Q}$-β plane (dashed lines show projections onto $A_{E,3\mathrm{D}} = 0$ plane) and cross-sections (at constant β) in 3D space.

In Figures 5.7-5.9 we show the effect on the A_1-family of increasing the resolution in the x-direction. Although there are quantitative changes from Figures 5.4-5.6, the qualitative behavior is similar, in the same way as was observed for the 2D steady flows with increasing N. Finally, in Figures 5.10-5.12, we plot the A_2 family computed at $\alpha = 1.3$ with $M = 1, N = 2$ and $K = 40, 50$.

Data for these families were computed at other α's, but not in any detail. Nevertheless, they do support the behavior shown in the figures here. To cross-check the 3D calculations, we followed some families into 3D space (at higher amplitude) and back onto the 2D solutions again at a different point. The 2D parameters agreed with those calculated from the 2D steady waves code, and β at the bifurcation point from the 2D solutions (i.e., at $A_{E,\mathrm{3D}} = 0$) with the neutral stability point calculated with the 3D superharmonic stability code.

Comparing Figures 5.4-5.6 and 5.7-5.9, we see that the similarity of the A_1 family curves for $N = 1$ and $N = 2$ suggests that accurate conclusions can be drawn from these data in terms of the qualitative behavior for $M = 1$. The constant $\mathbf{Re_Q}$ cross-sections display the same sharp increase in $A_{E,\mathrm{3D}}$ *vs.* $A_{E,\mathrm{2D}}$ with a relatively slower decrease back to $A_{E,\mathrm{3D}} = 0$ on the upper branch of the 2D solution curve. There is no decrease in $A_{E,\mathrm{2D}}$ below the 2D value here and no decrease in $\mathbf{Re_Q}$ along the constant β curves.

Having noted that the qualitative behavior of the 3D solutions appears to be maintained for the A_1-family when the x-resolution is increased, we assume that the behavior shown in Figure 5.10 for $\alpha = 1.3$, A_2 family, is correct. Although the form of the β dependence with Reynolds number differs for the three families investigated (S_1, A_1, A_2), the amplitude *vs.* Reynolds number dependence shown for A_2 appears to be typical for all families. The 3D solutions show a sharp increase in $A_{E,\mathrm{3D}}$ with increasing $A_{E,\mathrm{2D}}$ and there is no reduction of $\mathbf{Re_Q}$ from the 2D value

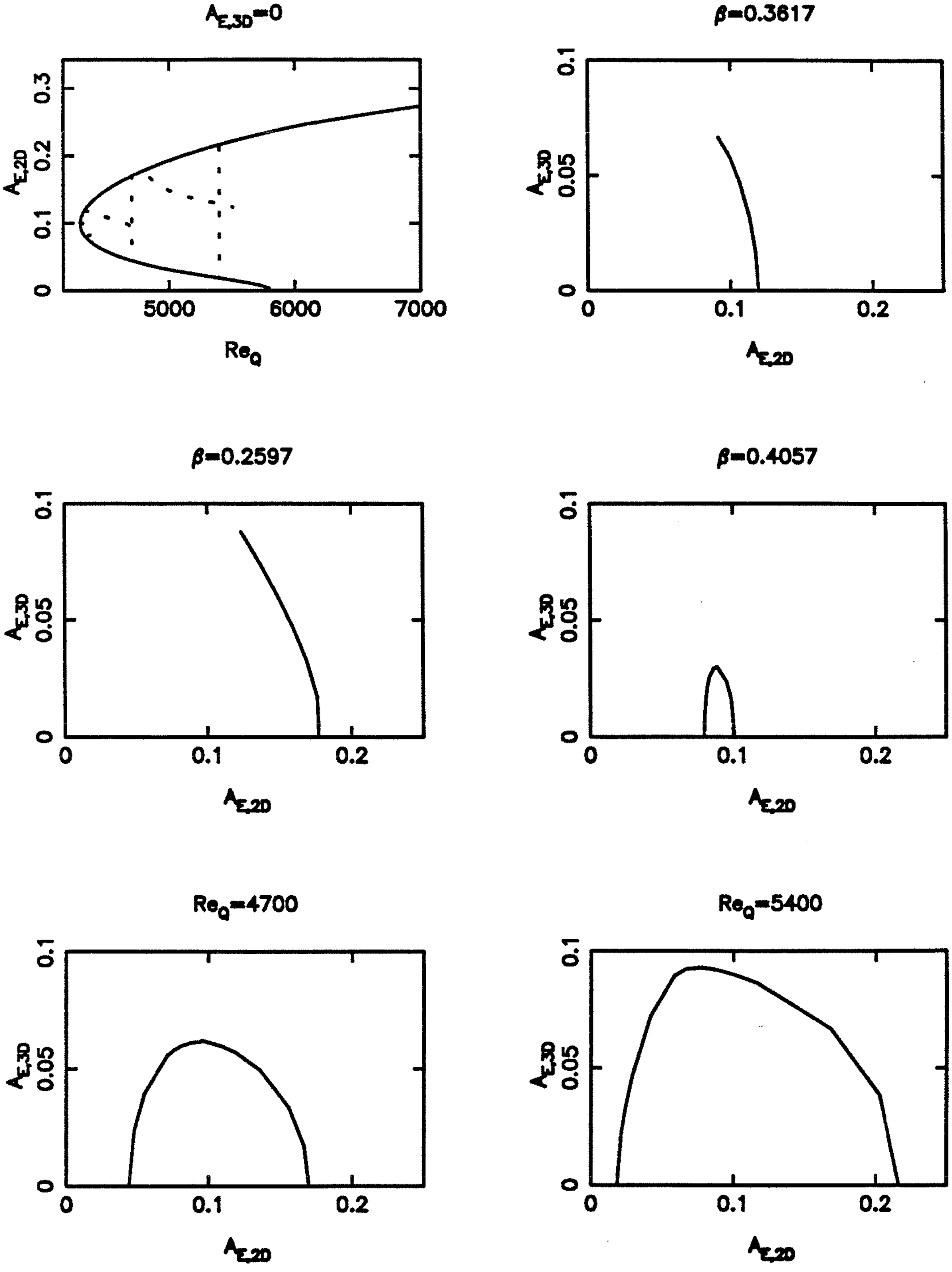

FIGURE 5.7. A_1 family at $\alpha = 1$ ($M = 1, N = 2, K = 40, 50$): $A_{E,\mathrm{2D}}$-$A_{E,\mathrm{3D}}$ plots.

Intersection with $\mathrm{Re_Q}$-$A_{E,\mathrm{2D}}$ plane (dashed lines show projections onto $A_{E,\mathrm{3D}} = 0$ plane) and cross-sections in 3D space. The constant β plots are projections onto the $A_{E,\mathrm{2D}}$-$A_{E,\mathrm{3D}}$ plane.

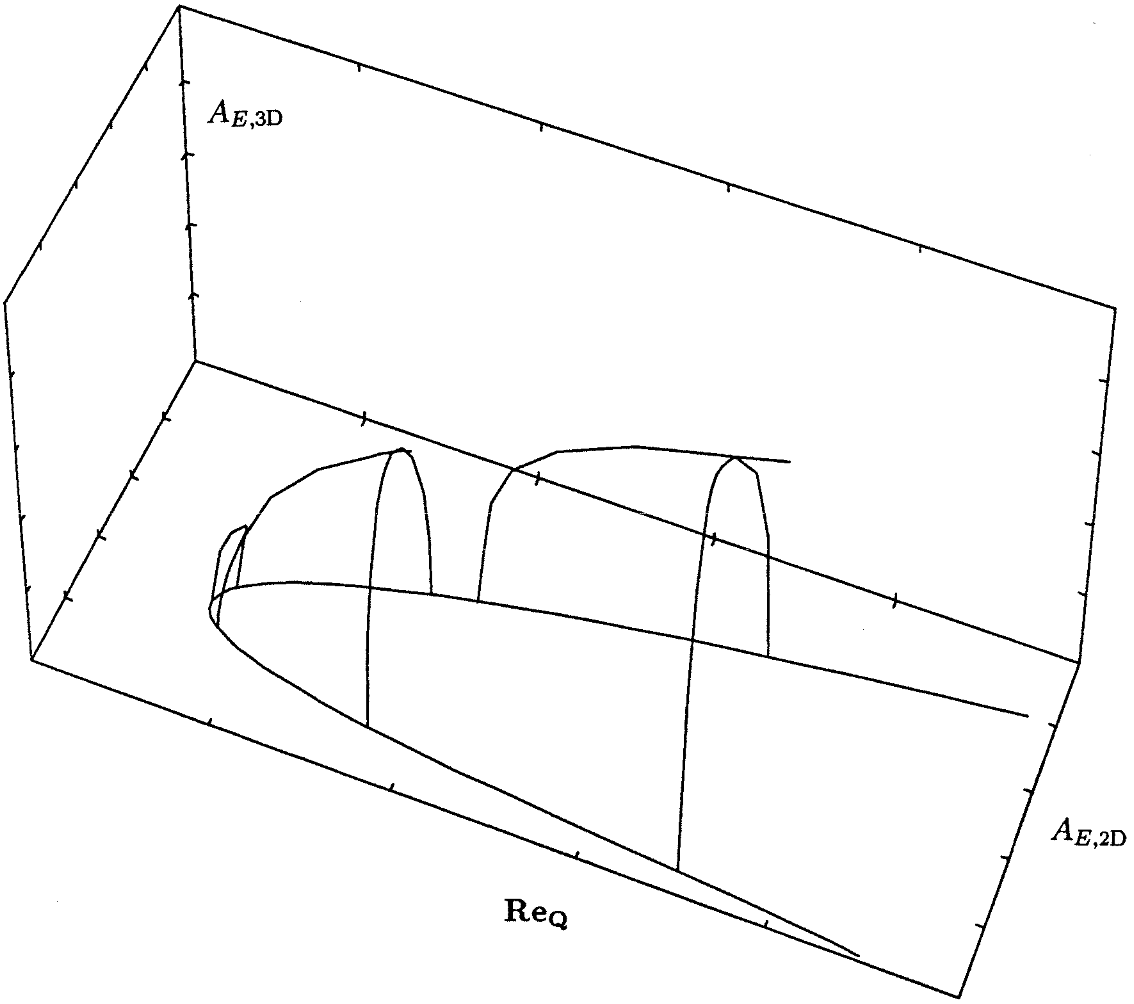

FIGURE 5.8. A_1 family at $\alpha = 1$ ($M = 1, N = 2, K = 40, 50$): Perspective sketch in ($\mathbf{Re_Q}, A_{E,2D}, A_{E,3D}$) space.

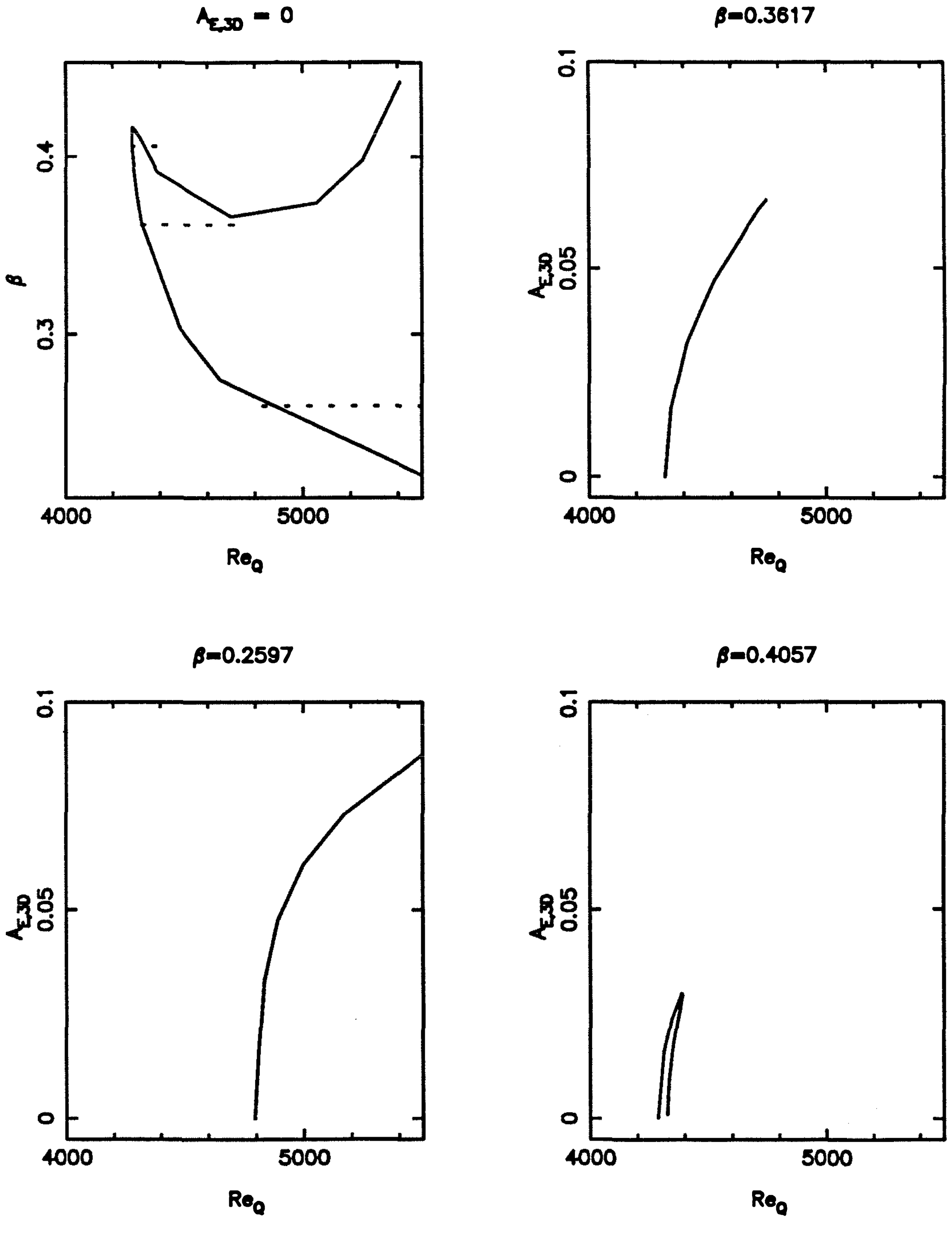

FIGURE 5.9. A_1 family at $\alpha = 1$ ($M = 1, N = 2, K = 40, 50$): constant β plots. Intersection with Re_Q-β plane (dashed lines show projections onto $A_{E,3D} = 0$ plane) and cross-sections (at constant β) in 3D space.

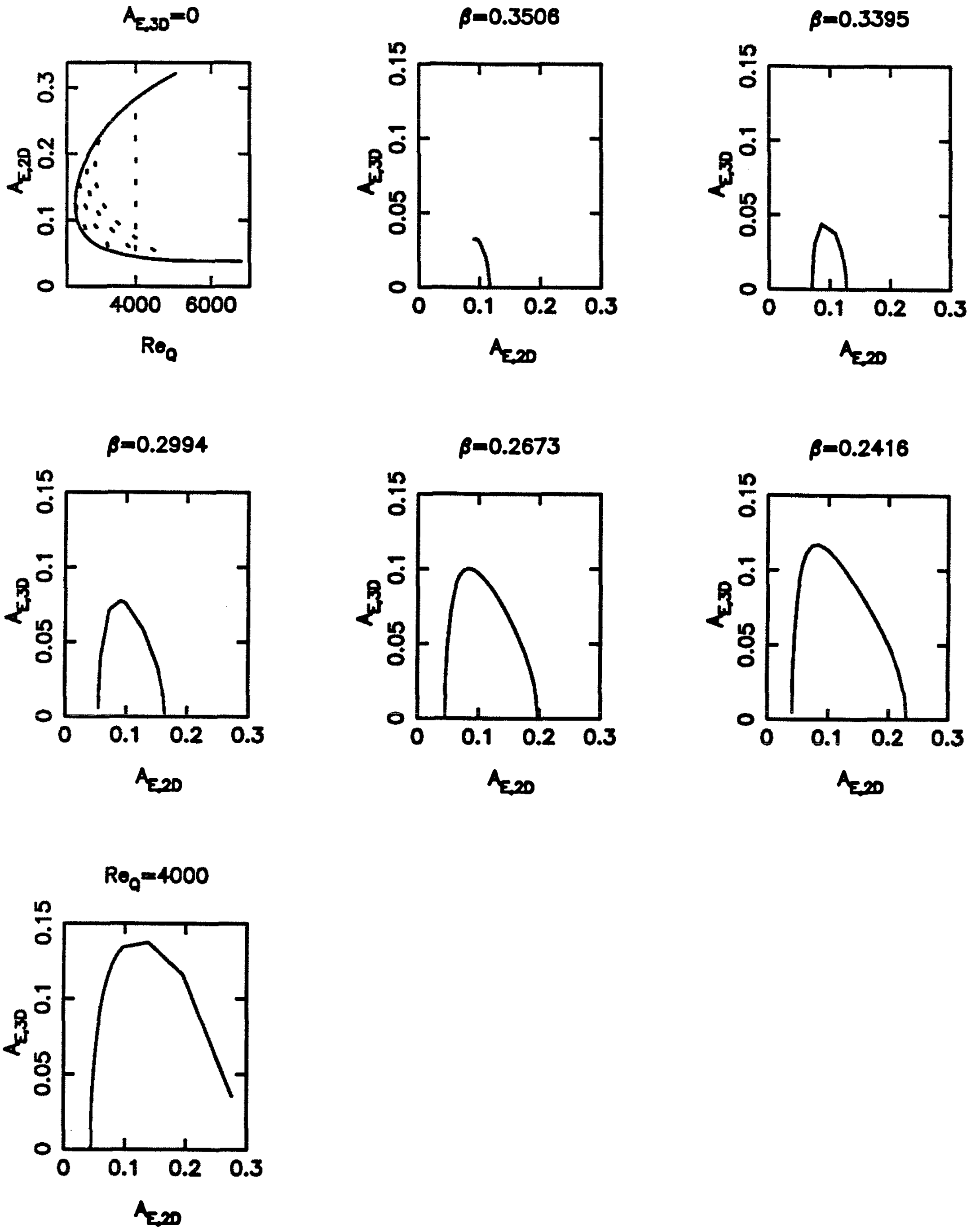

FIGURE 5.10. A_2 family at $\alpha = 1.3$ ($M = 1, N = 2, K = 40, 50$): $A_{E,\mathrm{2D}}$-$A_{E,\mathrm{3D}}$ plots.

Intersection with Re_Q-$A_{E,\mathrm{2D}}$ plane (dashed lines show projections onto $A_{E,\mathrm{3D}} = 0$ plane) and cross-sections in 3D space. The constant β plots are projections onto the $A_{E,\mathrm{2D}}$-$A_{E,\mathrm{3D}}$ plane.

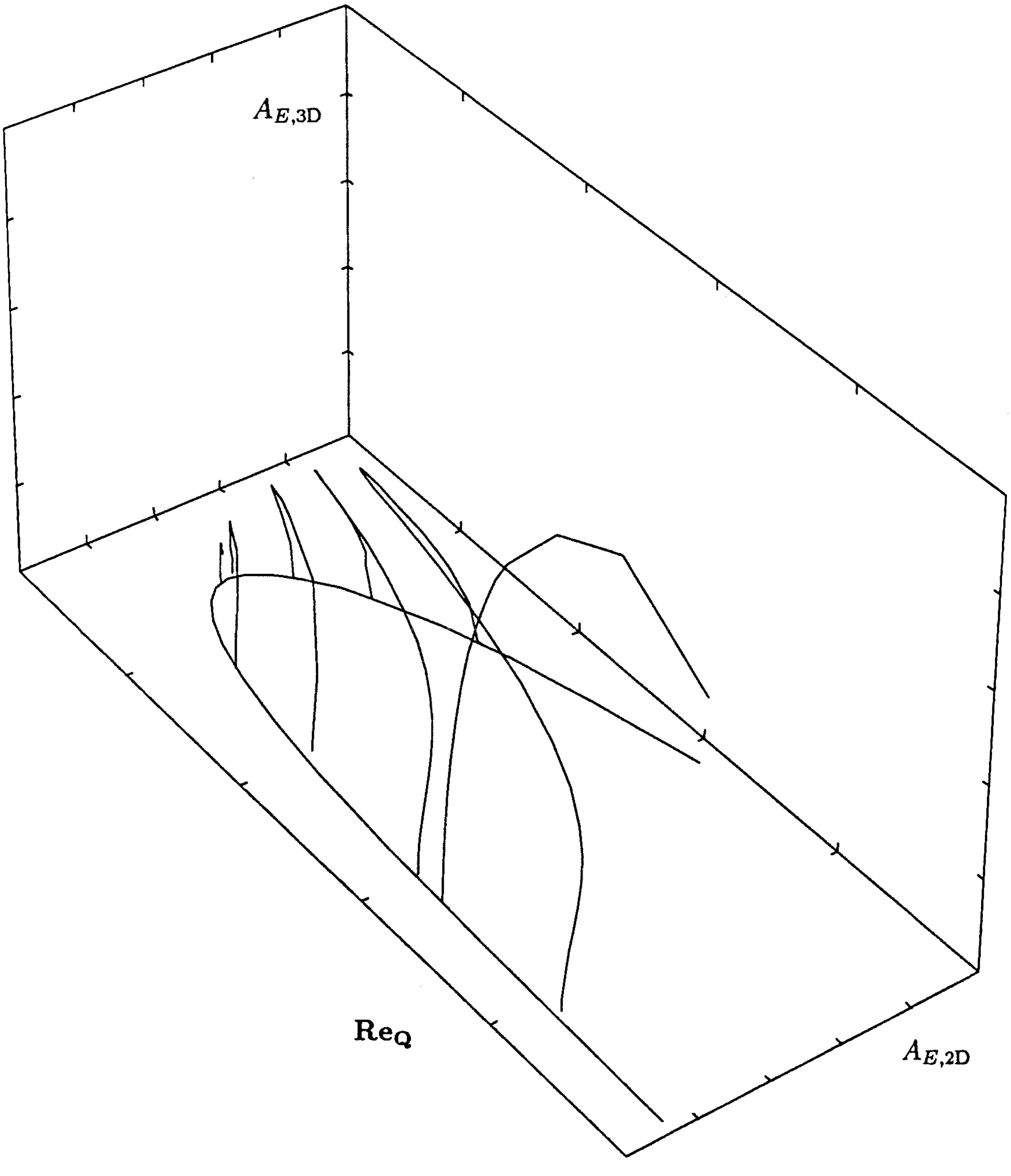

FIGURE 5.11. A_2 family at $\alpha = 1.3$ ($M = 1, N = 2, K = 40, 50$): Perspective sketch in $(\mathbf{Re_Q}, A_{E,2D}, A_{E,3D})$ space.

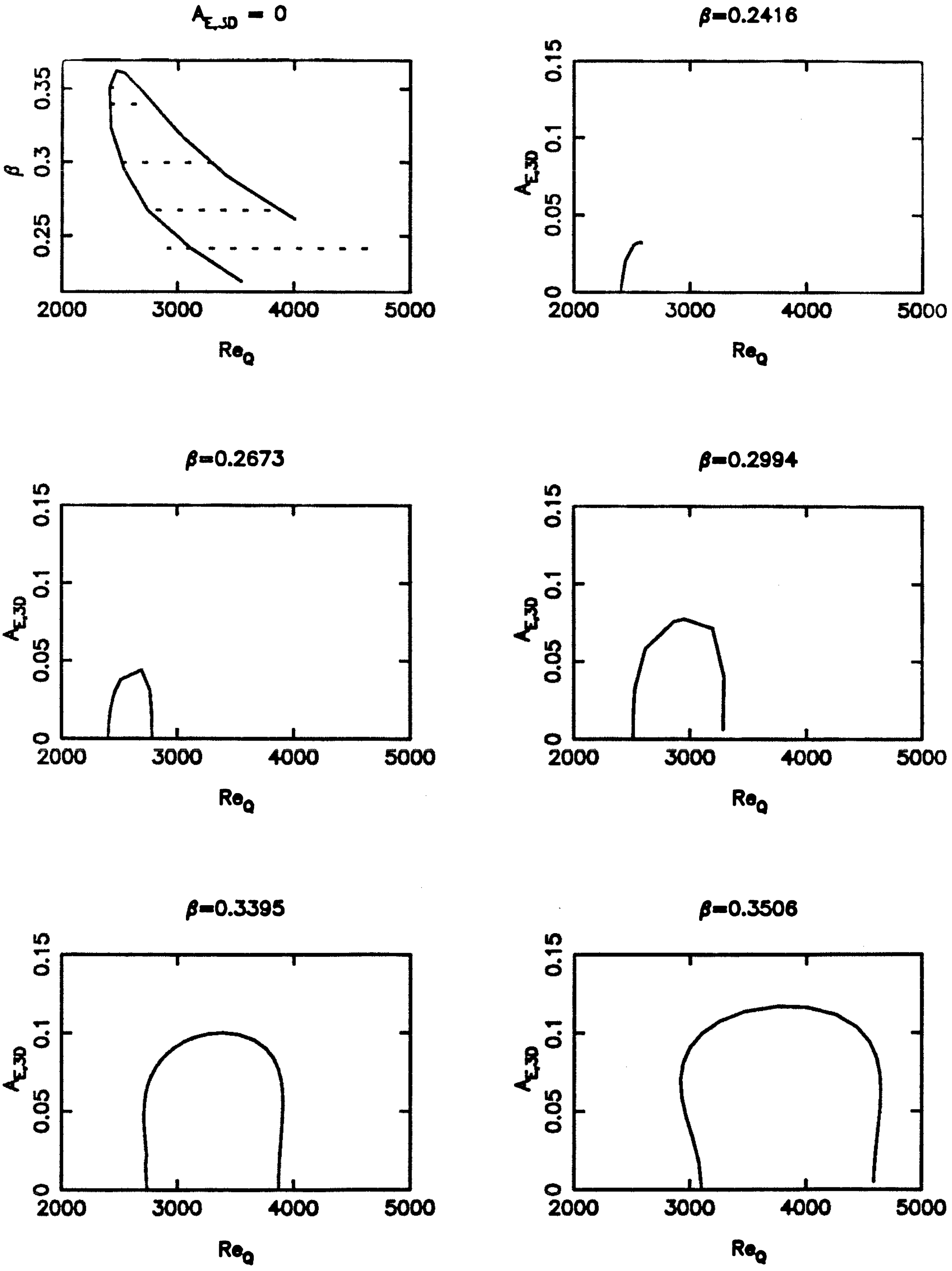

$A_{E,3D} = 0$

β=0.2416

β=0.2673

β=0.2994

β=0.3395

β=0.3506

FIGURE 5.12. A_2 family at $\alpha = 1.3$ ($M = 1, N = 2, K = 40, 50$): constant β plots. Intersection with $\mathrm{Re_Q}$-β plane (dashed lines show projections onto $A_{E,3D} = 0$ plane) and cross-sections (at constant β) in 3D space.

so that the 2D solution curve is the envelope of the 3D solutions in the $\mathbf{Re_Q}$-$A_{E,\mathrm{2D}}$ plane. We did not compute any solutions with increased z-resolution but suspect that the important effects occur in the streamwise direction and that the spanwise behavior is adequately resolved for qualitative conclusions to be made, particularly regarding the Reynolds number behavior.

Form of the 3D superharmonic flow. In Figure 5.13 we show the perturbation to the mean flow ($u_{00}(y)$) plotted for various 3D amplitudes along the constant $\beta = 0.2994$ cross-section shown in Figure 5.10, going from large to smaller 2D amplitude (upper to lower branch of the 2D solution curve). Noting that for the 2D solution curve, the energy in the mean flow increases monotonically as one moves from the lower to the upper branch (corresponding to a transfer of energy into the 2D perturbation), we see that this process is modified for the 3D waves. Examination of the profile and of the energies shown for each subplot shows that the 3D flow perturbation draws energy primarily from the mean flow (so that the mean flow energy *decreases* as the 3D amplitude increases, even as we move towards the lower branch of the 2D solution curve). This observation for these 3D secondary flows is consistent with the analysis of Orszag and Patera (1983) who observed that in time-dependent 3D flows the 2D flow mediated the transfer of energy from the mean flow to the 3D disturbance.

Examination of the velocity vectors of the 3D flows on this $\beta = 0.2994$ cross-section reveals that the flow remains essentially two-dimensional, with the xy-plane flow similar to that shown in Figure 4.9 for all z positions. In Figure 5.14 we show the wv velocity field in the zy-plane, at various x locations. Note that the velocity scale in each subplot is different. With this pattern at each cross-section, particle paths will tend to be helices (because they are swept down the channel from one cross-section to the next). The observed symmetry in the flow, and the

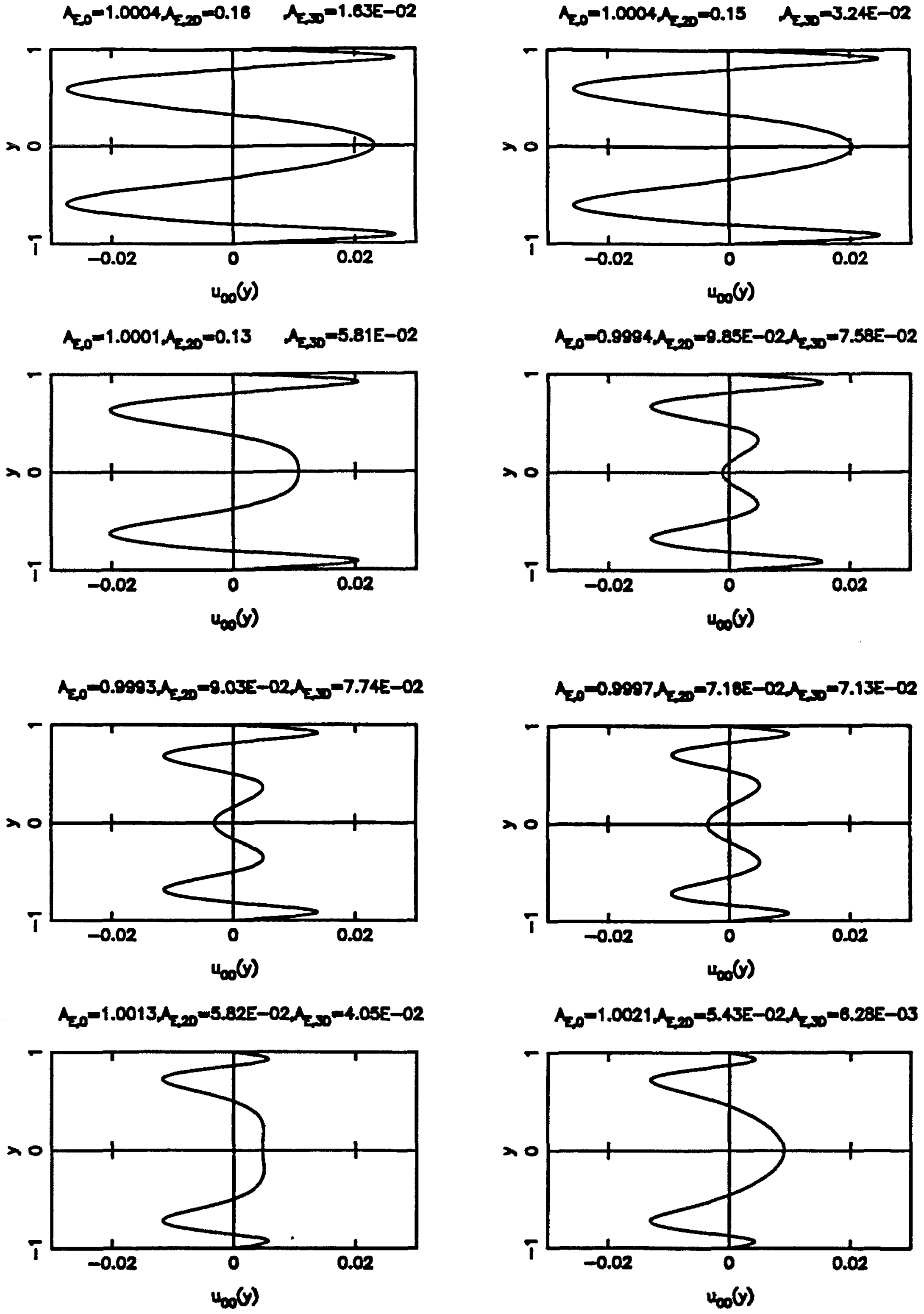

FIGURE 5.13. Mean flow perturbation along $\beta = 0.2994$ cross-section in Figure 5.10.

consequent suggestion of counter-rotating vortices, are results of the symmetry assumption (5.13).

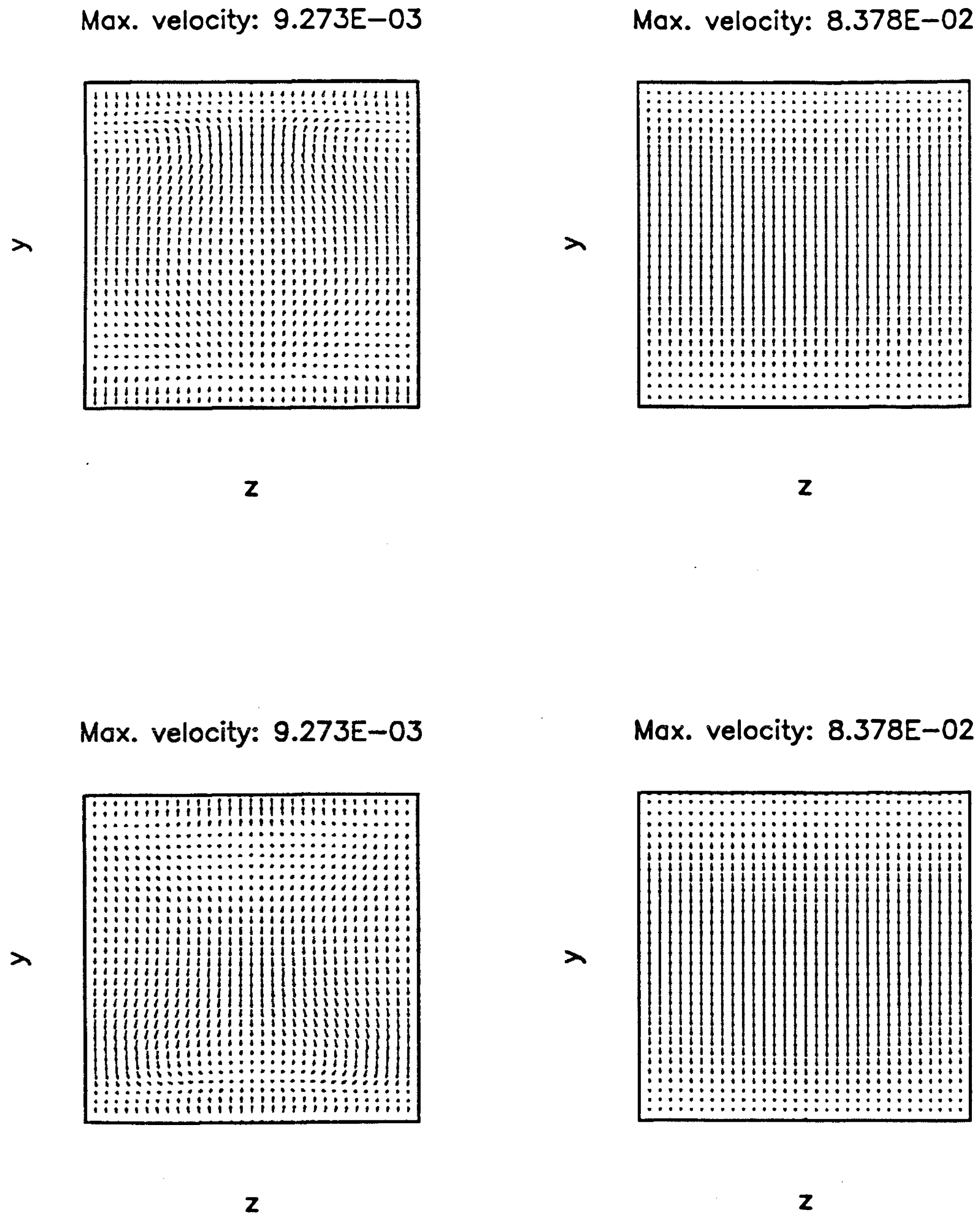

FIGURE 5.14. Velocity vectors in the yz-plane for the point $\beta = 0.2994$, $A_{E,3D} = 7.74 \times 10^{-4}, \alpha = 1.3$. Cross-sections plotted at $2\pi/(4\alpha)$ intervals in the x-direction. The distance scale on each subplot is 0-$2\pi/\beta$ in z, and -1 to $+1$ in y.

5.4 3D subharmonic waves

Starting from the curve of bifurcation points off the 2D secondary flow solutions, we have continued these solutions into the 3D space of subharmonic steady waves. The equations are as before, except that now we expand the $m > 0$ modes in both sub- and superharmonic components:

$$\mathbf{u}(x, y, z) = \sum_{n=-\infty}^{+\infty} \hat{\mathbf{u}}_{0n}(y) e^{i\alpha n x} + \sum_{m=-\infty}^{+\infty}{}' \sum_{n=-\infty}^{+\infty} \hat{\mathbf{u}}_{mn}(y) e^{i\alpha \frac{n}{2} x} \tag{5.19}$$

Note that a complete expansion does involve both types of modes for $m > 0$. However, for simplicity we assume that $m > 0$ superharmonic modes are zero and look for solutions in which the 3D components are purely subharmonic and the 2D components purely superharmonic:

$$\mathbf{u}(x, y, z) = \sum_{n=-\infty}^{+\infty} \hat{\mathbf{u}}_{0n}(y) e^{i\alpha n x} + \sum_{m=-\infty}^{+\infty}{}' \sum_{n=-\infty}^{+\infty} \hat{\mathbf{u}}_{mn}(y) e^{i\alpha (n+\frac{1}{2}) x} \tag{5.20}$$

We assume that the symmetry (5.13) still applies for the superharmonic modes $m = 0$. The equations and auxiliary relationships are the same as for the 3D superharmonic solutions. However, the reduction in the number of degrees of freedom means that of the parameters $(\mathbf{Re_Q}, \alpha, \beta, A_{E,\mathrm{2D}}, A_{E,\mathrm{3D}})$ we can fix two and determine the others (unlike the 3D superharmonic solutions).

5.5 Numerical results

The most computational effort, involving much trial and error, involved the reduction of $\mathbf{Re_Q}$ down to the $\mathbf{Re_Q} \approx 2500$ regime. In Figure 5.15 we present amplitude-Reynolds numbers plots (analagous to those for 2D secondary flows) for a range of α, computed with $M = N = 1, K = 50$. The behavior in these plots is somewhat similar to that for 2D secondary flows; a surface of solutions with a "nose" in $(\mathbf{Re_Q}, \alpha, A_{E,\mathrm{3D}})$ space. As Figure 5.15 shows, the minimum occurs at $\mathbf{Re_Q} \approx 1600$ for $\alpha \approx 1$.

This minimum does not agree with the results of Goldshtik *et al.* (1983), who found a minimum Reynolds number of $\mathbf{Re_Q} = 1017$ for $\alpha = 1.166$ using a finite difference code with (so far as we can ascertain from their paper) $M = N = 1$ and 101 Chebyshev-spaced collocation points. They used second-order differencing in the y-direction. Milinazzo and Saffman (1985) used a finite-difference scheme with up to fifth-order differencing and found that up to 200 points in y were needed to achieve convergence on a stretched grid when solving the 2D equations. This leads us to believe that Goldshtik's resolution might be inadequate. We tried to simulate the effects of such reduced y-resolution by reducing the number of modes from $K = 40$ to $K = 32$ at this minimum point. With the spectral collocation method, no significant change occurred. This does not, of course, rule out the possibility of inaccuracies in a finite difference formulation. When we used inadequate resolution in some of our test computations we found completely erroneous branches of solutions which disappeared when the mesh size was reduced in y. Such a check may not have been possible for Goldshtik because of computational limitations.

Nevertheless, this is a considerable reduction in Reynolds number from the secondary flow minimum of $\mathbf{Re_Q} = 2600$ (for $\alpha = 1.32, N = 4$) and is much closer to the experimentally determined transition value of $\mathbf{Re_Q} = 1000$. Given the quantitative changes in the 2D minimum with increasing N, this certainly raised the possibility that increasing the x-resolution here would reduce the minimum of $\mathbf{Re_Q} = 1600$ down closer to the transition value.

We were unsuccessful in converging directly from $M = N = 1, K = 50$ to the $M = 1, N = 2, K = 50$ solution surface. The only alternative was to start again

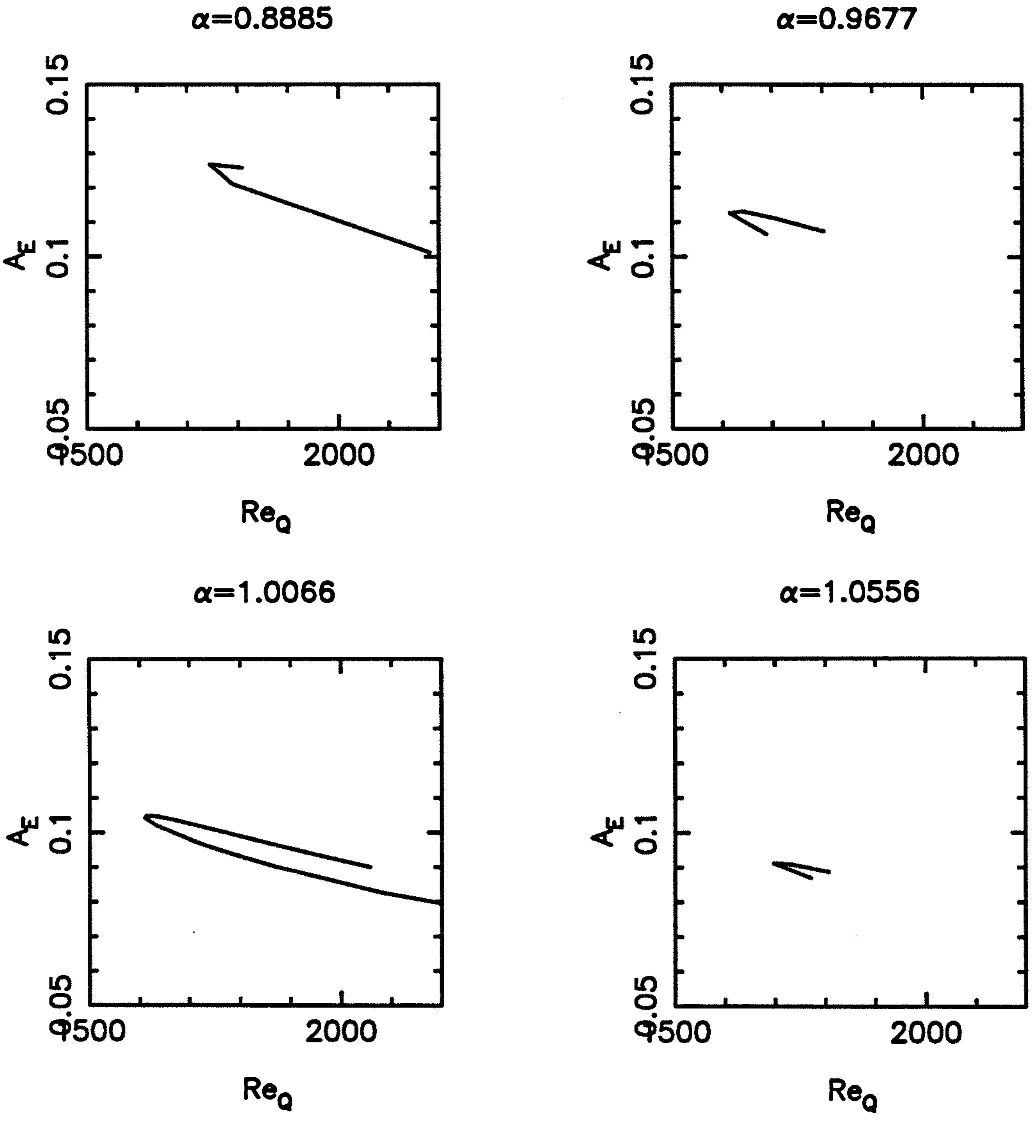

FIGURE 5.15. 3D subharmonic steady waves ($M = N = 1, K = 50$).

Cross-sections at different α for solution surface near minimum Re_Q.

at the bifurcation point at $\mathbf{Re_Q} = 11664$ and attempt to repeat the continuation process to low Reynolds number. However, no reduction in Reynolds number was possible. At a given α the bifurcation was either super-critical, or sub-critical with a small $\mathbf{Re_Q}$ decrease to a limit point in $\mathbf{Re_Q}$ and subsequent increase in $\mathbf{Re_Q}$. Such a drastic qualitative change in behavior from the $M = N = 1, K = 50$ solution surface is astounding and was not observed in the superharmonic waves calculations. It has to be attributed to some interaction between Fourier modes that were not present in the $N = 1$ approximation, but it is not clear what modes these would be.

In Figure 5.16 we show the behavior of the 3D secondary flow surface computed with $M = 1, N = 2, K = 50$. There is no longer any reduction in Reynolds number from the bifurcation point at $\mathbf{Re_Q} = 11664$ on the Orr-Sommerfeld curve (marked with the symbol on Figure 5.16). Instead the behavior is much more like that for 3D superharmonic waves except that at high Reynolds numbers the amplitude $A_{E,\mathrm{2D}}$ does increase beyond the 2D value. The y dependence of the solution is surprisingly difficult to resolve and we found $K = 69$ Chebyshev modes necessary.

Evidence of convergence. It is natural to ask whether the curves in Figure 5.16 are accurate representations of the converged solution or whether further changes occur as N or K is increased, similar to the significant change from $N = 1$ to $N = 2$. In Figure 5.17 we show the $\mathbf{Re_Q} = 13365$ cross-section computed with $N = 1, K = 69$, $N = 2, K = 49$, $N = 2, K = 69$ and various points (symbols in the figure) with $N = 3, K = 49$ ($N = 3, K = 69$ was not possible because of memory limitations). The largest qualitative change occurs from $N = 1$ to $N = 2$, but the behavior is then reasonably resolved with $N = 2, K = 49$. In Figure 5.18 we plot the decay of the Chebyshev coefficients (plotted on a linear-log scale) for some of the Fourier modes, for the maximum $A_{E,\mathrm{3D}}$ point for $\mathbf{Re_Q} = 13365$, computed with $N = 2, K = 69$. The modes which are identically zero (by symmetry) are

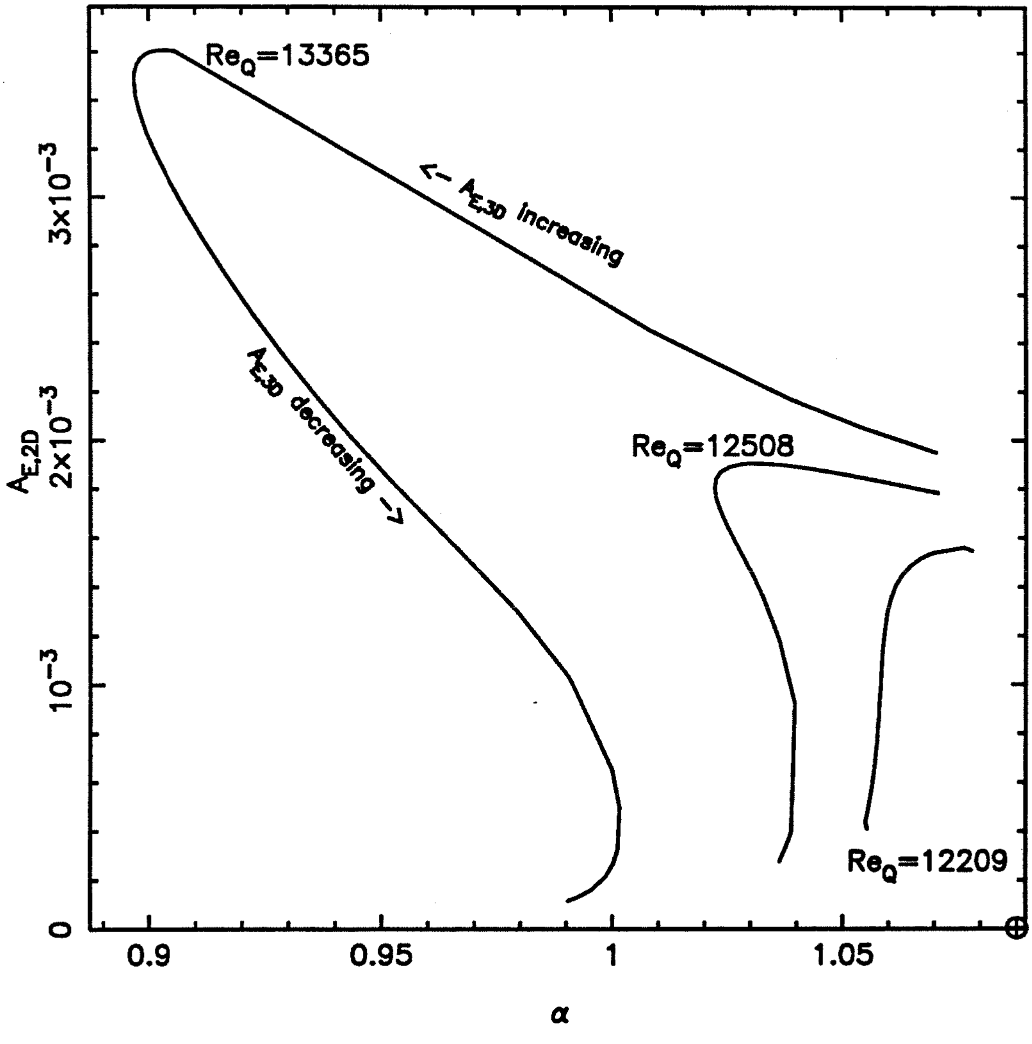

FIGURE 5.16. 3D subharmonic steady waves $(M = 1, N = 2, K = 69)$. Cross-sections at different $\mathbf{Re_Q}$ for solution surface near the bifurcation point (symbol $\oplus$) at $\mathbf{Re_Q} = 11664, \alpha = 1.0881$

not plotted. Although there is some evidence of aliasing in the highest modes, exponential decay (indicative of convergence of the expansion) appears to have been achieved.

In Table 5.1 we show the modal energies for the largest $A_{E,\mathrm{3D}}$ point on the $\mathbf{Re}_\mathbf{Q}$ =13365 cross-section, computed with $N = 3, K = 49$. The energies decay in N in the expected exponential fashion. It appears from this table, and from Figure 5.1, that both the Fourier and the Chebyshev expansions are converged.

TABLE 5.1. Modal energies for point at $\mathbf{Re}_\mathbf{Q} = 13365, A_{E,\mathrm{3D}} = 1.283 \times 10^{-2}$. Computed at highest $A_{E,\mathrm{3D}}$ point with $N = 3, K = 49$.

m	n	Energy
0	0	1.0021384
0	1	$9.78158253 \times 10^{-6}$
0	2	$1.07774084 \times 10^{-8}$
0	3	$4.50330280 \times 10^{-11}$
1	$-\frac{5}{2}$	$2.89416350 \times 10^{-10}$
1	$-\frac{3}{2}$	$1.28737547 \times 10^{-7}$
1	$-\frac{1}{2}$	$9.30757503 \times 10^{-5}$
1	$+\frac{1}{2}$	$7.13819881 \times 10^{-5}$
1	$+\frac{3}{2}$	$1.46914290 \times 10^{-7}$
1	$+\frac{5}{2}$	$2.94577771 \times 10^{-10}$

As discussed in §4.8, a curve of bifurcation points exists on the 2D secondary flow solution surface, from which the 3D subharmonic waves emanate. This curve intersects the Orr-Sommerfeld curve at $\mathbf{Re}_\mathbf{Q} = 11664, \alpha = 1.0881$ and our calculations suggest that it then increases in Reynolds number as it is followed on the 2D

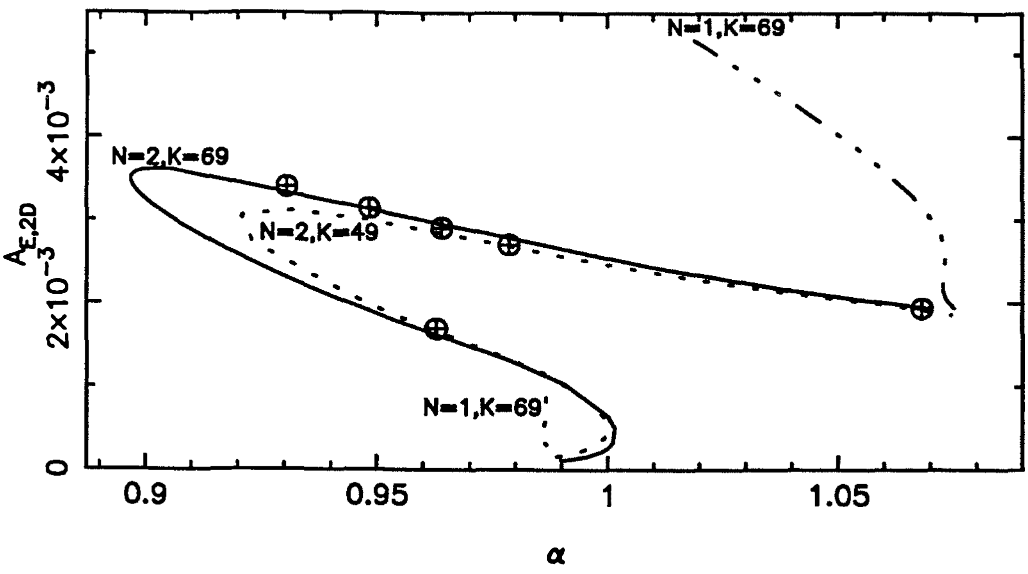

FIGURE 5.17. Comparison of $\mathrm{Re_Q} = 13365$ cross-section at different resolution.

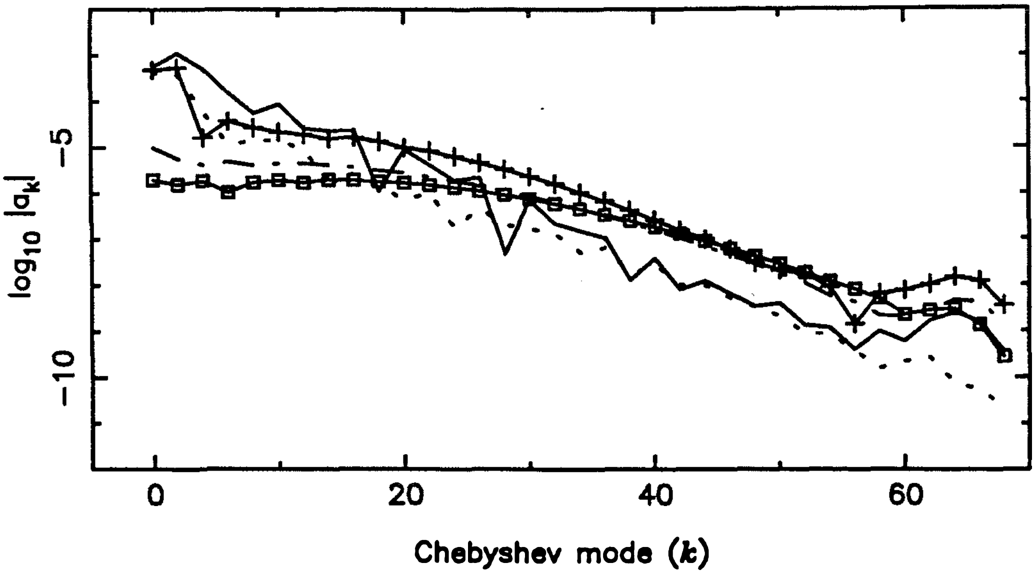

FIGURE 5.18. Decay of Chebyshev modes for the point $\mathrm{Re_Q} = 13365, A_{E,\mathrm{3D}} = 1.617 \times 10^{-2}$ ($M = 1, N = 2, K = 69$). The superharmonic modes (solid lines) and $n < 0$ subharmonic modes (dashed lines) are plotted for the maximum $A_{E,\mathrm{3D}}$ point.

solution surface. The agreement between the 3D subharmonic waves parameters, when $A_{E,\mathrm{3D}} \to 0$, and the 2D solution at the bifurcation point for $\mathbf{Re_Q} = 13364.832$ was found to be (with 2D values in parentheses): $\mathbf{Re_P} = 13366.661(13366.615), \alpha = 1.075(1.081), \beta = 2.01(1.97), E_{\mathrm{2D}} = 3.623 \times 10^{-6}(3.637 \times 10^{-6})$. The difference in resolution ($N = 2, K = 69$ for the subharmonic waves and $N = 1, K = 50$ for the 2D solution and the subharmonic stability) is not important since at these low 3D amplitudes $N = 1, K = 50$ is sufficient for all calculations. In considering the poor agreement, one must take into account the fact that both calculations are subject to error. The subharmonic bifurcation point must be found, to some extent, by trial and error (as described in §4.8). Furthermore, the low 3D amplitude behavior of the subharmonic waves is uncertain at best because the problem becomes ill-conditioned as the bifurcation point is approached. This is because with fixed α (say), $A_{E,\mathrm{3D}} = 0$ corresponds to a single point on the subharmonic curve, but to the whole curve of 2D secondary solutions (at this α). This difficulty stems from the absence of purely real eigenvalues for the 3D subharmonic stability problem.

5.6 Conclusions and recommendations

We have solved the viscous, incompressible 3D Navier-Stokes equations to find steady periodic travelling wave solutions, starting from previously computed 2D secondary flow solutions. Although the size of the systems being solved necessitated making certain symmetry assumptions and computing at relatively low resolution, we believe that the qualitative behavior of the 3D waves found is accurate.

In the superharmonic case several families were investigated (corresponding to different bifurcation points from the 2D secondary flow solution surface). In all cases these solutions "connected" points on the 2D surface with no reduction of the Reynolds number from the minimum computed for the 2D secondary flows.

In the subharmonic case we found that although minimum resolution ($N = 1$ Fourier mode in x) results agreed with those of Goldshtik in giving 3D secondary flows at low Reynolds numbers, the behavior was found to change drastically when N was increased to $N = 2$ (and was maintained for $N = 3$). In this case a single surface of solutions exists, bifurcating from a curve on the 2D solution surface. Once again, however, there is no decrease from the minimum Reynolds number point (in this case on the Orr-Sommerfeld curve) of $\mathbf{Re_Q} = 11664$.

As noted in §4.8, finding bifurcations to 3D subharmonic waves generally requires altering both β and $\mathbf{Re_Q}$ at a fixed α (say). The easiest bifurcation point to compute is that on the Orr-Sommerfeld curve. The possibility exists, however, of other 3D bifurcation points on the 2D secondary flow surface, ones which lie on a curve of bifurcation points not intersecting the Orr-Sommerfeld curve but with $\mathbf{Re_Q} \to \infty$ with decreasing $A_{E,\mathrm{3D}}$. We found what appeared to be such a point at $\mathbf{Re_Q} = 4880$, $\alpha = 1$. However, closer examination revealed this to be a local minimum of the eigenvalue, where $\sigma \approx 0 \pm i10^{-6}$ but does not pass through zero.

In §1.4 we stated that our primary interest in investigating 3D secondary flows was to find candidate vortical states with low Reynolds numbers typical of transition and turbulent flows. It is disappointing that this has not been realized with the 3D superharmonic and subharmonic secondary flows considered in this dissertation. Although it is possible that increased z-resolution, or relaxation of the various symmetry assumptions may yield more productive results, we feel that investigation of families of quasi-periodic flows would be more fruitful. In this respect we note the results of Chapter 3 which indicate that stable, 2D quasi-periodic flows may exist at lower Reynolds numbers than the minimum for 2D secondary flows. The relatively simple structure of these flows may make them amenable to easy numerical investigation.

CHAPTER 6

POISEUILLE-COUETTE FLOW

6.1 Problem formulation

We define Poiseuille-Couette flow (PCF) as PPF with the addition of an upper wall velocity V, with the lower wall remaining fixed in this frame of reference. The stream-function and mean flow velocity for the uniform PCF are just the sums of the component flows:

$$\Psi_{\mathrm{PCF}} = U_0\left(y - \frac{y^3}{3h^2}\right) + \frac{V}{2}\left(y + \frac{y^2}{2h}\right),$$

$$U_{\mathrm{PCF}} = U_0\left(1 - \frac{y^2}{h^2}\right) + \frac{V}{2}\left(1 + \frac{y}{h}\right).$$

The governing equations for the 3D perturbation in PPF follow through to PCF except that the base flow is changed and there is some reinterpretation necessary for the Reynolds numbers. Nondimensionalizing by the underlying PPF velocity U_0 and choosing to apply the flux boundary condition (2.9a) sets $U_0 \equiv U_Q$, where U_Q is the Poiseuille component velocity of the PCF having the same flux as our perturbed flow. Similarly, if we apply the pressure boundary condition (2.9b), then $U_0 \equiv U_P$, where U_P is the Poiseuille component of the PCF having the same pressure gradient as our perturbed flow.

Flux and pressure Reynolds numbers. The physical flux is altered by the Couette component of the base flow, now being

$$Q = [\Psi_{\mathrm{PCF}}]_{-h}^{+h} = \frac{4U_Q h}{3} + Vh,$$

whereas the pressure gradient is unaltered from

$$P = \frac{\nu}{2h}\left[\Psi_{\mathrm{PCF},yy}\right]_{-h}^{+h} = \frac{-2\nu U_P}{h^2}.$$

Some choice is now possible in the definition of the flux Reynolds number $\mathbf{Re_Q}$. We choose to define it in the same relationship to the flux as in (2.11a):

$$\mathbf{Re_Q} = \frac{3Q}{4\nu} = \frac{h}{\nu}\left(U_Q + \frac{3V}{4}\right)$$

However, this is not a convenient quantity for the equations, since after nondimensionalizing by $U_0 \equiv U_Q$ and h in the perturbation equations, the natural quantity appearing depends only on U_Q, so we define

$$\tilde{\mathbf{Re}}_{\mathbf{Q}} = \frac{hU_Q}{\nu} = \frac{3(Q - Vh)}{4\nu} \tag{6.1a}$$

while the pressure Reynolds number is unchanged from its previous definition of

$$\mathbf{Re_P} = \frac{hU_P}{\nu} = \frac{-h^3 P}{2\nu^2}. \tag{6.1b}$$

The dimensional representation of the *total* mean flow is

$$\begin{aligned}\Psi_{\mathrm{PCF}} + \hat{\psi}_0 &\equiv U_Q\left(y - \frac{y^3}{3h^2}\right) + \frac{V_Q}{2}\left(y + \frac{y^2}{2h}\right) + \hat{\psi}_{Q0} \\ &= U_P\left(y - \frac{y^3}{3h^2}\right) + \frac{V_P}{2}\left(y + \frac{y^2}{2h}\right) + \hat{\psi}_{P0},\end{aligned}$$

where V_Q, V_P denote the different nondimensionalized Couette velocities in the two cases. Nondimensionalizing by h and U_Q, U_P respectively and substituting into the boundary condition (2.9b) gives

$$\mathbf{Re_P} = \tilde{\mathbf{Re}}_{\mathbf{Q}}\left(1 - \frac{1}{4}\left[\hat{\psi}_{0Q,yy}\right]_{-1}^{+1}\right) \tag{6.2}$$

as before, because there is no pressure contribution from the Couette flow. In our calculations we have used $\tilde{\mathbf{Re}}_{\mathbf{Q}}$, and then *a posteriori* computed the flux Reynolds number $\mathbf{Re_Q}$ using

$$\mathbf{Re_Q} = \tilde{\mathbf{Re}}_{\mathbf{Q}} \left(1 + \frac{3V_Q}{4}\right).$$

6.2 Numerical results

Using the 3D superharmonic waves computed in Chapter 5 as a starting point, we have computed the corresponding Poiseuille-Couette waves for various wall velocities V. In Figure 6.1 we plot the results for $\alpha = 1.3$. The first subplot shows the $\mathbf{Re_P}$-$\mathbf{Re_Q}$ dependence of the 3D flows with $A_{E,\mathrm{3D}} \approx 0$ for $0 < V < 0.21$. The second subplot shows the same data in the $\mathbf{Re_Q}$-$A_{E,\mathrm{2D}}$ plane. These plots show that at constant flux (constant $\mathbf{Re_Q}$), as the wall velocity V is increased there is an initial small decrease in the pressure gradient (proportional to $\mathbf{Re_P}$) required to drive the flow. This effect is soon out-weighed by the increase in the amplitude of the nonuniform flow, which requires a greater pressure gradient at the same flux. This is more clearly shown in the third subplot of Figure 6.1, where $\mathbf{Re_P}$ is given as a function of V for several different values of $\mathbf{Re_Q}$.

In general, the solution curve shifts to higher Reynolds numbers, even though at a given $\mathbf{Re_Q}$ there is a reduction in $\mathbf{Re_P}$. This indicates that, at least for 2D PCF, the minimum pressure gradient (proportional to $\mathbf{Re_P}$) increases with increasing wall velocity V. This behavior is confirmed in Figures 6.2 and 6.3. Furthermore, the positions of the $V = 0.21$ cross-section in Figure 6.1 and of $V = 0.20$ in Figure 6.2 suggest that the minimum $\mathbf{Re_Q}$ in $(\mathbf{Re_Q}, A_{E,\mathrm{2D}}, \alpha)$ space moves towards lower α as V is increased.

In the remaining subplots of Figures 6.1 and 6.2 we show the 3D behavior for constant Reynolds number and for constant β. These should be compared with the behavior shown in Figure 5.10 and Figure 5.7 respectively for similar parameters (but $V = 0$). Other than the shift to higher Reynolds numbers, there is no significant change in the form of the cross-sections.

6.3 Summary

We conclude that as the Couette wall velocity is increased the 2D solution surface shifts to higher Reynolds number and to lower wavenumber α. Although at given $\mathbf{Re_Q}$ there is an initial decrease in the corresponding $\mathbf{Re_P}$, the overall behavior is for the minimum $\mathbf{Re_P}$ (and thus pressure gradient) to increase with increasing wall velocity V.

Sample cross-sections of 3D PCF suggest that there is little qualitative change from the behavior observed for 3D superharmonic waves in PPF (i.e., PCF with $V = 0$). It seems unlikely, therefore, that following these solutions in PCF space will lead to the discovery of finite amplitude flows in Plane Couette flow.

This does not rule out the possibility of continuation of known finite amplitude flows into Plane Couette flow, but suggests that success will depend on finding some artificial parameter in which to continue. The extreme values of such a parameter would reproduce (for instance) PPF and Plane Couette flow, but continuation would be through a region of physically unrealizable flows.

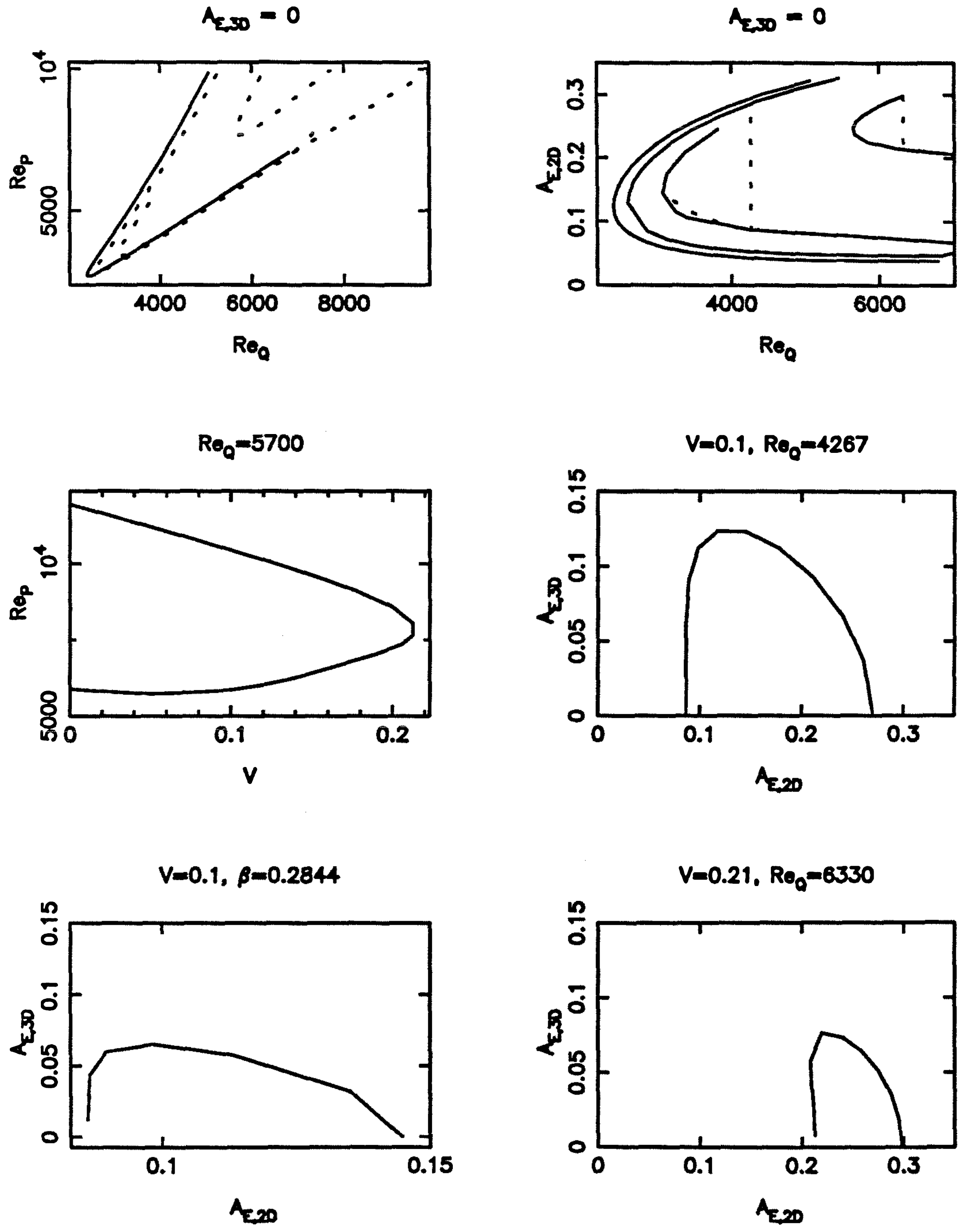

FIGURE 6.1. Poiseuille-Couette flow for $\alpha = 1.3$, $(M = 1, N = 2, K = 50)$. 3D flows computed for A_2 family.

Non-uniform PCF curves for $V = 0.05, 0.1, 0.21$ lie at higher Re_Q (curve labels omitted for clarity).

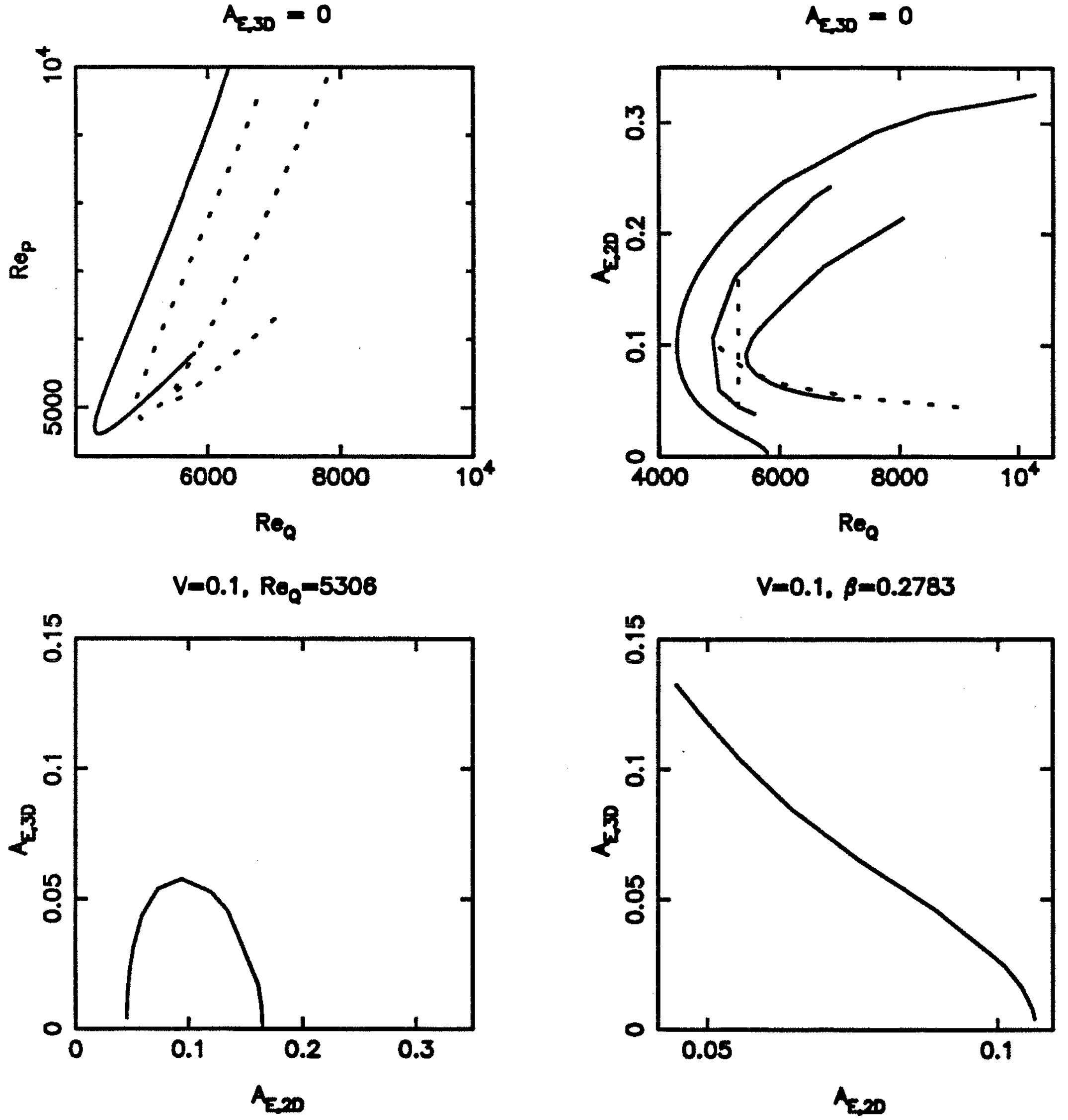

FIGURE 6.2. Poiseuille-Couette flow for $\alpha = 1$, $(M = 1, N = 2, K = 50)$. 3D flows computed for A_1 family.

Non-uniform PCF curves for $V = 0.1$ and 0.2 lie at higher Re_Q (curve labels omitted for clarity).

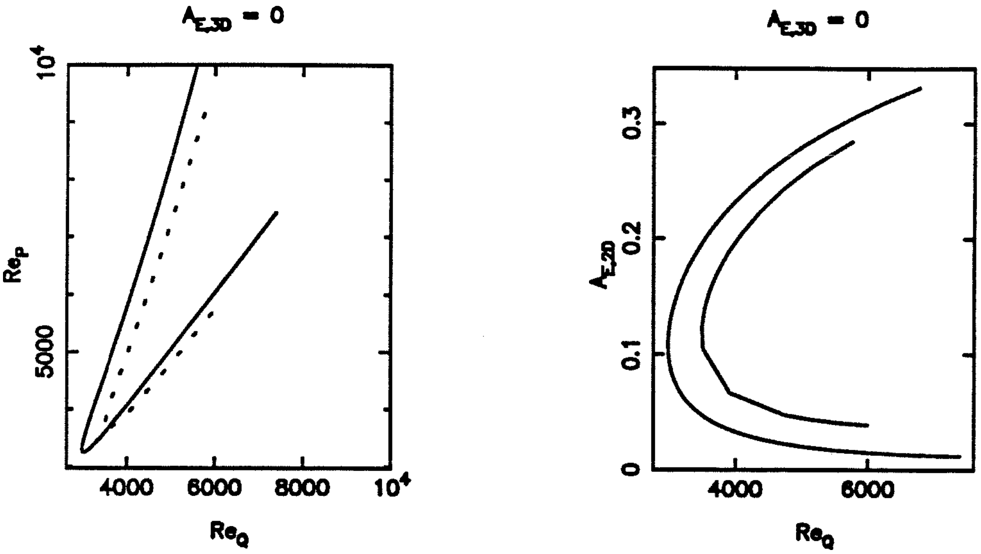

FIGURE 6.3. Poiseuille-Couette flow for $\alpha = 1.1375$, $(M = 1, N = 2, K = 50)$. Non-uniform PCF curve for $V = 0.1$ lies at higher Reynolds numbers (curve labels omitted for clarity).

APPENDIX I

2D SOLUTION SURFACE

In Figures I.1-I.3 we show plots of the relationship of the flux and pressure Reynolds numbers ($\mathbf{Re_Q}, \mathbf{Re_P}$) and the two amplitudes (A, A_E) as defined in (2.18) and (2.17). As noted in §2.1, it has been usual to present numerical results for this work in terms of $\mathbf{Re_P}$, even though there are good reasons for using $\mathbf{Re_Q}$ instead. These figures allow calculation of all quantities from ones given in the text.

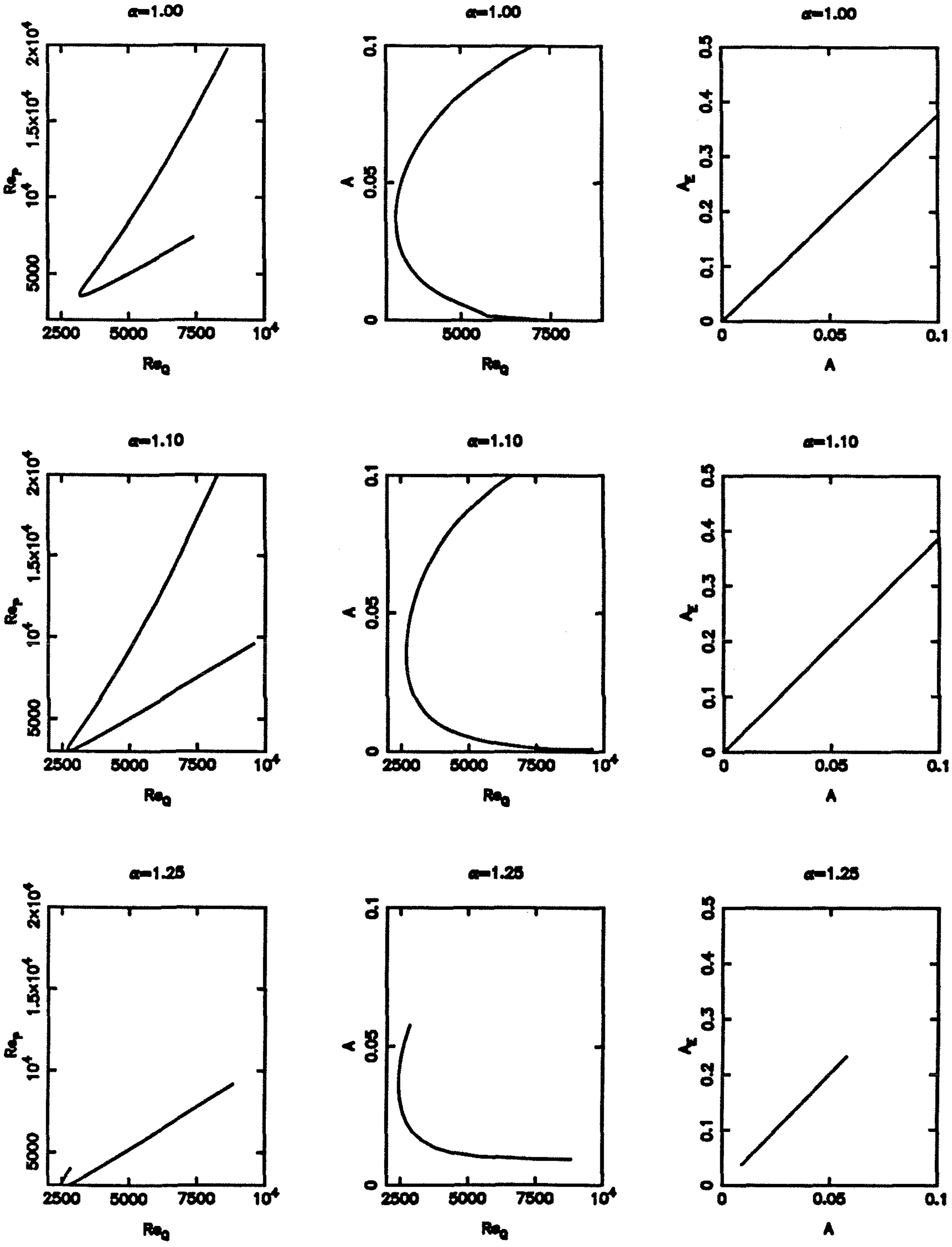

FIGURE I.1. Reynolds numbers and amplitudes for $1 < \alpha < 1.15$ $(N = 1, K = 50)$

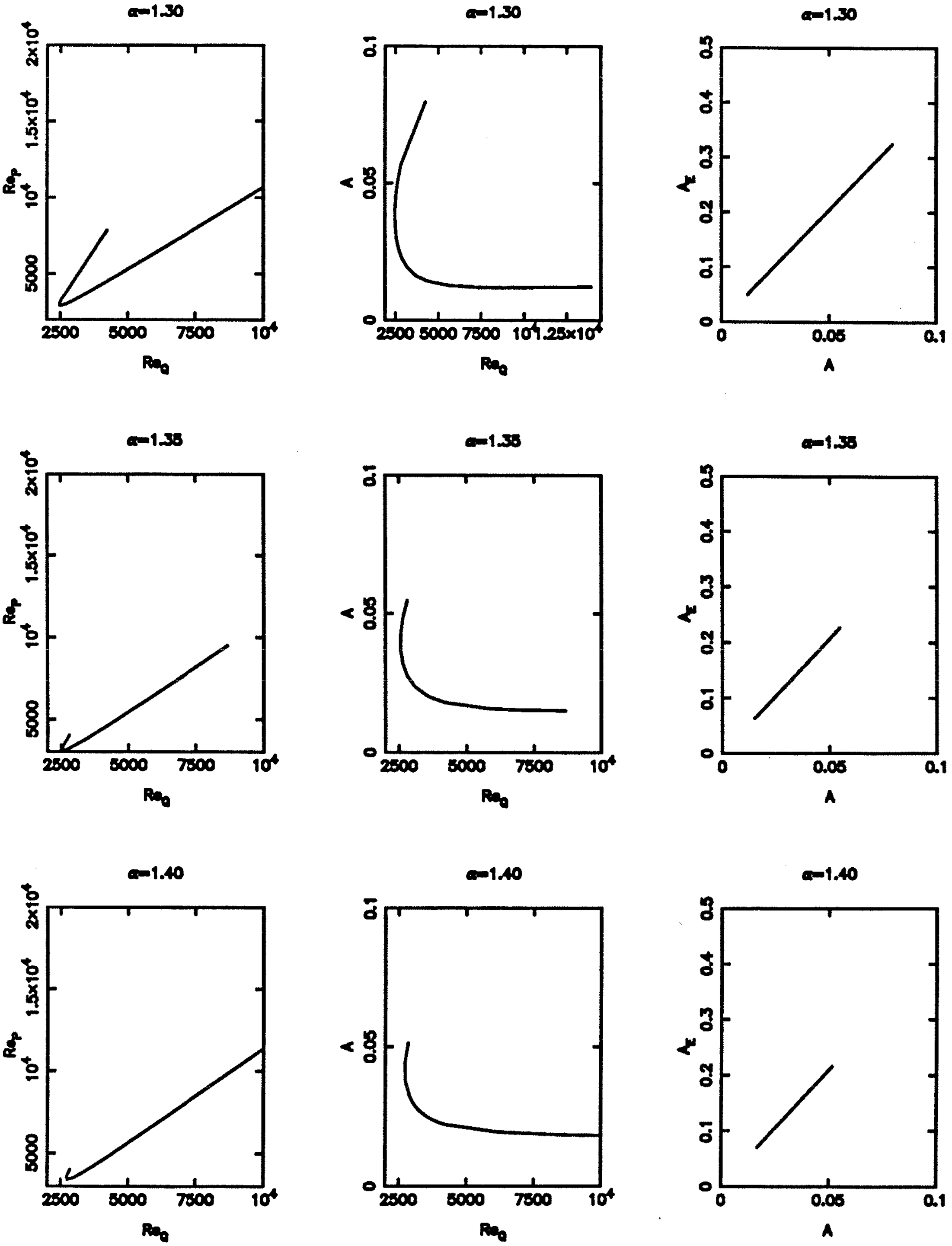

FIGURE I.2. Reynolds numbers and amplitudes for $1.3 < \alpha < 1.4$ ($N = 1, K = 50$)

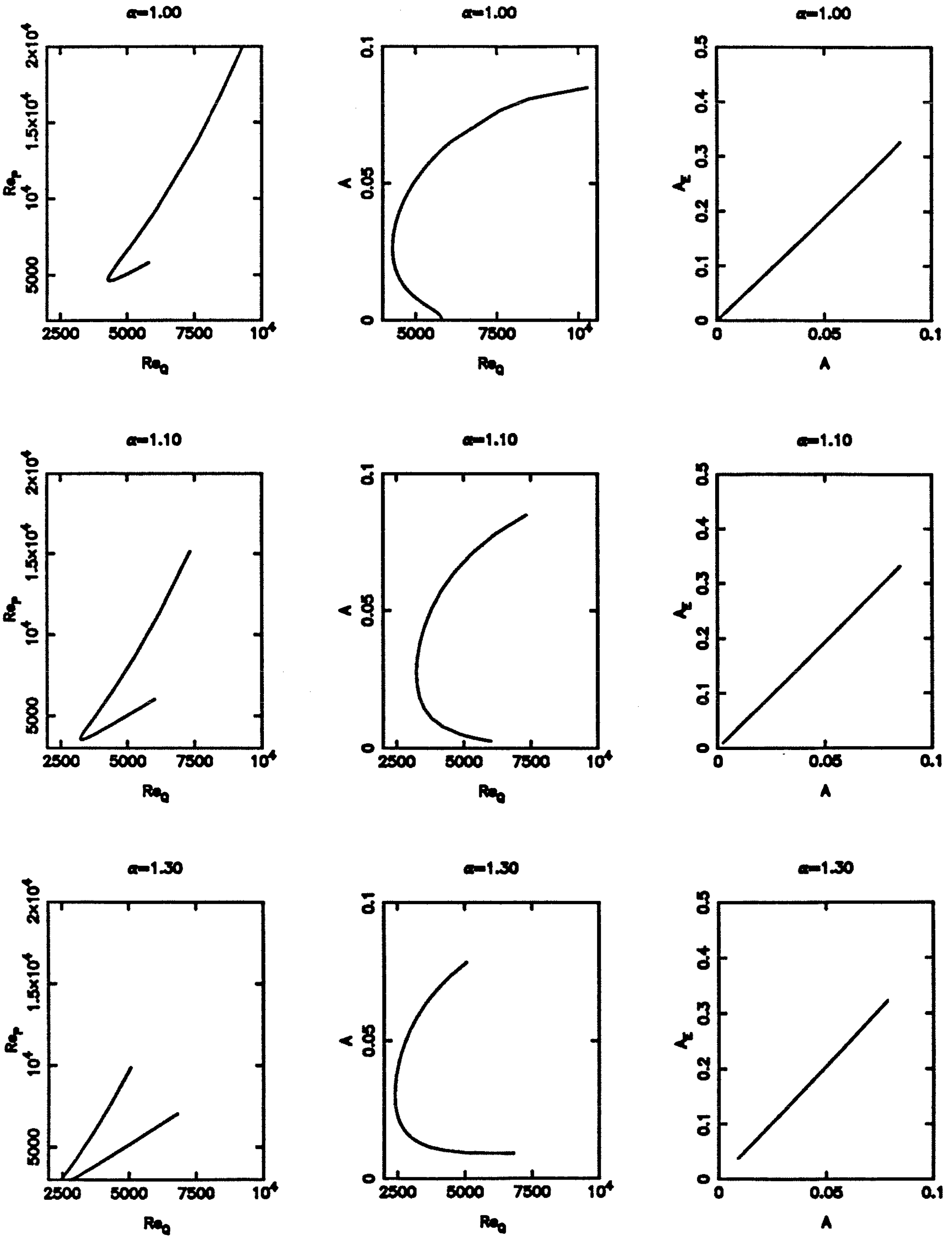

FIGURE I.3. Reynolds numbers and amplitudes for $1 < \alpha < 1.3$ $(N = 2, K = 50)$

Bibliography

Alavyoon F., Henningson D.S. and Alfresson P.H. (1986),
Turbulent spots in plane Poiseuille flow – flow visualization, Phys. Fluids **29** (4), 1328-1331.

Bayly B.J. (1986),
Three-Dimensional Instability of Elliptical Flow, Phys. Rev. Lett. **57**, 2160.

Benney D.J. and Lin C.C. (1960),
On the secondary motion induced by oscillations in a shear flow, Phys Fluids **7**, 319-326.

Biringen S. (1984),
Final stages of transition to turbulence in plane channel flow, JFM **148**, 413-442.

Biringen S. and Maestrello L. (1984),
Development of spot-like turbulence in plane channel flow, Phys. Fluids **27** (2), 318-321.

Carlson D.R., Widnall S.E. and Peeters M.F. (1982),
A flow-visualization study of transition in plane Poiseuille flow, JFM 121, 487-505.

Craik A.D.D. (1971),
Nonlinear resonant instability in boundary layers, JFM **50**, 393-413.

Craik A.D.D and Criminale W.O. (1986),
Evolution of wavelike disturbances in shear flows: a class of exact solutions of the Navier-Stokes equations, Proc. R. Soc. Lond. A **406**, 13.

Davies S.J. and White C.M. (1928),
An experimental study of the flow of water pipes of rectangular section, Proc. R. Soc. Lond. A **119**, 92-107.

Drazin P.G. and Reid W.H. (1981),
Hydrodynamic stability, Cambridge University Press.

Goldshtik M.A., Lifshits A.M. and Shtern V.N. (1983),
The transition Reynolds number for a plane channel, Akademiia Nauk SSSR, Doklady, **273**, No.1, 75-79. In Russian.

Heisenberg W. (1924),
Über Stabilität und Turbulenz von Flüssigkeitsströmen, Ann. Phys. **74**, 577-627.

Herbert Th. (1976),
Periodic secondary motions in a plane channel, Springer Lecture Notes in Physics **59**, 235.

Herbert Th. (1977),
Finite amplitude stability of plane parallel flows, AGARD Conference proceedings CP-224, 3 1-10.

Herbert Th. and Morkovin M.V. (1980),
Dialogue on bridging some gaps in stability and transition research, in *Laminar-Turbulent Transition* (eds. R. Eppler and H. Fasel), Springer-Verlag, 47-72.

Herbert Th. (1983a),
Stability of plane Poiseuille flow – Theory and experiment, Fluid Dynamics Transaction **11**, 77-126.

Herbert Th. (1983b),
Secondary instability of plane channel flow to subharmonic three-dimensional disturbances, Phys. Fluids **26**(4) (April 1983), 871-874.

Herbert Th. (1983c),
Modes of secondary instability in Plane Poiseuille Flow, Proceedings of the IUTAM Symposium on "Turbulence and Chaotic Phenomena in Fluids", September 1983.

Herbert Th. (1984),
Secondary instability of plane shear flows – Theory and application, Proceedings of the IUTAM Symposium on "Laminar-Turbulent Transition", July 1984.

Karnitz M.A., Potter M.C. and Smith M.C. (1974),
An experimental investigation of transition of a plane Poiseuille flow, J. Fluids Engng. **96**, 384388.

Kato T. (1966),
Perturbation theory for linear operators, Springer-Verlag, New York, 43.

Keller H.B. (1977),
Numerical Solution of Bifurcation and Nonlinear Eigenvalue Problems in *Applications of Bifurcation Theory*, Academic Press Inc.

Kim J. (1983),
On the structure of wall-bounded turbulent flows, Phys. Fluids **26** (8), 2088-2097.

Klebanoff P.S., Tidstrom K.D. and Sargent L.M. (1962),
The three-dimensional nature of boundary-layer instability, JFM **12**, 1-34.

Kleiser L. (1982),
Spectral simulations of laminar-turbulent transition in plane Poiseuille flow and comparison with experiments, in *Proc. 8th Intl Conf. on Numerical Methods in Fluid Dynamics, Aachen* (ed. E. Krause), Springer Lecture Notes in Physics **170**, 280.

Kozlov V.V. and Ramazanov M.P. (1980),
Experimental investigation of the growth process of disturbances in Poiseuille flow, Preprint 21, Inst. Theor. Appl. Mech., AN SSSR SO, Novosibirsk.

Kozlov V.V. and Ramasanov M.P. (1982),
I.T.A.M., USSR AN Novsibirsk, Preprint 4-82.

Kozlov V.V. and Ramazanov M.P. (1984),
Development of finite-amplitude disturbances in Poiseuille flow, JFM **147**, 149-157.

Krist S.E. and Zang T.A. (1987),
Numerical simulation of channel flow transition: Resolution requirements and structure of the hairpin vortex, NASA technical paper **2667**.

Landman M.J. (1987),
New solutions of an amplitude equation describing transition in a laminar shear flow, Ph.D. thesis, Caltech.

Landman M.J. and Saffman P.G. (1987),
On the Three-Dimensional Instability of Strained Vortices in a Viscous Fluid, submitted to Phys. Fluids.

Lin C.C. (1944),
On the stability of two-dimensional parallel flows, Proc. Nat. Acad. Sci., Wash., **30**, 316-323.

Marsden J.E. and McCracken M. (editors) (1976),
The Hopf Bifurcation and Its Applications, Applied Mathematical Sciences **19**, Springer-Verlag, New York.

Meksyn D. and Stuart J.T. (1951),
Stability of viscous motion between parallel planes for finite disturbances, Proc. Roy. Soc. A **208**, 517-526.

Milinazzo F.A. and Saffman P.G. (1985),
Finite-amplitude waves in plane viscous shear flows, JFM **160**, 281-295.

Nishioka M., Iida S. and Ichikawa Y. (1975),
An experimental investigation of the stability of plane Poiseuille flow, JFM **72**,

731-751.

Nishioka M., Iida S. and Kanbayashi S. (1978),
An experimental investigation of the subcritical instability in plane Poiseuille flow, Proc. 10th Turbulence Symposium, Inst. Space Aeron. Sci., Tokyo Univ., 55-62.

Nishioka M., Asai M. and Iida S. (1980),
An experimental investigation of secondary instability, in *Laminar-Turbulent Transition* (eds. R. Eppler and H. Fasel), Springer-Verlag, 37-46.

Nishioka M., Asai M. and Iida S. (1981),
Wall phenomena in the final stage of transition to turbulence, in *Transition and Turbulence* (ed. R.E. Meyer), Academic Press, 113-126.

Nishioka M. and Asai M. (1985),
Some observations of the subcritical transition in plane Poiseuille flow, JFM **150**, 441-450.

Orszag S.A. (1971),
Accurate solution of the Orr-Sommerfeld stability equation, JFM **50**, 689-703.

Orszag S.A. and Gottlieb D. (1977),
Numerical Analysis of Spectral Methods: Theory and Applications, Society for Industry and Applied Mathematics **26**, 14.

Orszag S.A. and Kells L.C. (1980),
Transition to turbulence in plane Poiseuille and plane Couette flow, JFM **96**, 159-206.

Orszag S.A. and Patera A.T. (1981),
Subcritical transition to turbulence in planar shear flows, in *Transition and Turbulence* (ed. R.E. Meyer), Academic Press, 127-146.

Orszag S.A. and Patera A.T. (1983),
Secondary instability of wall-bounded shear flows, JFM **128**, 347-385.

Patel V.C. and Head M.R. (1969),
Some observations in skin friction and velocity profiles in fully developed pipe and channel flows, JFM 38, 181-201.

Pierrehumbert R.T. (1986),
Universal Short-Wave Instability of Two-Dimensional Eddies in an Inviscid Fluid, Phys. Rev. Lett. **57**, 2157.

Reichardt H. (1956),
Über die Geschwindigkeitsverteilung in einer geradlinigen turbulenen Couetteströmung, Z. Angew. Math. Mech. **36**, S26-9, 454.

Rozhdestvensky B.L. and Simakin I.N. (1984),
Secondary flows in a plane channel: their relationship and comparison with turbulent flows. JFM **147**, 261-289.

Saffman P.G. (1983),
Vortices, stability, and turbulence, in *Fourth International Conference on Physicochemical Hydrodynamics* (ed. R. Pfeffer), Annals of the New York Academy of Sciences **404**, 12-24.

Saric W.S. and Reynolds G.A. (1980),
in *Laminar-Turbulent Transition* (eds. R. Eppler and H. Fasel), Springer-Verlag, 125.

Saric W.S. and Thomas A.S.W. (1983),
Experiments on the subharmonic route to turbulence in boundary layers, Proc. IUTAM Symposium on "Turbulence and Chaotic Phenomena in Fluids", Kyotoa, Japan.

Saric W.S., Kozlov V.V. and Levchenko V.Ya. (1984),
Forced and unforced subharmonic resonance in boundary layer transition, AIAA Paper No. 84-0007.

Stewartson K. and Stuart J.T. (1971),
A non-linear instability theory for a wave system in plane Poiseuille flow, JFM **48**, 529-545.

Strang G. (1980),
Linear Algebra and its applications (2nd edition), Academic Press.

Toplosky N. and Akylas T.R. (1987),
Nonlinear spiral waves in rotating pipe flow, submitted to JFM.

Thomas L.H. (1953),
The stability of plane Poiseuille flow, Phys. Rev. **91**, 780-783.

Williams D.R., Fasel H. and Hama F.R. (1984),
Experimental determination of the three-dimensional vorticity field in the boundary layer transition process, JFM **149**, 179-203.

Zahn J.-P., Toomre J., Spiegel E.A. and Gough D.O. (1974),
Nonlinear cellular motions in Poiseuille channel flow. JFM **64** part 2, 319-345.